POLARIZATION DYNAMICS OF SINGLE-PHOTON EMITTERS IN HEXAGONAL BORON NITRIDE AND THEIR APPLICATION IN QUANTUM KEY DISTRIBUTION

A Thesis Submitted to
the Graduate School of
İzmir Institute of Technology
in Partial Fulfillment of the Requirements for the Degree of

DOCTOR OF SCIENCE

in Physics

by
Çağlar SAMANER

July 2025
İZMİR

We approve the thesis of **Çağlar SAMANER**

Examining Committee Members:

Assoc. Prof. Dr. Serkan ATEŞ
Department of Physics, İzmir Institute of Technology

Assoc. Prof. Dr. Özgür ÇAKIR
Department of Physics, İzmir Institute of Technology

Assoc. Prof. Dr. İbrahim SARPKAYA
UNAM, Bilkent University

Prof. Dr. Feridun AY
Department of Electrical-Electronics Engineering, Eskişehir Technical University

---

Prof. Dr. Alpan BEK
Department of Physics, Middle East Technical University

18 July 2025

Assoc Prof. Dr. Serkan ATEŞ
Supervisor, Department of Physics
İzmir Institute of Technology

Prof. Dr. Lütfi ÖZYÜZER
Head of the Department of Physics

Prof. Dr. Mehtap EANES
Dean of the Graduate School

ABSTRACT

POLARIZATION DYNAMICS OF SINGLE-PHOTON EMITTERS IN HEXAGONAL BORON NITRIDE AND THEIR APPLICATION IN QUANTUM KEY DISTRIBUTION

The advancement of quantum technologies is critically dependent on the development of high-performance solid-state single-photon sources. Among emerging platforms, defects in hexagonal boron nitride (hBN) have garnered significant attention due to their bright and stable single-photon emission at room temperature. However, a comprehensive understanding of their polarization properties, which are crucial for encoding quantum information, has been limited by time-averaged measurement techniques that obscure dynamic effects. This thesis presents a multifaceted investigation into the nanosecond-scale polarization dynamics of single-photon emitters in hBN and demonstrates their successful application in quantum key distribution.

First, we introduce and apply a time-resolved analysis of the linear polarization, revealing that the degree of linear polarization is not static but evolves significantly throughout the emission lifetime. We find that the most highly polarized photons are emitted within the first few nanoseconds of the decay process. To deconstruct this behavior, we then perform a complete time-resolved Stokes parameter analysis. This advanced method reveals that the observed depolarization in the linear basis is not solely due to random fluctuations but arises from a dynamic interplay with a significant circular polarization component, demonstrating a near-unity degree of polarization even when the degree of linear polarization is reduced.

Finally, by harnessing these fundamental insights, we report the first integration of a 2D material-based single-photon source into a functional quantum key distribution system. A characterized hBN defect was used as the quantum light source in a free-space B92 protocol implementation at room temperature, successfully establishing a secure key with a quantum bit error rate of 8.95%. This work not only provides a deeper understanding of the complex photo-physics of hBN emitters but also confirms their viability as a robust and scalable resource for practical quantum communication technologies.

ÖZET

ALTIGEN BOR NİTRÜR'DEKİ TEK FOTON YAYICILARIN POLARİZASYON DİNAMİKLERİ VE KUANTUM ANAHTAR DAĞITIMINDAKİ UYGULAMALARI

Kuantum teknolojilerinin ilerlemesi, yüksek performanslı katı-hal tek-foton kaynaklarının geliştirilmesine kritik düzeyde bağlıdır. Gelişmekte olan platformlar arasında, altıgen bor nitrür (hBN) içindeki kusurlar, oda sıcaklığında parlak ve kararlı tek-foton emisyonu göstermeleri nedeniyle önemli ölçüde dikkat çekmiştir. Ancak, kuantum bilgisini kodlamak için hayati önem taşıyan polarizasyon özelliklerinin kapsamlı bir şekilde anlaşılması, dinamik etkileri göz ardı eden zaman-ortalamalı ölçüm teknikleri nedeniyle sınırlı kalmıştır. Bu tez, hBN'deki tekil foton yayıcıların nanosaniye ölçeğindeki polarizasyon dinamiklerine yönelik çok yönlü bir araştırmayı sunmakta ve bu yayıcıların kuantum anahtar dağıtımı uygulamasındaki başarılı kullanımını göstermektedir.

İlk olarak, doğrusal polarizasyonun zaman-çözünürlüklü bir analizini sunup uygulayarak, doğrusal polarizasyon derecesinin statik olmadığını, bunun yerine emisyon ömrü boyunca önemli ölçüde evrildiğini ortaya koyuyoruz. En yüksek düzeyde polarize olmuş fotonların, bozunmanın ilk birkaç nanosaniyesi içinde yayıldığını bulduk. Bu davranışı çözümlemek için, ardından tam bir zaman-çözünürlüklü Stokes parametre analizi gerçekleştirdik. Bu gelişmiş yöntem, doğrusal bazda gözlemlenen depolarizasyonun yalnızca rastgele dalgalanmalardan kaynaklanmadığını, aynı zamanda doğrusal polarizasyon derecesi düşerken bile, bire yakın bir polarizasyon derecesi gösteren önemli bir dairesel polarizasyon bileşeni ile dinamik bir etkileşimden kaynaklandığını ortaya koymaktadır.

Son olarak, bu temel bilgilerden yararlanarak, 2B malzeme tabanlı bir tek-foton kaynağının, işlevsel bir kuantum anahtar dağıtımı sistemine ilk entegrasyonunu rapor ediyoruz. Karakterize edilmiş bir hBN kusur merkezi, oda sıcaklığında çalışan serbest uzay B92 protokolü uygulamasında kuantum ışık kaynağı olarak kullanılmış ve %8.95'lik bir kuantum bit hata oranı ile güvenli bir anahtar başarıyla oluşturulmuştur. Bu çalışma, sadece hBN tek foton yayıcılarının karmaşık fotofiziğine dair daha derin bir anlayış sağlamakla kalmayıp, aynı zamanda pratik kuantum iletişim teknolojileri için sağlam ve ölçeklenebilir bir kaynak olarak uygunluklarını da doğrulamaktadır.

ACKNOWLEDGMENTS

First and foremost, I would like to express my sincere gratitude to my advisor, Assoc. Prof. Dr. Serkan Ateş, for his invaluable guidance, continuous support, and encouragement throughout my doctoral studies.

I would also like to thank my thesis committee members, Assoc. Prof. Dr. Özgür Çakır and Assoc. Prof. Dr. İbrahim Sarpkaya, for their insightful comments and constructive suggestions, which significantly improved the quality of this work.

I am deeply grateful to my labmates, Serkan Paçal, Furkan Ağlarcı, Ömer Tapşın, and Yağız Oyun, for the many helpful discussions, their camaraderie, and the collaborative atmosphere we shared throughout the years.

Lastly, I am deeply grateful to my wife, Gaye Samaner, for her endless love, patience, and unwavering support. This work would not have been possible without her presence by my side.

TABLE OF CONTENTS

LIST OF TABLES

LIST OF FIGURES

Figure **Page**

CHAPTER 1

INTRODUCTION

The rise of quantum technologies has spurred intense research into solid-state single-photon sources (SPSs), which are essential components for quantum computation (*1*), communication (*2*), sensing (*3*), quantum key distribution (QKD) (*4*), and quantum random number generation (*5*, *6*). These technologies utilize non-classical light to achieve functionalities that are unattainable with classical resources, including enhanced security, parallel processing, and increased sensitivity. Quantum computers use single photons as qubits to exploit superposition and entanglement for scalable logic operations. In sensing, quantum correlations enable improved resolution and noise suppression, while QKD protocols ensure provably secure information exchange. Quantum random number generators derive their unpredictability from fundamental quantum indeterminacy, offering certified randomness critical for cryptographic applications. These and other quantum-enabled technologies rely on precise control of single-photon properties.

Among the key candidates for SPSs, quantum dots (*7*, *8*), color centers in diamond (*9*), and emerging two-dimensional (2D) materials (*10*, *11*) have demonstrated outstanding potential. In particular, hexagonal boron nitride (hBN), with its wide bandgap and the ability to host bright and optically stable defects, has emerged as a robust platform for room-temperature quantum emitters (*12*, *13*). These defect-based SPSs span a broad spectral range (*14*), offer integration compatibility with photonic circuits (*15*), and demonstrate resilience in high temperature environments (*16*). Furthermore, the scalability and chemical stability of hBN provide a viable route for practical and large-scale deployment of SPSs (*17*, *18*). Despite impressive progress in fabricating and characterizing hBN quantum emitters (*19–22*), a comprehensive understanding of their emission properties, particularly polarization characteristics, remains limited.

Single-photon sources are often characterized by features such as photon purity (*23*), indistinguishability (*24*), brightness (*25*), and emission dynamics (*26*), which are central to many quantum applications. Among these attributes, polarization plays a dual role: it is both a fundamental physical observable and an information carrier (*27*). In photonic quantum computing, polarization qubits enable interference-based gates and entanglement (*28*, *29*), while in QKD protocols such as BB84 or B92, polarization encodes cryptographic keys (*30*). However, the polarization of photons emitted from defect-based

sources is often degraded due to local strain, phonon interactions, or nearby charge environments (*31*, *32*). Furthermore, most studies characterize polarization using time-averaged intensity measurements, which overlook the dynamic effects that arise during excited-state evolution. This underscores the need for advanced methods to access complete polarization information, including circular components, and resolve temporal variations on the nanosecond scale.

To realize high-performance quantum devices, the optimization of quantum emitters must extend beyond brightness and purity to incorporate complete polarization control (*33–35*). Techniques such as resonant excitation (*36*, *37*), cavity coupling (*38*, *39*), and emitter waveguide integration (*40*) have been proposed to enhance quantum light-matter interfaces. Nevertheless, a precise understanding of the system's dynamics is essential for engineering emitter environments, minimizing decoherence (*41*), and tailoring emission properties for specific applications (*42*, *43*). In this context, our recent work introduces a novel combination of time-resolved Stokes parameter analysis and dipole crystal orientation mapping, performed on single defects in hBN and nanodiamond platforms (*44*, *45*). This approach provides sub-nanosecond resolution for the temporal evolution of polarization and dipole misalignment, offering crucial insights for polarization-encoded protocols and a fundamental understanding of defect emission processes. Our findings pave the way for new emitter characterization schemes, the identification of emitters (*46–48*), and the rational design of defect-based SPSs with engineered polarization profiles.

The remainder of this thesis is structured as follows:

Chapter 2 provides the theoretical background necessary for this work. It covers the principles of single-photon emission, including photon statistics and coherence functions, introduces the fundamentals of solid-state emitters, and details the mathematical formalisms, such as Stokes parameters, used to describe polarized light.

Chapter 3 details the experimental methods employed throughout our research. This includes a description of the custom-built confocal micro-photoluminescence setup, the principles of time-correlated single photon counting for lifetime analysis, and the second-order photon correlation measurement technique used to verify single-photon emission.

Chapter 4 presents the first main experimental study of this thesis, focusing on the polarization dynamics of hBN emitters. It first details the time-resolved analysis in a linear basis, revealing dynamic changes in the degree of linear polarization. It then presents a more comprehensive analysis using Stokes parameters to decompose the emission into its linear and circular components and map its evolution on the Poincare sphere.

Chapter 5 details the second significant contribution: the application of an hBN single-photon source in a quantum communication protocol. It provides an overview of QKD principles, followed by a detailed account of our proof-of-concept demonstration of the B92 protocol, including the system's performance, error analysis, and a simulation of its future potential.

Chapter 6 concludes the thesis by summarizing the key findings from our studies on polarization dynamics and QKD, discussing their broader scientific and technological implications, and providing an outlook on promising future research directions.

CHAPTER 2

THEORETICAL BACKGROUND

In this chapter, we provide a brief theoretical foundation to support the experimental work presented in this thesis. We begin by discussing photon statistics to establish a foundation for understanding single-photon emission. Subsequently, we explore the mechanisms of non-resonant single-photon emission using relevant mathematical models, followed by an introduction to single-photon sources, with an emphasis on solid-state systems and the role of the Franck-Condon principle in optical responses. The chapter concludes with an overview of hBN as a single-photon source and the mathematical representation of light, with a focus on Stokes polarization parameters.

2.1. Single Photon Emitters

Single photon emitters (SPEs) are crucial for quantum technologies due to their ability to produce light with unique statistical properties. Understanding these properties begins with an analysis of photon statistics, which characterize the emission behavior of different light sources.

2.1.1. Photon Statistics

The probability $P(n)$ of detecting n photons in a coherent state of light is given by (*49*):

$$P(n) = \frac{\bar{n}^n e^{-\bar{n}}}{n!}, \quad n = 0, 1, 2, ... \tag{2.1}$$

where $\bar{n}$ is called the mean photon number, or mean value in general. Equation 2.1 describes the **Poisson Distribution.** The Poisson distribution provides a statistical model for situations where events occur randomly and return only integer values. When applied to photon statistics, the Poisson distribution is often associated with coherent light sources, such as ideal lasers, where the emission of photons is a purely random process.

A notable feature of the Poisson distribution is that its variance $(\Delta n)^2$ is equal to its mean value $\bar{n}$, leading to the relationship:

$$(\Delta n)^2 = \bar{n}, \tag{2.2}$$

where Δn is the distribution's standard deviation and represents the light beam's photon number fluctuations. This equality between the variance and the mean photon number is a hallmark of coherent light sources, serving as a reference point for comparing other types of light sources.

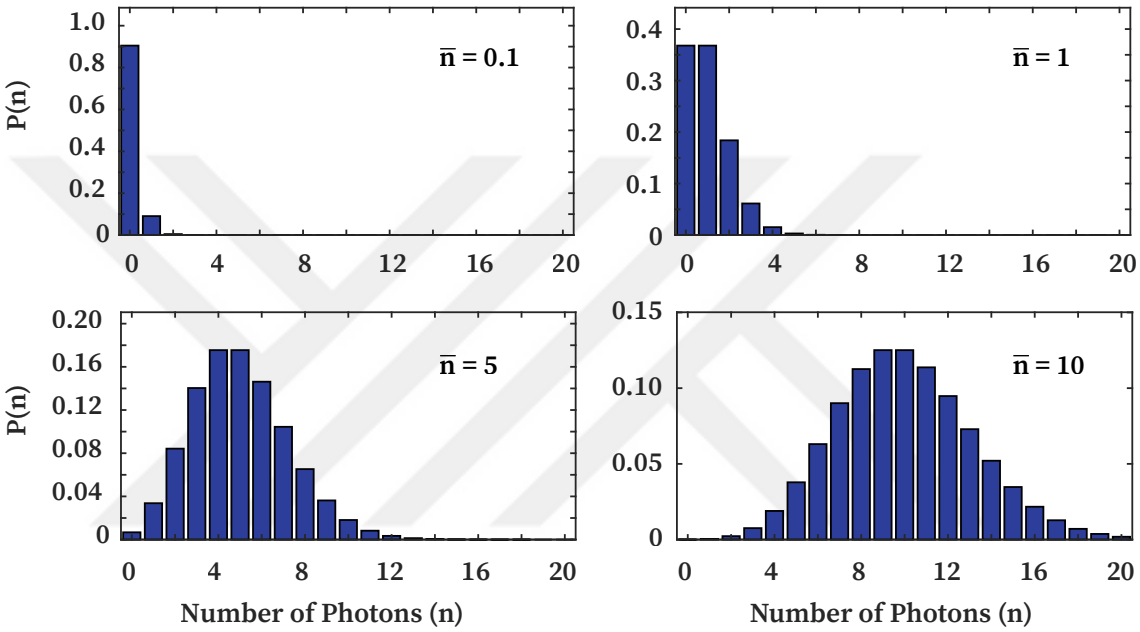

Figure 2.1: Photon number distributions for Poissonian light with different mean photon numbers ($\bar{n}$). The distributions demonstrate how increasing the mean photon number broadens the distribution, transitioning from a highly peaked form at $\bar{n} = 0.1$ to a more symmetric and spread-out distribution at $\bar{n} = 10$.

Figure 2.1 displays the general behavior of the Poisson distribution for various $\bar{n}$ values. As $\bar{n}$ increases, the distribution broadens and becomes more symmetrical around its mean value. For $\bar{n} = 0.1$, the probability of detecting exactly one photon is negligible and dominated by the likelihood of detecting zero photons. In contrast, for $\bar{n} = 1$, the probability of detecting exactly one photon is comparable to that of detecting two photons, with higher photon numbers also having considerable probabilities, highlighting the inefficiency of single-photon generation in weak Poissonian sources such as an attenuated laser beam.

2.1.2. Classification of Light by Photon Statistics

Photon statistics not only describe the probability of detecting a certain number of photons but also allow for the classification of light based on the nature of photon number fluctuations. The standard deviation of the photon distribution Δn compared to the mean photon number $\bar{n}$ determines the classification of light. There are three possible categories:

- **super-Poissonian statistics:** $\Delta n > \sqrt{\bar{n}}$,
- **Poissonian statistics:** $\Delta n = \sqrt{\bar{n}}$,
- **sub-Poissonian statistics:** $\Delta n < \sqrt{\bar{n}}$.

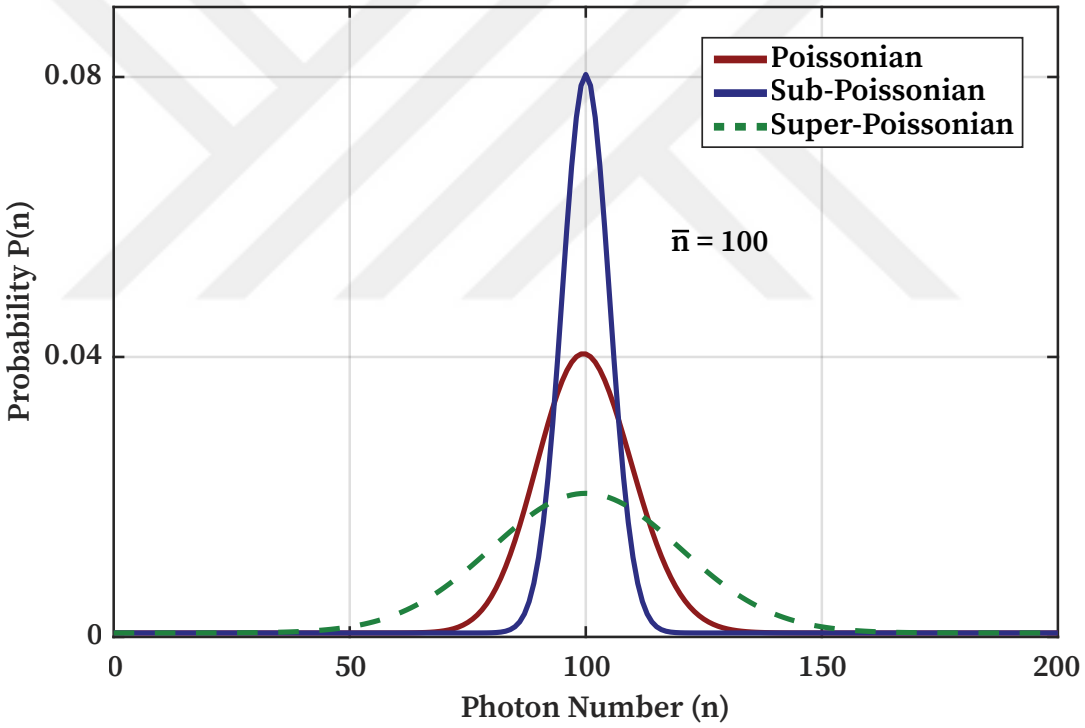

Figure 2.2: Photon number distributions $P(n)$ for a mean photon number $\bar{n} = 100$. The **Poissonian** (solid red), **Sub-Poissonian** (solid blue), and **Super-Poissonian** (dashed green) distributions illustrate different statistical regimes of photon number fluctuations (*49*).

The difference between the three cases is illustrated in Figure 2.2. Super-Poissonian light exhibits larger fluctuations in the photon number compared to Poissonian light. This is typical of thermal or chaotic light sources, where photon bunching increases the variance of the photon statistics. The broader distribution of super-Poissonian light, as shown in Figure 2.2, reflects this higher variability.

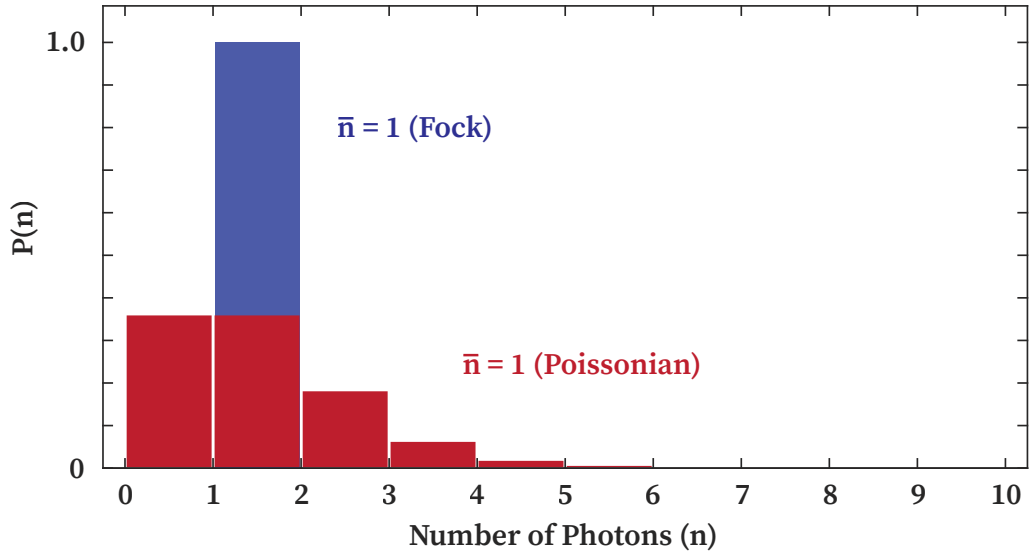

Figure 2.3: Photon number distribution $P(n)$ for a beam of light with a fixed photon number $\bar{n}$ with no fluctuations. Such states are called photon number states (Fock states), and the distribution is a delta function at $n = \bar{n}$. The figure shows the $\bar{n} = 1$ for Fock and Poissonian Distributions.

Sub-Poissonian light, by contrast, demonstrates reduced fluctuations compared to a Poisson distribution. This behavior is characteristic of quantum light sources, particularly those that emit single photons. The ideal case of a sub-Poissonian distribution would be a sharp peak at $\bar{n} = 1$, representing a perfect single-photon source illustrated in Figure 2.3. The Poissonian distribution with $\bar{n} = 1$ is also shown in the figure for better comparison. Such light sources are crucial in quantum technologies, where suppressing multi-photon events is necessary.

2.1.3. The Second-Order Coherence Function

While the classification based on photon number fluctuations (Δn versus $\sqrt{\bar{n}}$) provides a theoretical framework for understanding different types of light, an experimentally accessible quantity that directly probes these statistical properties is the **normalized second-order coherence function**, denoted as $g^{(2)}(\tau)$. This function measures the correlation between the intensity of a light field at two different times, t and $t + \tau$, effectively quantifying the conditional probability of detecting a photon at time $t + \tau$, given that one was detected at time t.

Classically, for a light field with electric field $\mathcal{E}(t)$ and instantaneous intensity $I(t)$ (where $I(t) \propto |\mathcal{E}(t)|^2$), and assuming a statistically stationary light field (where average properties are independent of the absolute time t), the normalized second-order coherence

function is defined as (*50*, *51*):

$$g^{(2)}(\tau) = \frac{\langle \mathcal{E}^*(t)\,\mathcal{E}^*(t+\tau)\,\mathcal{E}(t+\tau)\,\mathcal{E}(t)\rangle}{(\langle|\mathcal{E}(t)|^2\rangle)^2} = \frac{\langle I(t)\,I(t+\tau)\rangle}{\langle I(t)\rangle^2}. \tag{2.3}$$

Here, $\langle \dots \rangle$ denotes a time average over t. The value of $g^{(2)}(\tau)$ at zero time delay, $g^{(2)}(0)$, is particularly insightful. It is important to note that for any classical field theory, where light is described by fluctuating electric fields or intensities, it can be shown (e.g., using the Cauchy-Schwarz inequality) that $g^{(2)}(0) \geq 1$ (*50*). Therefore, the observation of $g^{(2)}(0) < 1$ is a direct signature of the quantum nature of light, indicating that a purely classical description is insufficient. The classification based on $g^{(2)}(0)$ is as follows:

- $g^{(2)}(0) = 1$: This characterizes **Poissonian light** (e.g., an ideal laser). Photon detection events are independent; the detection of one photon provides no information about the likelihood of detecting another immediately.
- $g^{(2)}(0) > 1$: This indicates **super-Poissonian light** (e.g., thermal or chaotic light). This phenomenon is known as *photon bunching*, where photons have a higher-than-random probability of arriving in close succession. For thermal light, $g^{(2)}(0) = 2$.
- $g^{(2)}(0) < 1$: This signifies **sub-Poissonian light**, a non-classical feature. This phenomenon is known as *photon anti-bunching*, where the detection of one photon reduces the probability of detecting another photon immediately.

For an ideal single-photon emitter, which by definition emits one photon at a time, it is impossible to detect two photons simultaneously. Consequently, such a source would exhibit $g^{(2)}(0) = 0$. In experimental reality, factors like detector dark counts, background light, and multi-photon emission from imperfect sources lead to $g^{(2)}(0) > 0$. A widely accepted criterion for claiming single-photon emission is $g^{(2)}(0) < 0.5$ (*52*, *53*), indicating that the probability of detecting two photons simultaneously is at least halved compared to a coherent source of the same intensity.

For stationary light sources, as $\tau \to \infty$, the photon detection events become uncorrelated, and $g^{(2)}(\tau) \to 1$. The full temporal behavior of $g^{(2)}(\tau)$ provides information about the emission dynamics of the source, such as excited state lifetimes or, in more complex systems, transitions to metastable states.

These characteristic behaviors of $g^{(2)}(\tau)$ for different types of light are illustrated in Figure 2.4. For thermal light (super-Poissonian), photon bunching is observed as a peak with $g^{(2)}(0) = 2$, which then decays towards $g^{(2)}(\tau) = 1$ for larger τ. Coherent

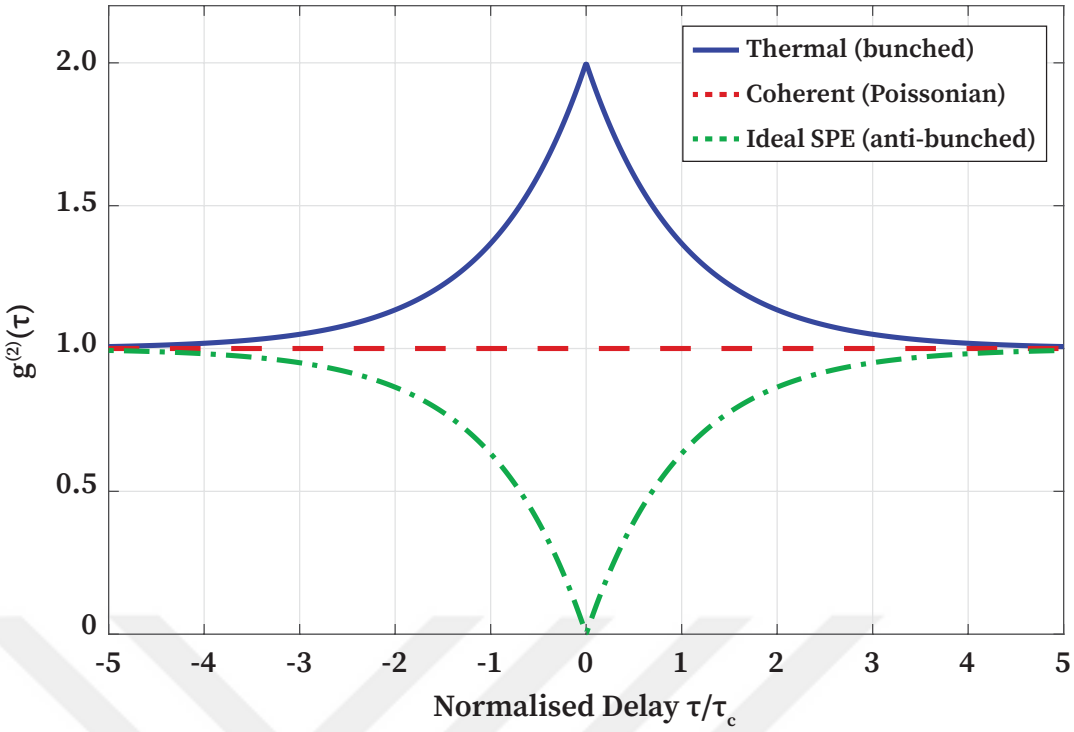

Figure 2.4: Characteristic second-order coherence functions $g^{(2)}(\tau)$ for different types of light sources. Thermal light shows photon bunching with $g^{(2)}(0) = 2$. Coherent light exhibits Poissonian statistics with $g^{(2)}(\tau) = 1$. An ideal single-photon emitter displays perfect photon anti-bunching with $g^{(2)}(0) = 0$, which recovers to 1 for $\tau > 0$. Real SPEs show $0 < g^{(2)}(0) < 0.5$.

light (Poissonian) exhibits a flat line at $g^{(2)}(\tau) = 1$, indicating no correlation between photon detection events at any time delay. In contrast, an ideal single-photon emitter (sub-Poissonian) shows a distinct anti-bunching dip, with $g^{(2)}(0) = 0$, signifying that no two photons are emitted simultaneously. This dip then recovers towards $g^{(2)}(\tau) = 1$ on a timescale often related to the emitter's excited state lifetime, as the system becomes ready to emit another photon after a characteristic recovery period. For realistic SPEs, imperfections and background lead to $0 < g^{(2)}(0) < 0.5$, but the anti-bunching dip remains the key signature. Notably, even a highly attenuated pulsed laser with a mean photon number per pulse $\bar{n} \ll 1$ (e.g., $\bar{n} = 0.1$) retains Poissonian statistics and yields $g^{(2)}(0) \approx 1$, distinguishing it clearly from true single-photon sources despite its low photon flux.

Experimentally, $g^{(2)}(\tau)$ is typically measured using a Hanbury Brown and Twiss (HBT) interferometer (*54*). In this setup, light from the source is divided by a 50:50 beamsplitter, with each output path directed to a separate single-photon detector. A time-to-digital converter records the time differences between photon arrival events at the two detectors. A histogram of these time differences, after appropriate normalization, yields the $g^{(2)}(\tau)$ function.

The measurement and analysis of $g^{(2)}(\tau)$ are thus fundamental tools for verifying

the quantum nature of light and for the characterization and validation of single-photon emitters, which are central to many quantum technologies. In the context of this thesis, the measurement of $g^{(2)}(\tau)$ via an HBT setup (introduced in chapter 3) is the definitive experimental method used to confirm the quantum, single-photon nature of the individual emitters investigated in hexagonal boron nitride.

2.1.4. Modeling Single-Photon Emission, Three-Level System

The emission of single photons is most fundamentally described by a quantum two-level system, where an emitter cycles between a ground and an excited state. While this model correctly captures the essential signature of an emitter—photon antibunching at zero time delay ($g^{(2)}(0) = 0$)—it fails to describe more complex photodynamics common in real-world systems (*53*). Specifically, many solid-state emitters, including those in hBN, display fluorescence intermittency (blinking) and an associated photon bunching effect at intermediate time delays (where $g^{(2)}(\tau) > 1$). This behavior indicates that the emitter can be temporarily 'shelved' in a long-lived, non-radiative dark state after excitation (*55*). To accurately account for this shelving mechanism, the two-level picture is extended to a three-level system, which incorporates this third metastable state. This model provides the simplest framework that quantitatively reproduces these experimental observations and is thus fundamental for describing the dynamics of realistic single-photon emitters (*56*).

Three-Level System Model

A three-level system consists of a singlet ground state, an excited state, and a triplet dark (metastable) state, as displayed in Figure 2.5. The system is optically driven by an excitation rate γ_{12}, which promotes population from the ground state to the excited state. The excited state can decay back to the ground state by the transition rate γ_{21}, which encompasses both radiative and non-radiative decay processes.

In addition to these decay processes, an alternative non-radiative pathway known as intersystem crossing (ISC) allows the emitter to transition from the excited singlet state to the triplet dark state at a rate γ_{23}. Since ISC is typically spin-forbidden, this transition occurs with low probability but can significantly affect the emission properties by temporarily shelving the emitter in the dark state. The return transition from the triplet state to the ground state occurs at a rate γ_{31}, which is often slow, further reducing the effective photon emission rate. These processes play a crucial role in determining the

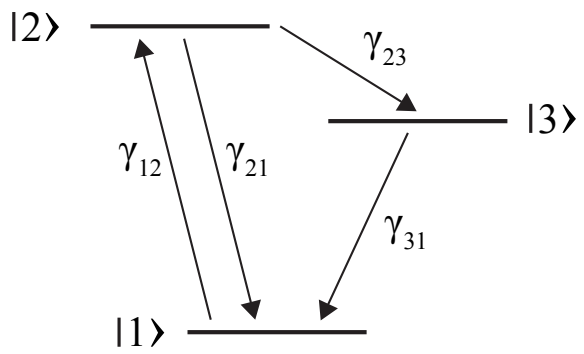

Figure 2.5: Schematic representation of a three-level system. The system consists of a singlet ground state $|1\rangle$, an excited singlet state $|2\rangle$, and a long-lived triplet state $|3\rangle$.

emission efficiency and stability of single-photon sources. The transition rate equations in terms of populations p_i and rates are given by (*56*).

$$\dot{p}_1 = -\gamma_{12}p_1 + (\gamma_r + \gamma_{nr})p_2 + \gamma_{31}p_3, \tag{2.4}$$

$$\dot{p}_2 = \gamma_{12}p_1 - (\gamma_r + \gamma_{nr} + \gamma_{23})p_2, \tag{2.5}$$

$$\dot{p}_3 = \gamma_{23}p_2 - \gamma_{31}p_3, \tag{2.6}$$

$$1 = p_1 + p_2 + p_3. \tag{2.7}$$

In this system, γ_{12} represents the excitation rate induced by an external light source, which drives the population from the ground state to the excited state. The total decay rate from the excited state to the ground state is given by $\gamma_{21} = \gamma_r + \gamma_{nr}$, where γ_r corresponds to radiative emission of a photon and γ_{nr} accounts for non-radiative losses due to interactions with the environment. The transition rate γ_{23} describes the probability of the emitter entering the dark state from the excited state, while γ_{31} governs the slow return of the emitter from the dark state to the ground state. Equation (2.7) ensures population conservation, meaning the emitter always remains in one of the three states.

The steady state of the system is given by assuming that the population p_i for all states remains constant over time. Consequently, their time derivatives are set to zero, and the rate Equations (2.4) - (2.7) become a set of four linear equations.

$$0 = -\gamma_{12}p_1 + (\gamma_r + \gamma_{nr})p_2 + \gamma_{31}p_3, \tag{2.8}$$

$$0 = \gamma_{12}p_1 - (\gamma_r + \gamma_{nr} + \gamma_{23})p_2, \tag{2.9}$$

$$0 = \gamma_{23}p_2 - \gamma_{31}p_3, \tag{2.10}$$

$$1 = p_1 + p_2 + p_3. \tag{2.11}$$

Solving this set of equations for p_2, we find

$$p_2 = \frac{(1 + \gamma_{23}/\gamma_{31})^{-1}}{1 + \frac{1}{\gamma_{12}}\frac{(\gamma_{nr}+\gamma_r+\gamma_{23})}{1+\gamma_{23}/\gamma_{31}}}. \tag{2.12}$$

The rate R at which the system emits photons can be defined as $R = p_2\gamma_r$ in terms of the population of the excited state p_2 and radiative transition rate γ_r. Substituting the population p_2, we find

$$R(P) = R_\infty \frac{P/P_S}{1 + P/P_S}, . \tag{2.13}$$

where P is the power of the excitation light, defined by $\gamma_{12} = P/(\hbar w)$. Two parameters R_∞ and P_S are defined as

$$R_\infty = \gamma_r \left(1 + \frac{\gamma_{23}}{\gamma_{31}}\right)^{-1}, \tag{2.14}$$

$$P_S = \frac{\gamma_r + \gamma_{nr} + \gamma_{23}}{(1 + \gamma_{23}/\gamma_{31})}\hbar\omega, \tag{2.15}$$

indicating the saturated emission rate R_∞ and the excitation power P_s where the emission rate equals $R_\infty/2$. Figure 2.6 illustrates this characteristic saturation behaviour: the normalised emission rate R/R_∞ rises with increasing normalised excitation power P/P_s and asymptotically approaches unity as the intensity becomes much larger than P_s, a consequence of the finite lifetime of the excited state.

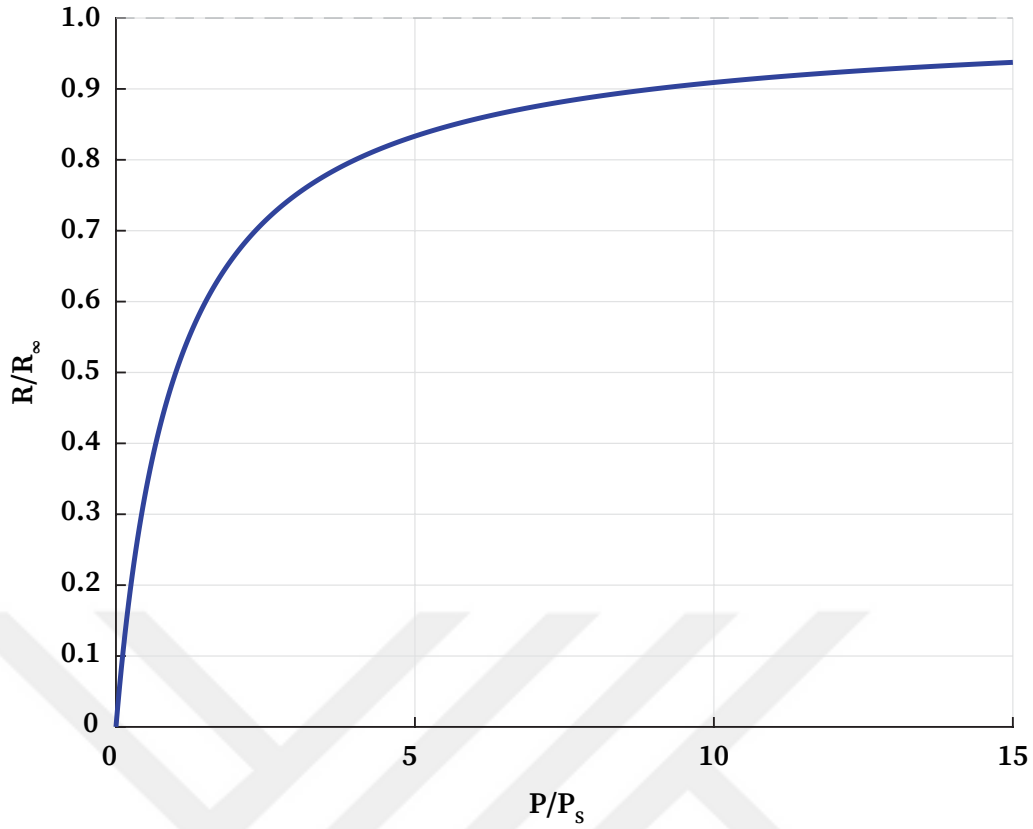

Figure 2.6: Normalized saturation curve of a three-level quantum emitter. The emission rate R is normalized to its maximum value R_∞, and the excitation power P is normalized to the saturation power P_s. The curve follows the functional form $\frac{R}{R_\infty} = \frac{P/P_s}{1+P/P_s}$, demonstrating the characteristic saturation behavior as $P/P_s \to \infty$.

2.1.5. Time-Dependent Analysis of Three-Level System

Although the experimental realization of saturation behavior under increased excitation powers is indicative of a single emitter, definitive identification requires an analysis of the light's statistical properties. This is primarily achieved through measurements of the second-order coherence function $g^{(2)}(\tau)$, as introduced in Section 2.1.3. For analytical modeling of an emitter, particularly a three-level system, $g^{(2)}(\tau)$ (defined by Eq. (2.3)) can be related to the dynamics of the emitter's internal states. Specifically, it can be expressed in terms of the conditional probability of the emitter being in the excited state $|2\rangle$ at time τ, given it was in the excited state and emitted a photon at $\tau = 0$, leading to:

$$g^{(2)}(\tau) = \frac{p_2(\tau|\text{emission at } \tau = 0)}{p_2(\text{steady state})}, \tag{2.16}$$

where $p_2(\tau|\text{emission at } \tau = 0)$ is the probability of finding the system in the excited state $|2\rangle$ at time τ after an emission event at $\tau = 0$, and $p_2(\text{steady state})$ (or $p_2(\infty)$ as you used later) is the steady-state population of the excited state. For a system that has just

emitted a photon and returned to the ground state, $p_2(\tau|\text{emission at } \tau = 0)$ is equivalent to the population $p_2(\tau)$ of an initially unexcited system that evolves over time τ under continuous excitation (*56*). Thus, this is often written as:

$$g^{(2)}(\tau) = \frac{p_2(\tau)}{p_2(\infty)}, \tag{2.17}$$

where $p_2(\tau)$ is the time-dependent population of the excited state (assuming the system starts in the ground state after an emission at $\tau = 0$), and $p_2(\infty)$ is its steady-state value. Solving the rate equations (2.4)–(2.7) for $p_2(\tau)$ and substituting the solution into Equation (2.17), we obtain the following expression for the autocorrelation function (*56*):

$$g^{(2)}(\tau) = -\left(1 + \frac{A_2}{A_3}\right)e^{s_1\tau} + \frac{A_2}{A_3}e^{s_2\tau} + 1, \tag{2.18}$$

where the parameters s_1, s_2, and A_2/A_3 are approximately given by

$$s_1 \approx -(\gamma_{12} + \gamma_{21}), \tag{2.19}$$

$$s_2 \approx -\left(\gamma_{31} + \frac{\gamma_{12}\gamma_{23}}{\gamma_{12} + \gamma_{21}}\right), \tag{2.20}$$

$$\frac{A_2}{A_3} \approx \frac{\gamma_{12}\gamma_{23}}{\gamma_{31}(\gamma_{12} + \gamma_{21})}, \tag{2.21}$$

under the assumption that

$$\gamma_{21} \geq \gamma_{12} \gg \gamma_{23} \geq \gamma_{31}. \tag{2.22}$$

This approximation reflects a typical hierarchy of transition rates in three-level single-photon emitters, where the excitation and decay rates between the singlet ground and excited states (γ_{12} and γ_{21}) are significantly faster than the intersystem crossing (γ_{23}) and the decay from the triplet state back to the ground state (γ_{31}). This separation of timescales is commonly observed in systems where non-radiative relaxation through dark states leads to photon bunching behavior in the autocorrelation function.

Figure 2.7 shows the behavior of second-order autocorrelation function $g^{(2)}(\tau)$, as described by Equation (2.17), for two excitation powers. Three characteristic behaviors can be observed: the antibunching dip at short times, where $\tau \approx 0$, originates from the first term in Eq. (2.18). Photon bunching at intermediate times around $\tau \approx 10^{-7}$ arises due to ISC to the triplet dark state, causing the emitter to remain in the dark state until a spin flip occurs, which is commonly known as the blinking of the emitter (*55*). Lastly, the

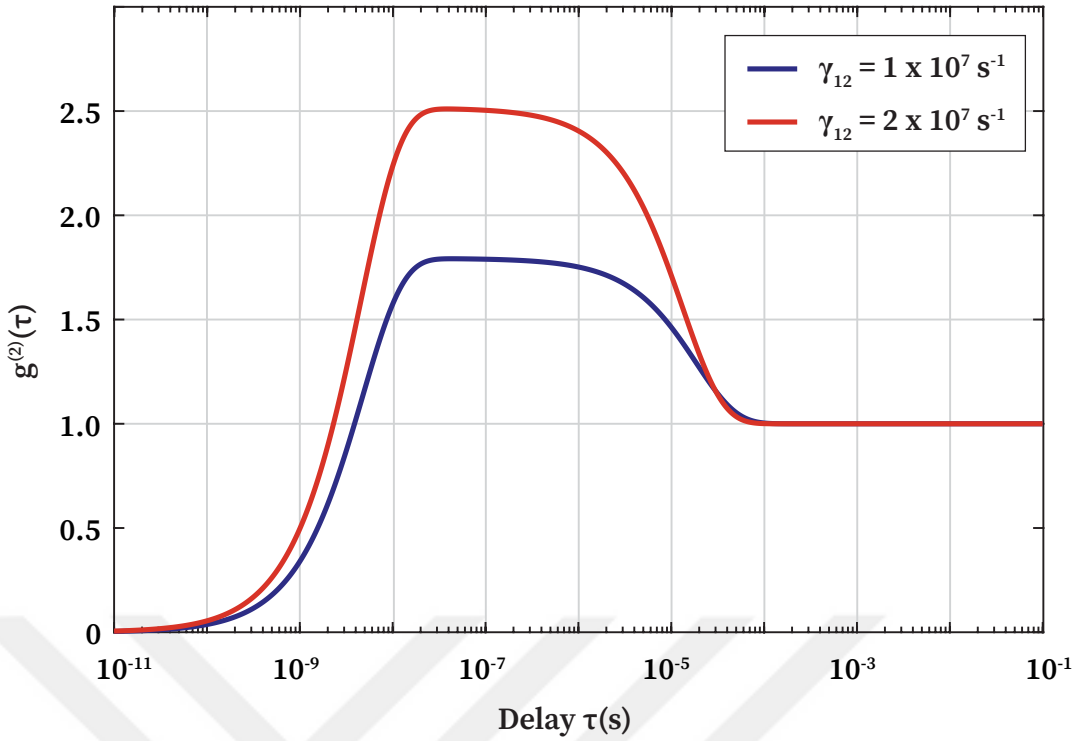

Figure 2.7: Second-order autocorrelation function $g^{(2)}(\tau)$ plotted for two excitation powers. The excitation rates are set to $\gamma_{12} = 1 \times 10^7$ s^{-1}, and 2×10^7 s^{-1}, while the transition rates between the singlet and triplet states are set to realistic values typical to single emitters i.e. $\gamma_{21} = 2 \times 10^8 s^{-1}$, $\gamma_{23} = 5 \times 10^5 s^{-1}$, and $\gamma_{31} = 3 \times 10^4 s^{-1}$.

normalization of $g^{(2)}(\tau)$ at long times indicates the absence of time correlation between detected photons when the delay between detection events is sufficiently long, i.e., for $\tau > 10^{-4}$ seconds.

Additionally, Figure 2.7 illustrates that as the excitation power increases, the bunching amplitude at intermediate times becomes more pronounced. At the same time, the antibunching dip near $\tau = 0$ narrows, reflecting the faster cycling of the emitter between the ground and excited states.

2.2. Fundamentals of Solid-State Single-Photon Sources

Solid-state single-photon sources are integral to many quantum technologies, as outlined in Chapter 1. Platforms such as semiconductor quantum dots, color centers in diamond, and defects in two-dimensional (2D) materials like hBN are particularly valued for their potential scalability and integration capabilities (*7–11*). Figure 2.8 illustrates several prominent examples of these solid-state SPS platforms. Understanding the fundamental optical properties of these emitters within their solid-state environment is crucial

for their development and application, and forms the focus of this section. Key desirable characteristics for any SPS include high single-photon purity ($g^{(2)}(0) \approx 0$), brightness, high collection efficiency, and high indistinguishability (*17*, *24*, *26*).

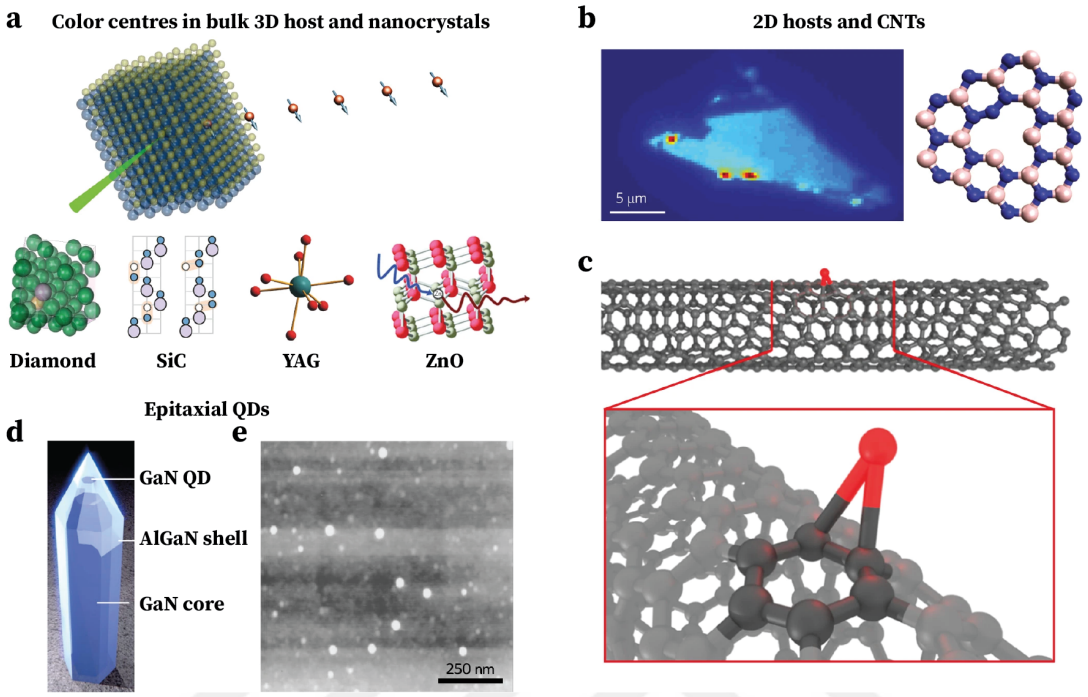

Figure 2.8: Examples of solid-state single-photon emitters across various material platforms. **(a)** Defects in bulk 3D crystals (showcasing diamond, SiC, YAG, and ZnO in insets) and nanocrystals. **(b)** Emitters in 2D hosts: a confocal map illustrating emission from transition metal dichalcogenides such as WSe_2 (left), and defects in hexagonal boron nitride (right). **(c)** Excitons at oxygen-related defects in single-walled carbon nanotubes (CNTs). **(d)** A nitride quantum dot embedded in a nanowire waveguide. **(e)** Self-assembled InAs QDs. Figure reproduced with permission from Springer Nature (*17*), which itself contains material adapted from multiple sources.

2.2.1. Optical Signatures of Emitters in Solid-State Environments

The emission properties of an SPS are intimately linked to its local environment, especially in solid-state systems. The host material can influence the emitter through various mechanisms such as local strain, crystal fields, and, significantly, through interaction with lattice vibrations, or phonons (*31*, *32*). These interactions shape the optical spectrum of the emitter, which typically consists of a sharp Zero-Phonon Line (ZPL) accompanied by Phonon Sidebands (PSBs).

2.2.2. The Franck-Condon Principle and Phonon Coupling

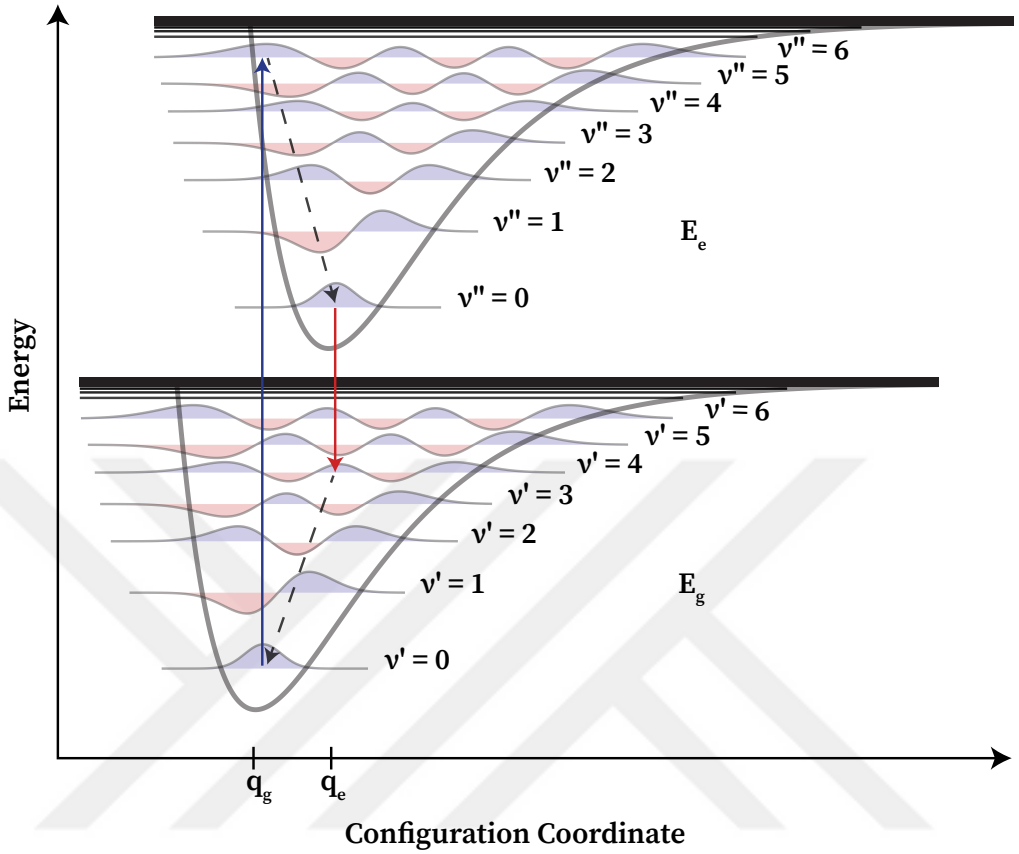

Figure 2.9: The Franck-Condon principle for a solid-state emitter, shown on a configuration coordinate diagram with ground (E_g) and excited (E_e) electronic states, their respective vibrational levels (v'), and equilibrium configurations (q_g, q_e). Arrows illustrate: optical **absorption** (solid blue) to a higher vibrational level in E_e, followed by non-radiative relaxation (dashed black); and subsequent optical **emission** (solid red, depicting a PSB transition) to a higher vibrational level in E_g, followed by non-radiative relaxation (dashed black). An emission transition of $v'' - v' = 0$ would correspond to the ZPL.

The characteristic spectral shape of solid-state emitters, featuring a ZPL and associated PSBs, can be understood through the Franck-Condon principle. This principle, initially developed for molecules, describes the electronic (vibronic) transitions between different electronic states where the nuclear coordinates of the system do not instantaneously change during the rapid electronic transition. In a solid-state defect, the **nuclei** correspond to the defect atoms and the surrounding lattice ions.

Figure 2.9 illustrates this principle using a configuration coordinate diagram. The diagram shows the potential energy surfaces of the ground (E_g) and excited (E_e) electronic states of the emitter as a function of the configuration coordinate. The minima of these potentials, representing the equilibrium configurations of the system, are located at q_g for

the ground state and q_e for the excited state, indicating a horizontal offset due to different equilibrium geometries. Each electronic state possesses a set of quantized vibrational (phononic) levels (labeled v').

During optical excitation (absorption), the system transitions from the ground electronic state (typically its lowest vibrational level at low temperatures) to the excited electronic state. According to the Franck-Condon principle, this transition is vertical on the configuration coordinate diagram, meaning the nuclear configuration remains fixed. If the potential energy surfaces of the ground and excited states are offset horizontally (due to different equilibrium geometries, as indicated by q_g and q_e in Figure 2.9), the system will likely land in a higher vibrational level of the excited state. The emitter then rapidly relaxes non-radiatively to the lowest vibrational level of the excited state by emitting phonons into the host material, typically on picosecond timescales (*57*).

Subsequently, emission occurs as the system transitions from the lowest vibrational level of the excited electronic state back to the ground electronic state. Again, this is a vertical transition. If the transition occurs to the lowest vibrational level ($v' = 0$) of the ground state without creating any phonons, the emitted photon has an energy corresponding to the ZPL. Alternatively, if the transition terminates on a higher vibrational level of the ground state (as illustrated in Figure 2.9), one or more phonons are created, and the emitted photon has a correspondingly lower energy, contributing to the PSB. The PSB thus provides a map of the phonon modes coupled to the electronic transition of the defect. The relative intensity of the ZPL to the total emission is quantified by the Debye-Waller factor (f_{DW}), which is defined as the ratio of the integrated intensity of the ZPL to the total emission spectrum ($f_{DW} = I_{\mathrm{ZPL}}/(I_{\mathrm{ZPL}} + I_{\mathrm{PSB}})$) (*58*). This factor is temperature-dependent; at higher temperatures, increased phonon occupation leads to stronger PSB emission and a weaker ZPL.

The phonon modes involved are characteristic of the host material and the local environment of the defect. For instance, in 2D materials like hBN, specific lattice phonon modes (e.g., optical phonons with energies in the range of 160-200 meV) are often observed in the PSB of defect emitters, providing valuable information about the emitter-phonon coupling (*14*, *43*). The strength of this coupling affects the spectral width of the ZPL and the overall spectral shape, which are crucial for applications that require spectrally narrow and stable emitters. Therefore, the analysis of an emitter's spectral shape, particularly the ZPL and its associated PSB, is a crucial experimental tool used in the subsequent chapters to characterize individual defects in hBN and probe their coupling to the host lattice.

2.3. Hexagonal Boron Nitride as a Single Photon Source

Following the general principles of optical transitions and photon statistics in solid-state emitters discussed previously in this chapter, hBN has emerged as a prominent 2D material for hosting robust SPEs, as highlighted in Chapter 1 (*59*). Its wide bandgap and ability to host bright, optically stable defects make it a compelling platform for room-temperature quantum emitters (*12*). This section explores the specific properties of hBN relevant to these quantum emitters, focusing on their characteristic features and providing a theoretical foundation for the experimental work presented in this thesis.

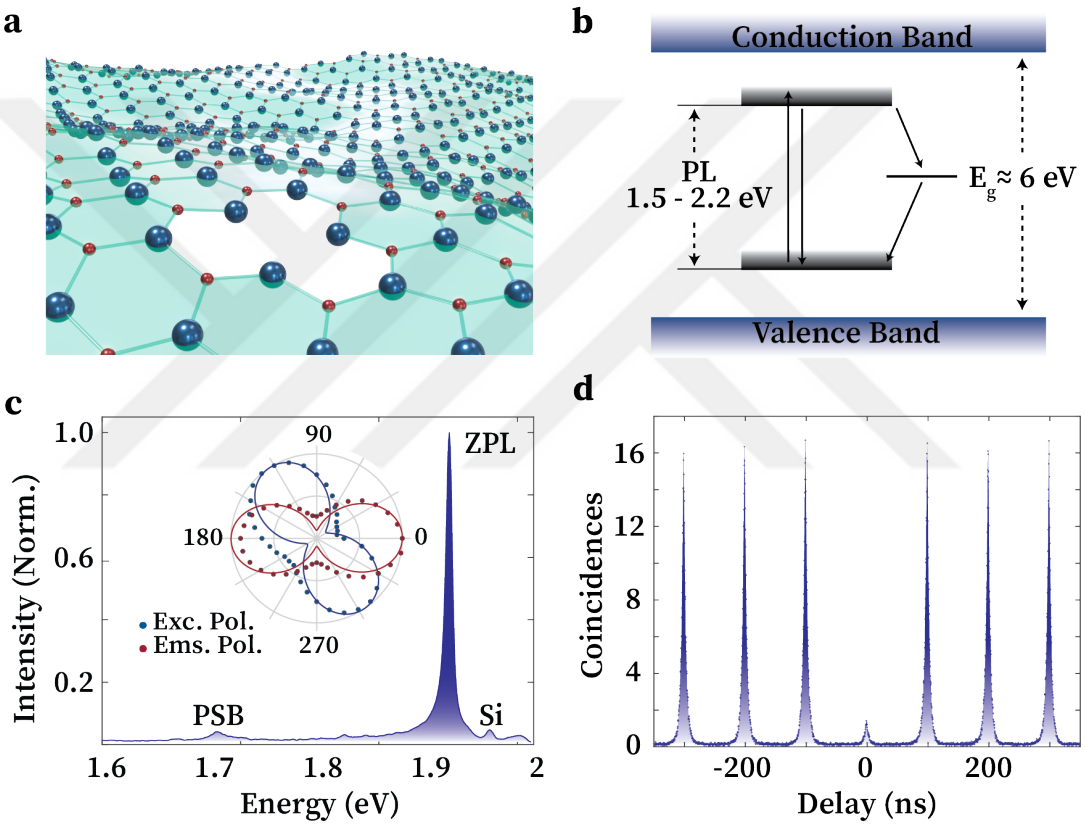

Figure 2.10: Structural, optical, and quantum emission properties of single-photon emitters in hexagonal Boron Nitride. **(a)** hBN honeycomb lattice (Boron: larger blue spheres, Nitrogen: smaller red spheres) with a representative nitrogen vacancy (V_N) defect site. **(b)** Schematic energy band diagram of hBN showing its wide bandgap ($E_g \approx 6$ eV) and a representative intra-gap three-level emitter. **(c)** Typical photoluminescence spectrum of an hBN SPE displaying a ZPL and PSB; inset: characteristic linear excitation and emission polarization. **(d)** Second-order autocorrelation function $g^{(2)}(\tau)$ exhibiting photon antibunching ($g^{(2)}(0) \ll 0.5$), confirming single-photon emission.

The suitability of hBN as a host for SPEs stems from several key material characteristics. Structurally, hBN is a van der Waals crystal composed of hexagonally arranged boron (represented as larger blue spheres in Figure 2.10a) and nitrogen atoms (smaller

red spheres in Figure 2.10a), forming a honeycomb lattice analogous to graphene, often referred to as "white graphene" (*60*). Electronically, it is a wide bandgap insulator, with reported bandgap values typically in the range of 5.8–6.4 eV (*61*), as schematically depicted in Figure 2.10b. This significant energy gap is crucial as it allows for the presence of deep electronic defect levels within the gap, which can act as optically active centers emitting photons across a broad spectral range, well-isolated from the material's band-edge transitions. The vibrational properties of the hBN lattice also play a critical role in shaping the optical spectra of its embedded emitters. hBN possesses a rich phonon spectrum, with distinct high-energy optical phonon modes (e.g., E_{2g} modes) frequently observed with energies in the range of approximately 160–200 meV (*48*). As detailed in the discussion of the Franck-Condon principle (cf. Figure 2.9), the coupling of an emitter's electronic transition to these lattice phonons is responsible for the characteristic PSBs observed in their emission spectra (see Figure 2.10c). Furthermore, hBN exhibits excellent optical transparency, high thermal conductivity, and notable chemical and thermal stability, contributing to the robustness of emitters hosted within it (*15*).

Quantum emitters in hBN have attracted significant attention due to their bright and stable single-photon emission, often observable even at room temperature (*12*). Despite intense research, the precise atomic nature and origin of many SPEs in hBN remain subjects of ongoing investigation and debate (*46*). Current understanding suggests they are often associated with point defects, with common hypotheses including intrinsic defects such as nitrogen vacancies (V_N) or boron vacancies (V_B) (potentially the V_B^- for spin-active defects (*21*)), antisite defects (N_B, B_N) (*62*), and, increasingly, defect complexes involving extrinsic impurities like carbon (e.g., C_BV_N, C_NV_B) (*20*, *47*) or oxygen. This wide variety of potential defect structures is believed to be responsible for the broad distribution of optical and quantum properties observed across different hBN emitters. Structural features, such as wrinkles or localized strain fields, are also thought to play a role (*22*). Various treatments, including annealing or irradiation, are commonly employed to create or activate these emitters (*63*, *64*).

The quantum emitters in hBN exhibit a rich set of optical and quantum characteristics that make them promising for quantum applications. They emit across a broad spectral range from the UV to the near-IR (*59*), with individual emitters typically displaying a sharp ZPL accompanied by a PSB at cryogenic temperatures (Figure 2.10c). The PSB's structure, governed by the Franck-Condon principle (cf. Figure 2.9), reflects coupling to hBN's high-energy optical phonons, and the ZPL intensity relative to the total emission is quantified by the temperature-dependent Debye-Waller factor (f_{DW}) (*65*). Crucially, their

single-photon nature is confirmed by strong photon antibunching in the second-order correlation function, $g^{(2)}(0) \ll 0.5$ (Figure 2.10d), as detailed in Section 2.1.3 (*66*). The excited-state lifetimes are typically in the nanosecond range (*22*, *26*), which influences their maximum emission rates and relates to the transition dynamics described by the three-level system model (e.g., Equations 2.4-2.7).

Many hBN emitters are notably bright and photostable (*12*, *61*), though some may exhibit blinking or spectral diffusion (*41*, *67*). A significant attribute is their often strong linear emission polarization (illustrated in the inset of Figure 2.10c), linked to defect symmetry and orientation within the hBN crystal (*13*, *31*). As highlighted in Chapter 1, a comprehensive understanding and control of these polarization properties, including their dynamics, are central to the research presented in this thesis. Furthermore, their optical properties can be sensitive to the local environment, including strain and electric fields (*32*, *67*), offering pathways for tuning but also presenting challenges for homogeneity.

The diverse family of quantum emitters hosted in hexagonal boron nitride offers a compelling platform for advancing quantum science and technology (*10*, *17*). Their intrinsic brightness, photostability, and operation across a wide spectral range (including at room temperature for many (*16*)) underscore their significant potential, as well as their compatibility with van der Waals heterostructure integration. However, fully realizing this potential necessitates overcoming challenges related to the precise identification of defect structures, achieving deterministic control over emitter placement and spectral properties (*18*, *19*), and mitigating environmental perturbations (*41*). A deeper understanding and refined control of all their emission characteristics, particularly the dynamics of their polarization state as emphasized in Chapter 1, are crucial for tailoring these SPEs for sophisticated quantum applications, forming a key motivation for the work presented in subsequent chapters.

2.4. Mathematical Representation of Light

While the previous sections detailed the physical properties of quantum emitters in hBN, a complete experimental investigation requires a rigorous method to characterize the polarization of the light they emit. A frequent and pivotal observation for many emitters in hBN, including those studied in this work, is that their emission does not always appear to be perfectly linearly polarized; that is, measurements often yield a Degree of Linear Polarization (DoLP) less than one.

This observation presents a critical ambiguity. A low DoLP could arise from two

distinct physical scenarios: the emitter could be intrinsically emitting fully polarized but *elliptical* or *circular* light, or it could be emitting light that is genuinely *partially polarized*-an incoherent mixture of a polarized component and an unpolarized one, resulting in a Degree of Polarization (DoP) less than one. Distinguishing between these possibilities is crucial for understanding the emitter's underlying symmetry and photodynamics. The commonly used Jones formalism, which describes only fully polarized light, is insufficient for this task as it cannot represent an unpolarized component. Therefore, to resolve this ambiguity, the more comprehensive Stokes formalism is required. By allowing for the characterization of any polarization state, the Stokes parameters make it possible to determine the DoP and thus differentiate between elliptically polarized and partially polarized emission. For this reason, the Stokes formalism is an essential tool, not merely a convenient choice, for the in-depth analysis of hBN emitters undertaken in this thesis.

There are three widely adopted formalisms to represent the polarization of light. The polarization vector represents the electric field of a monochromatic plane wave in its raw form, without any simplifications, such as restricting light propagation to a single direction. The polarization vector formalism is commonly used in ray tracing calculations where light propagates in multiple directions and interacts with various components and media that alter its polarization.

Table 2.1: Overview of commonly used representations for polarized light in theoretical and computational optics. Each representation varies in its ability to describe various properties of the light as indicated in the corresponding polarization element column.

Light Representation	Representation Properties	Polarization Element Representation
Polarization Vector	• Monochromatic plane wave in arbitrary direction • Amplitude and phase information • Can describe interference • Cannot describe partially or unpolarized light • Three complex elements	Polarization Ray Tracing Matrices
Jones Vector	• Monochromatic plane wave along z-axis • Amplitude and phase information • Can describe interference • Cannot describe partially or unpolarized light • Two complex elements	Jones Matrices
Stokes Parameters	• Incoherent light along z-axis • Intensity information • Cannot describe interference • Can describe partially or unpolarized light • Four real elements	Mueller Matrices

In most practical cases, light propagates in a single direction, conventionally designated as the z-axis. Such light has no electric field component along the z-axis and, therefore, can be represented by a two-component vector known as the Jones vector. The Jones vector can be seen as a simplified polarization vector with only two complex components. It is still expressed in terms of the amplitude and phase of the electric field. Components that alter polarization can be represented by 2×2 operators, known as Jones matrices. The polarization vector and Jones formalisms cannot describe partially or unpolarized light, where the amplitude and phase of the electric field fluctuate in either preferred or completely random orientations during propagation. One must use a different representation known as Stokes formalism to account for partially and unpolarized light.

The main differences between these three common light representations are summarized in Table 2.1. The appropriate formalism for representing and performing calculations with light must be chosen according to the properties of light and the intended study. Since our study involves partially polarized light, Stokes parameters are appropriate for representing light and performing related calculations.

This chapter provides an overview of Stokes parameters, which serve as a mathematical framework for analyzing completely polarized, partially polarized, and unpolarized light. We then explore the Poincare sphere, a geometrical depiction of polarization states that correlate with Stokes parameters. Additionally, we illustrate how Mueller matrices function as operators for various optical components.

2.4.1. Stokes Polarization Parameters

Stokes parameters of a monochromatic plane wave propagating in the z-direction are defined as (*68*)

$$S_0(t) = \left(\frac{1}{2}\epsilon_0 nc\right)\left[|E_x(t)|^2 + |E_y(t)|^2\right], \tag{2.23}$$

$$S_1(t) = \left(\frac{1}{2}\epsilon_0 nc\right)\left[|E_x(t)|^2 - |E_y(t)|^2\right], \tag{2.24}$$

$$S_2(t) = \left(\frac{1}{2}\epsilon_0 nc\right)\left[E_x(t)E_y^*(t) + E_x^*(t)E_y(t)\right], \tag{2.25}$$

$$S_3(t) = \left(\frac{1}{2}\epsilon_0 nc\right)\left[-iE_x(t)E_y^*(t) + iE_x^*(t)E_y(t)\right], \tag{2.26}$$

Where ϵ, n, and c are the permittivity of vacuum, the refractive index of the medium that light propagates in, and the speed of light, respectively. Dropping the prefactors $\left(\frac{1}{2}\epsilon_0 nc\right)$, which effectively normalizes the parameters to the intensity of the light, and using the definition of the electric field in terms of amplitude and phase, Stokes parameters can be rewritten as

$$S_0(t) = \epsilon_x^2(t) + \epsilon_y^2(t), \tag{2.27}$$

$$S_1(t) = \epsilon_x^2(t) - \epsilon_y^2(t), \tag{2.28}$$

$$S_2(t) = 2\epsilon_x(t)\epsilon_y(t)\ cos[\phi_0(t)], \tag{2.29}$$

$$S_3(t) = 2\epsilon_x(t)\epsilon_y(t)\ sin[-\phi_0(t)], \tag{2.30}$$

where ϵ_i is the amplitude of electric field components and $\phi_0(t)$ is the phase difference between electric field components defined as $\phi_0(t) = \phi_x(t) - \phi_y(t)$. Here, we adopt the notation of reference in (*68*), where $S_3(t)$ is positive for right elliptically polarized light and negative for left elliptically polarized light.

With the definitions above, Stokes parameters are often represented by a column matrix $[S_0\ S_1\ S_2\ S_3]^T$, carrying both intensity and polarization information of a plane wave. Stokes parameters are often used in their normalized form, where all parameters are divided by S_0, considering a light beam of unit irradiance. To provide a comparative overview, Stokes parameters and Jones vectors for various polarization states are presented in Table 2.2.

In classical electromagnetic theory, the amplitude and phase values of a monochromatic light are time-independent, meaning it is always completely polarized. Therefore, Stokes's parameters for a monochromatic light satisfy the following condition.

$$S_0^2 = S_1^2 + S_2^2 + S_3^2. \tag{2.31}$$

As a result, only three components of the Stokes parameters are independent of each other. For polychromatic or quasi-monochromatic light, on the other hand, the amplitude and phase values of a light beam constantly change with time, resulting in random fluctuation of light as it propagates. However, the fluctuations in the amplitude and phase

Table 2.2: Representative Jones vectors and Stokes parameters for several standard polarization states, including linear, circular, and unpolarized light.

State of Polarization	Jones Vector	Stokes Parameters
Horizontal polarization	$\begin{bmatrix}1\\0\end{bmatrix}$	$\begin{bmatrix}1\\1\\0\\0\end{bmatrix}$
Vertical polarization	$\begin{bmatrix}0\\1\end{bmatrix}$	$\begin{bmatrix}1\\-1\\0\\0\end{bmatrix}$
±45 polarizations	$\frac{1}{\sqrt{2}}\begin{bmatrix}1\\\pm 1\end{bmatrix}$	$\begin{bmatrix}1\\0\\\pm 1\\0\end{bmatrix}$
RC and LC polarizations	$\frac{1}{\sqrt{2}}\begin{bmatrix}1\\\pm i\end{bmatrix}$	$\begin{bmatrix}1\\0\\0\\\pm 1\end{bmatrix}$
Unpolarized light	N/A	$\begin{bmatrix}1\\0\\0\\0\end{bmatrix}$

of quasi-monochromatic light with a sufficiently narrow spectral bandwidth are relatively slow, but not entirely insignificant on the timescale needed to make a measurement. Correct treatment of quasi-monochromatic light can be obtained by replacing the instantaneous intensities in Eqs 2.30 with their time-averaged values, such as

$$S_0(t) = \langle \epsilon_x^2(t) \rangle + \langle \epsilon_y^2(t) \rangle, \tag{2.32}$$

$$S_1(t) = \langle \epsilon_x^2(t) \rangle - \langle \epsilon_y^2(t) \rangle, \tag{2.33}$$

$$S_2(t) = 2\langle \epsilon_x(t)\epsilon_y(t)\ cos[\phi_0(t)] \rangle, \tag{2.34}$$

$$S_3(t) = 2\langle \epsilon_x(t)\epsilon_y(t)\ sin[-\phi_0(t)] \rangle. \tag{2.35}$$

A quasi-monochromatic light field cannot be fully polarized, as this would necessitate a perfectly stationary polarization ellipse. Neither can it be completely unpolarized, since the slow fluctuations of the polarization ellipse's orientation and ellipticity do not

average out completely. This intermediate state is termed partial polarization and, as will be shown, can be defined by the following inequality.

$$S_0^2 \geq S_1^2 + S_2^2 + S_3^2, \tag{2.36}$$

Where the equality holds for completely polarized light, and the greater than sign applies to partially polarized light.

For the unpolarized light, one would expect the time averages in Eqs 2.32-2.35 to become

$$\langle \epsilon_x^2(t) \rangle = \langle \epsilon_y^2(t) \rangle, \tag{2.37}$$

$$\langle cos[\phi_0(t)] \rangle = 0, \tag{2.38}$$

$$\langle sin[\phi_0(t)] \rangle = 0. \tag{2.39}$$

Using these relations, completely unpolarized light is characterized by its intensity along with the following Stokes parameters.

$$\begin{bmatrix} S_0 \\ S_1 \\ S_2 \\ S_3 \end{bmatrix}_{unpol} = \begin{bmatrix} S_0 \\ 0 \\ 0 \\ 0 \end{bmatrix}. \tag{2.40}$$

Degree of Polarization (DoP)

The degree of polarization is a metric for Stokes parameters that characterizes the degree of randomness in a polarization state. By definition, it is written as

$$DoP = \frac{\sqrt{S_1^2 + S_2^2 + S_3^2}}{S_0}, \; 0 \leq DoP \leq 1. \tag{2.41}$$

A light beam with a DoP of 1 is considered completely polarized, and its polarization ellipse always traces the same path. Stokes parameters for such light also satisfy the relation given in Eqn 2.31. Any light that has a DoP between 0 and 1 is called partially polarized and satisfies the inequality given in Eqn 2.36. Figure 2.11 displays the behavior of polarization ellipse for circularly polarized light and +45 degree polarized light concerning decreasing DoP values (*69*). As can be seen from the figures, in the case of completely polarized light (DoP = 1), the polarization ellipse traces a single path, and in the lower values of DoP, the polarization ellipse starts to fluctuate more and more around the main polarization trace, DoP = 0 represents the unpolarized light where polarization ellipse randomly fluctuates with respect to time.

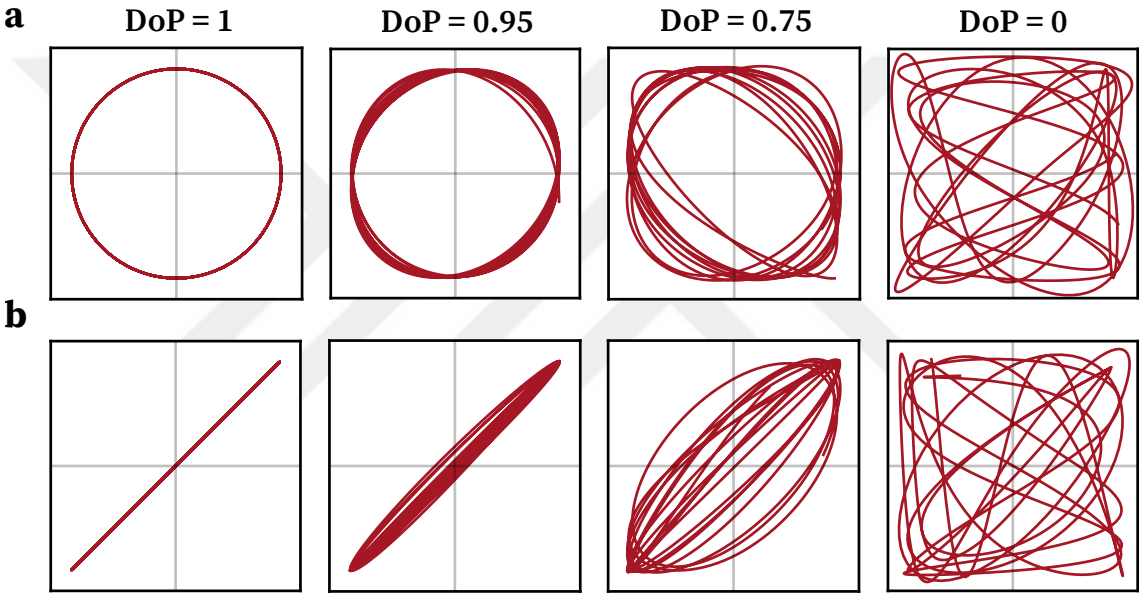

Figure 2.11: Traces of polarization ellipses for **(a)** circularly polarized light with DoP of 1.00, 0.95, 0.75, 0.50, and **(b)** +45 polarized light with DoP of 1.0, 0.8, 0.6, 0.4, 0.2, and 0.

Apart from true DoP, the DoLP can also be defined as follows.

$$DoLP = \frac{\sqrt{S_1^2 + S_2^2}}{S_0}. \tag{2.42}$$

DoLP describes the extent to which the electric field is confined in one plane. When the DoLP equals 1, the light is linearly polarized. By definition, the following relation between DoP and DoLP is always true.

$$DoLP \leq DoP, \tag{2.43}$$

Equality holds when a light beam is linearly polarized, and inequality holds when a light beam has any non-zero circular contribution. Similarly, the degree of circular polarization (DoCP) is defined as

$$DoCP = \frac{S_3}{S_0}. \tag{2.44}$$

The Degree of Circular Polarization quantifies the fraction of total intensity that is circularly polarized, specifying the light's helicity. A value of $DoCP = +1$ corresponds to purely right-handed circularly polarized light, $DoCP = -1$ indicates purely left-handed circularly polarized light, and $DoCP = 0$ is characteristic of light that is linearly polarized, partially linearly polarized, or unpolarized.

Any partially polarized light field can be uniquely described as an incoherent superposition of a completely polarized and a completely unpolarized component. This decomposition is formally expressed using the following Stokes parameters

$$\begin{bmatrix} S_0 + S_0' \\ S_1 \\ S_2 \\ S_3 \end{bmatrix} = \begin{bmatrix} S_0 \\ S_1 \\ S_2 \\ S_3 \end{bmatrix}_{CP} + \begin{bmatrix} S_0' \\ 0 \\ 0 \\ 0 \end{bmatrix}_{UP}, \tag{2.45}$$

Where CP and UP stand for Stokes parameters of completely polarized and unpolarized light, respectively, equation 2.45 can be expressed in an equivalent form.

$$\begin{bmatrix} S_0 \\ S_1 \\ S_2 \\ S_3 \end{bmatrix} = (1 - DoP) \begin{bmatrix} S_0 \\ 0 \\ 0 \\ 0 \end{bmatrix} + \begin{bmatrix} DoP * S_0 \\ S_1 \\ S_2 \\ S_3 \end{bmatrix}, \tag{2.46}$$

Where the DoP satisfies the relations derived before, this decomposition allows the study of a completely polarized part of a partially polarized light.

2.4.2. Poincare Sphere

The Poincare sphere provides a geometric representation of polarization states, simplifying the analysis of polarization transformations, particularly those induced by retarders. The coordinates on the sphere are constructed from the Stokes parameters, expressed in their normalized form as follows:

$$\hat{\mathbf{S}} = \begin{bmatrix} 1 \\ s_1 \\ s_2 \\ s_3 \end{bmatrix} = \frac{\mathbf{S}}{S_0} = \begin{bmatrix} S_0/S_0 \\ S_1/S_0 \\ S_2/S_0 \\ S_3/S_0 \end{bmatrix}. \tag{2.47}$$

where $\hat{\mathbf{S}}$ is the normalized Stokes parameters. The DoP of $\hat{\mathbf{S}}$ becomes

$$DoP = \sqrt{s_1^2 + s_2^2 + s_3^2}. \tag{2.48}$$

For a completely polarized state, the Degree of Polarization is unity (DoP = 1). The normalized Stokes parameters are therefore constrained by the following relation:

$$\sqrt{s_1^2 + s_2^2 + s_3^2} = 1. \tag{2.49}$$

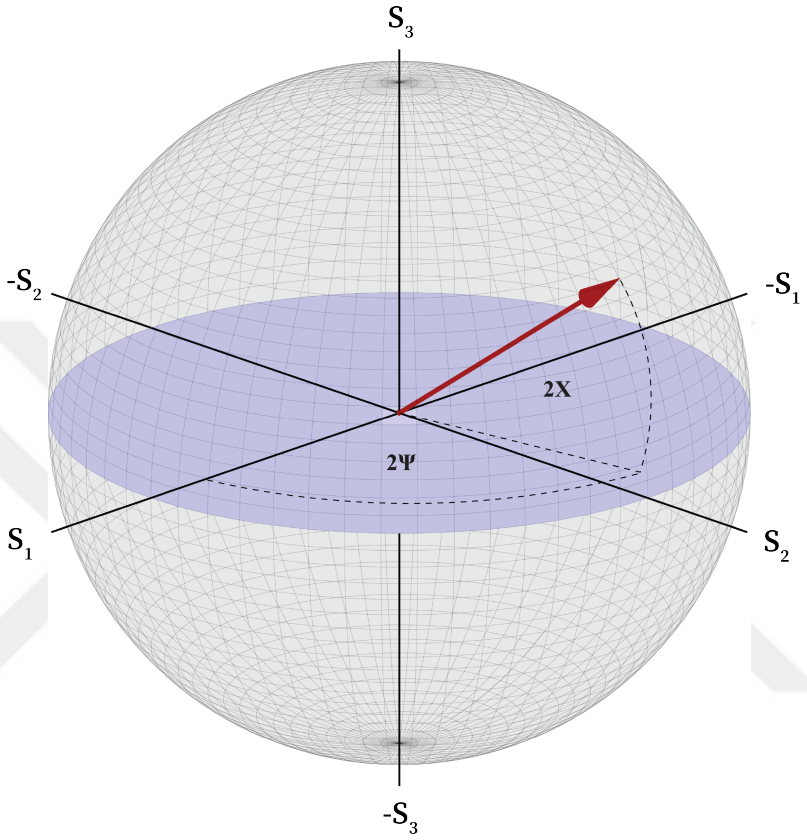

Figure 2.12: The Poincare sphere representation of polarization states and related angular parameters. The axes are defined by the normalized Stokes parameters S_1, S_2, and S_3. The longitude, 2Ψ, and latitude, 2χ, are angles related to the orientation and ellipticity of the polarization ellipse, respectively. The red vector represents an arbitrary state of elliptical polarization.

Each polarization state is mapped to a point (s_1, s_2, s_3) on the Poincare sphere, where the coordinates correspond to the normalized Stokes parameters. The orthogonal axes of this sphere are defined by the basis Stokes parameters $(\pm S_1, \pm S_2, \pm S_3)$, as illustrated in Figure 2.12. All fully polarized states, for which the Degree of Polarization is unity (DoP = 1), lie on the surface of this sphere.

Conversely, states of partially polarized light, for which the Degree of Polarization is less than one ($DoP < 1$), are represented by points located *inside* the sphere. The radial distance of any point from the sphere's origin is equal to its Degree of Polarization. This provides a clear geometric picture: a point at the very center ($s_1 = s_2 = s_3 = 0$) corresponds to completely unpolarized light ($DoP = 0$), while any other point within

the sphere represents a partially polarized state. This also gives a visual interpretation of the decomposition in Equation 2.46, where any partially polarized state can be seen as lying along a vector that points from the origin toward a state of total polarization on the surface.

In this geometric framework, specific regions on the sphere correspond to important classes of polarization. As shown in Figure 2.12, any point on the sphere's surface can also be defined by a longitude 2Ψ and a latitude 2χ. These angles directly describe the physical characteristics of the light's polarization ellipse:

- **The Orientation Angle (Ψ)**: The longitude 2Ψ relates to the orientation of the polarization ellipse. The angle Ψ itself, which ranges from 0 to π, is the angle the major axis of the ellipse makes with respect to the horizontal axis.
- **The Ellipticity Angle (χ)**: The latitude 2χ relates to the shape, or ellipticity, of the ellipse. The angle χ ranges from $-\pi/4$ (left-hand circular) to $+\pi/4$ (right-hand circular). An angle of $\chi = 0$ signifies a line (linear polarization).

This mapping means the equator of the sphere, where $2\chi = 0$, contains all possible states of linear polarization. The North Pole ($s_3 = 1$) and South Pole ($s_3 = -1$) represent perfect right-hand circular (RHC) and left-hand circular (LHC) polarization, respectively. All other points on the surface between the equator and the poles represent the infinite states of elliptical polarization.

The transformation from these spherical coordinates to the Cartesian normalized Stokes parameters is given by:

$$s_1 = \cos(2\chi)\cos(2\Psi) \tag{2.50}$$

$$s_2 = \cos(2\chi)\sin(2\Psi) \tag{2.51}$$

$$s_3 = \sin(2\chi) \tag{2.52}$$

Thus, the Stokes parameters provide a complete algebraic description of a light beam's intensity and polarization, while the Poincare sphere offers an intuitive geometric visualization of its polarization state. Having established how to represent any state of polarization-whether completely, partially, or unpolarized-the next logical step is to describe how these states are transformed when light interacts with optical components, such as polarizers and wave plates. This is accomplished through the Mueller matrix formalism, which provides a powerful and general method for calculating the effect of

optical elements on Stokes vectors.

2.4.3. Mueller Matrices

The Mueller matrix formalism provides a powerful method for analyzing how optical components alter the polarization state of light. In this framework, the transformation of a Stokes vector is described by a linear operation, where the component is represented by a 4x4 real-valued matrix known as its Mueller matrix, **M**. The output Stokes vector is calculated by multiplying the component's Mueller matrix with the input Stokes vector:

$$\begin{bmatrix} S'_0 \\ S'_1 \\ S'_2 \\ S'_3 \end{bmatrix}_{\text{out}} = \begin{bmatrix} M_{11} & M_{12} & M_{13} & M_{14} \\ M_{21} & M_{22} & M_{23} & M_{24} \\ M_{31} & M_{32} & M_{33} & M_{34} \\ M_{41} & M_{42} & M_{43} & M_{44} \end{bmatrix} \begin{bmatrix} S_0 \\ S_1 \\ S_2 \\ S_3 \end{bmatrix}_{\text{in}}, \tag{2.53}$$

where the primed Stokes parameters represent the light after interacting with the optical component. A key advantage of this formalism is its ability to handle both completely polarized and partially polarized light correctly.

For example, consider a normalized, +45Â°-polarized light beam ($[1, 0, 1, 0]^T$) passing through an ideal horizontal polarizer (HP). The calculation, using the matrix for the HP from Table 2.3, is as follows:

$$\frac{1}{2}\begin{bmatrix} 1 \\ 1 \\ 0 \\ 0 \end{bmatrix}_{\text{out}} = \frac{1}{2}\begin{bmatrix} 1 & 1 & 0 & 0 \\ 1 & 1 & 0 & 0 \\ 0 & 0 & 0 & 0 \\ 0 & 0 & 0 & 0 \end{bmatrix}_{\text{HP}} \begin{bmatrix} 1 \\ 0 \\ 1 \\ 0 \end{bmatrix}_{\text{in}}. \tag{2.54}$$

The resulting output vector is $[0.5, 0.5, 0, 0]^T$. This result is physically intuitive: the output light is now horizontally polarized (since $S'_1/S'_0 = 0.5/0.5 = 1$) and its total intensity (S'_0) has been reduced by half, in perfect accordance with Malus's law for a 45Â° angle between the input polarization and the polarizer's axis.

Table 2.3 lists the Mueller matrices for several common optical components. For the general linear polarizer, the angle θ represents the orientation of its transmission axis

Table 2.3: Mueller matrices for common polarization altering components. Angles for polarizers are with respect to the horizontal. For the phase retarders, the slow and fast axes coincide with the horizontal and vertical axes, respectively, with respect to the optical path.

Component	Mueller Matrix
Horizontal polarizer	$M(0) = \frac{1}{2}\begin{bmatrix} 1 & 1 & 0 & 0 \\ 1 & 1 & 0 & 0 \\ 0 & 0 & 0 & 0 \\ 0 & 0 & 0 & 0 \end{bmatrix}$
+45 polarizer	$M(+45^\circ) = \frac{1}{2}\begin{bmatrix} 1 & 0 & 1 & 0 \\ 0 & 0 & 0 & 0 \\ 1 & 0 & 1 & 0 \\ 0 & 0 & 0 & 0 \end{bmatrix}$
General polarizer	$M(\theta) = \frac{1}{2}\begin{bmatrix} 1 & \cos 2\theta & \sin 2\theta & 0 \\ \cos 2\theta & \cos^2 2\theta & \cos 2\theta \sin 2\theta & 0 \\ \sin 2\theta & \cos 2\theta \sin 2\theta & \sin^2 2\theta & 0 \\ 0 & 0 & 0 & 0 \end{bmatrix}$
Half-wave plate	$M(\phi_0 = \pm 180^\circ) = \begin{bmatrix} 1 & 0 & 0 & 0 \\ 0 & 1 & 0 & 0 \\ 0 & 0 & -1 & 0 \\ 0 & 0 & 0 & -1 \end{bmatrix}$
Quarter-wave plate	$M(\phi_0 = \pm 90^\circ) = \begin{bmatrix} 1 & 0 & 0 & 0 \\ 0 & 1 & 0 & 0 \\ 0 & 0 & 0 & \mp 1 \\ 0 & 0 & \pm 1 & 0 \end{bmatrix}$
General phase retarder	$M(\phi_0) = \begin{bmatrix} 1 & 0 & 0 & 0 \\ 0 & 1 & 0 & 0 \\ 0 & 0 & \cos\phi_0 & -\sin\phi_0 \\ 0 & 0 & \sin\phi_0 & \cos\phi_0 \end{bmatrix}$

with respect to the horizontal. For the phase retarders, ϕ_0 is the phase retardance, and the matrices are given for the standard convention where the fast axis is aligned with the vertical (y-axis).

With the Mueller matrix formalism established, we now possess a complete set of tools to both describe any polarization state using Stokes parameters and to model its transformation by optical systems. This comprehensive mathematical framework serves as the foundation for the experimental polarization analysis presented throughout this thesis.

Chapter Summary

This chapter establishes the fundamental theoretical framework required for studying single-photon emitters in solid-state systems. We began by introducing the principles of photon statistics and the second-order coherence function, $g^{(2)}(\tau)$, which serves as the

definitive experimental tool for verifying the quantum nature of an emitter through the observation of photon antibunching. To understand the complex photophysical behavior of real-world emitters, we explored the three-level atomic system, which accounts for phenomena such as saturation and shelving into metastable states. The characteristic optical spectrum of solid-state emitters, comprising a ZPL and PSB, was explained through the Franck-Condon principle, which describes the coupling between the emitter's electronic transition and the host lattice vibrations. These concepts were then contextualized for the specific material of interest, hBN, highlighting the properties that make it an exceptional host for bright, room-temperature quantum emitters.

The second half of the chapter developed the mathematical formalism necessary for the precise characterization of light's polarization. We introduced the Stokes parameters as a comprehensive method for describing any state of polarization, including partially polarized and unpolarized light. The Poincare sphere was presented as an intuitive geometric tool for visualizing these states. Finally, the Mueller matrix calculus was established as a robust framework for modeling the transformation of polarization by optical components.

CHAPTER 3

EXPERIMENTAL METHODS

The experimental study of defects in hBN as SPS requires precise optical characterization techniques to probe their emission properties and validate their quantum nature. The unique properties of hBN defects, including their brightness, stability at room temperature, and often polarized emission, make them promising candidates for quantum information technologies, such as the QKD explored in this thesis (*61*). This chapter outlines the experimental methods employed to investigate the spectral characteristics, decay dynamics, polarization properties, and quantum nature of single-photon emission from hBN defects. The methods described in this chapter serve as fundamental techniques for optical characterization. Additional experimental techniques specific to each investigation are described within their respective chapters.

Room-temperature micro-photoluminescence (μPL) spectroscopy is used to analyze the optical response of individual hBN defects. This technique serves as the initial step in the optical characterization of emitters, providing essential emission properties, such as their spectral signature (including zero-phonon line and phonon sidebands), brightness, and polarization, as well as material-specific properties, including vibrational modes. Identifying and characterizing these spectral features is crucial for selecting suitable emitters for further quantum optical studies and for understanding their interaction with the hBN host material. The polarization of emitted light, a key parameter for investigating the polarization dynamics central to this thesis, can also be readily assessed using μPL. Additionally, Time-Correlated Single Photon Counting (TCSPC) is employed to examine the temporal characteristics of photon emission from defects in hBN. This technique enables the measurement of excited-state lifetimes of emitters, which is fundamental for understanding their quantum efficiency, maximum photon emission rate, and suitability for applications like QKD. It is also crucial for investigating decay time-related polarization effects, which are a core component of the polarization dynamics studied in this work (*44*, *45*). Furthermore, the quantum nature of emission is assessed through second-order photon correlation measurements, which allow for the determination of photon antibunching behavior. This is a key signature of single-photon emission and an indispensable verification step to confirm that an hBN defect behaves as a trustworthy SPS, a prerequisite for its use in QKD protocols (*70*).

Combining these methods provides a fundamental understanding of the optical and quantum properties of hBN emitters, paving the way for their application in quantum technologies. The following sections describe each technique, including the experimental setup, measurement procedures, and data analysis methods.

3.1. Micro-Photoluminescence Spectroscopy

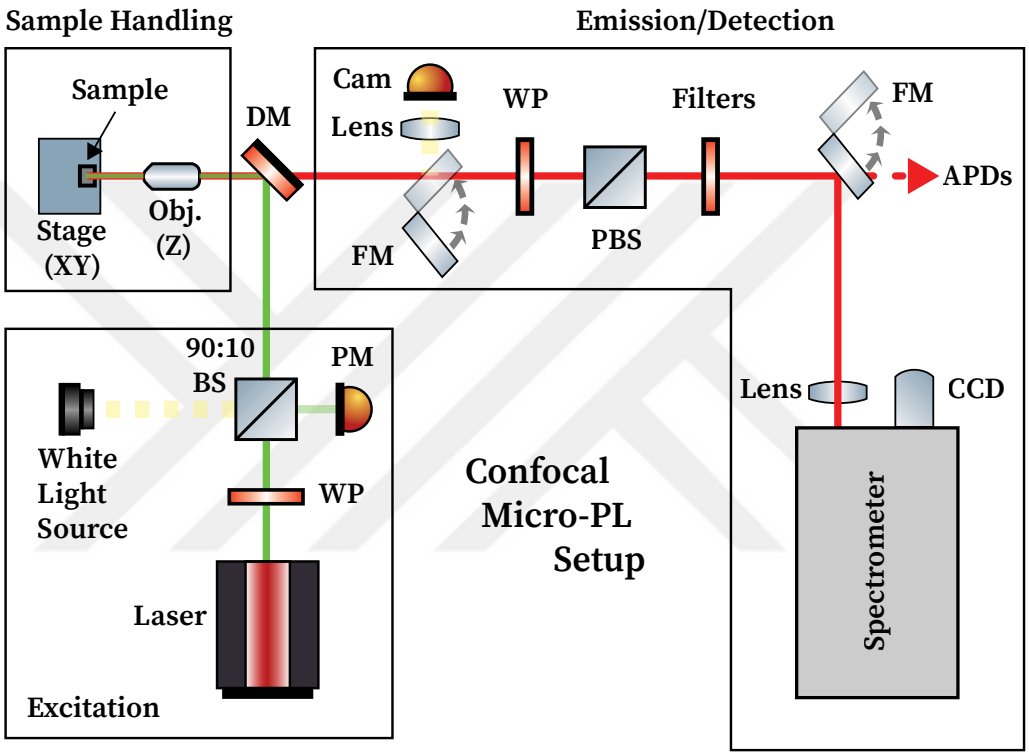

Figure 3.1: Schematic of custom-built confocal micro-PL setup for room-temperature studies of hBN defects with polarization and correlation capabilities. The setup consists of three main paths: excitation, sample handling, and emission/detection. A dichroic mirror directs a laser beam through an objective lens to excite the sample, which is positioned using an XY stage. The same objective collects the photoluminescence, which then passes through the DM and filters. A wave plate and a polarizing beam splitter are used at the start of the emission/detection path for polarization-dependent studies. A flip mirror routes the emission to either a spectrometer and CCD for spectral analysis or to avalanche photodiodes for photon counting and correlation measurements. Key components are abbreviated as: BS: Beam Splitter, WP: Wave Plate, PM: Power Meter, DM: Dichroic Mirror, PBS: Polarizing Beam Splitter, FM: Flip Mirror, APD: Avalanche Photodiode, CCD: Charge-Coupled Device.

Throughout this thesis, defects in solution based hBN flakes have been studied by a custom-built confocal μ-PL setup operating at room temperature, as shown in Figure 3.1. The confocal arrangement is essential for spatially isolating individual hBN defects, which are often sparsely distributed, and for rejecting out-of-focus background fluo-

rescence, thereby improving the signal-to-noise ratio for single emitter studies. The setup can be broadly divided into three main sections: (i) Excitation Path, (ii) Sample Handling, and (iii) Emission & Detection Path. A brief description of each section is provided here.

Excitation Path

- **Laser Source & Polarization Control.** Excitation of hBN defects is achieved using either a continuous-wave (CW) laser or a pulsed laser, depending on the required measurements. CW excitations are performed using a diode-pumped, single-frequency green laser (Verdi V6, Coherent) operating at 532 nm with a 5 MHz (rms) linewidth. This wavelength is commonly used as it efficiently excites a broad range of hBN defects (*12*, *13*). Pulsed excitations are conducted using either a 483 nm or 635 nm laser (PiL048 - PiL063, Pilas - NKT Photonics) operating at repetition rates of up to 80 MHz, with pulse widths of 80 ps and 50 ps, respectively. Pulsed excitation is essential for time-resolved measurements such as TCSPC (Section 3.2) and pulsed $g^{(2)}(\tau)$ measurements (Section 3.3). Before entering the main optical path, the laser passes through a wave plate (WP) to adjust its polarization state. This is important because many hBN defects exhibit anisotropic absorption and emission dipoles (*31*); optimizing the excitation polarization can maximize the excitation efficiency of the emitter and is also used to study excitation polarization anisotropy.

- **Beam Splitter & Power Monitoring.** A 90:10 beam splitter (BS) is used to direct a small fraction (typically 10%) of the beam to a power meter (PM) for real-time monitoring of the laser power. The majority (90%) of the beam continues toward the sample.

- **White Light Source and Imaging Camera.** A white light source combined with a CMOS camera in the detection path is used for locating bulk hBN flakes and for coarse positioning of the laser spot on the sample surface.

- **Dichroic Mirror (DM).** A dichroic mirror (DM) then directs the beam toward the objective lens while allowing the longer-wavelength PL signal from the sample to pass through to the detection arm. The choice of DM is critical to efficiently reflect the excitation laser while transmitting the characteristic Stokes-shifted emission from hBN defects, which typically ranges from ~550 nm to over 800 nm (*17*).

Sample Handling

- **Objective Lens.** A high NA objective lens (50x magnification, 0.90 NA, M Plan Apo HR - Mitutuyo) with adjustable Z-focus (PLSZ, Thorlabs) is responsible for tightly focusing the laser beam onto the hBN sample, aiming to excite individual defects, achieving a laser spot diameter of below 1 micrometer. Emitted photoluminescence and scattered laser are also collected with the same objective. A high NA is crucial for both efficient excitation and collection of the emitted photons from a point-like emitter, which is essential for achieving a good signal-to-noise ratio in single-photon experiments.

- **Sample Stage.** The sample itself is mounted on an XY motorized stage (MLS203, Thorlabs), which enables precise scanning and positioning with a resolution of up to 100 nm. This enables the systematic mapping of hBN flakes to locate and repeatedly address individual emitters.

Emission & Detection Path

- **Polarizing Beam Splitter & Wave Plates.** Polarization selection is performed using a combination of a wave plate (either a half-wave plate or a quarter-wave plate) and a polarizing beam splitter (PBS), which enables polarization-dependent analysis of emitted photons. A motorized rotation mount (PRM1Z8, Thorlabs) automates these measurements, increasing efficiency and reducing measurement-related errors. This component is central to the investigation of polarization dynamics in hBN emitters, a primary focus of this thesis. By rotating the wave plate, the polarization projection axis of the emitted light can be systematically varied, allowing for the determination of parameters such as the DoLP and the orientation of the emission dipole.

- **Spectrometer & CCD:** For spectral analysis, the emission is directed to a spectrometer/monochromator (Shamrock 750, Andor) equipped with a charge-coupled device (CCD - Newton, Andor). The spectrometer features three interchangeable gratings (150 l/mm, 600 l/mm, and 1800 l/mm), offering a spectral resolution of approximately 15 pm. This allows for the detailed characterization of the emission spectrum of hBN defects, including the identification of the ZPL, analysis of phonon sidebands (which provides insight into electron-phonon coupling in hBN (*62*)), observation of spectral diffusion (*67*), and distinguishing between different types of emitters (*47*).

- **Avalanche Photodiodes (APDs):** Alternatively (or in parallel), the emission can

be sent to single-photon detectors by a flip mirror (or via beam splitter) to perform either time-correlated single photon counting or photon-correlation measurements. These detectors are crucial for quantifying the photon flux and performing the quantum optical measurements described in the following sections.

Overall, this custom confocal micro-photoluminescence setup allows for high-resolution spatial mapping, spectral characterization, polarization analysis, and photon-counting measurements of hBN defects at room temperature, providing a comprehensive toolkit for studying their potential as SPSs.

3.2. Time-Correlated Single Photon Counting

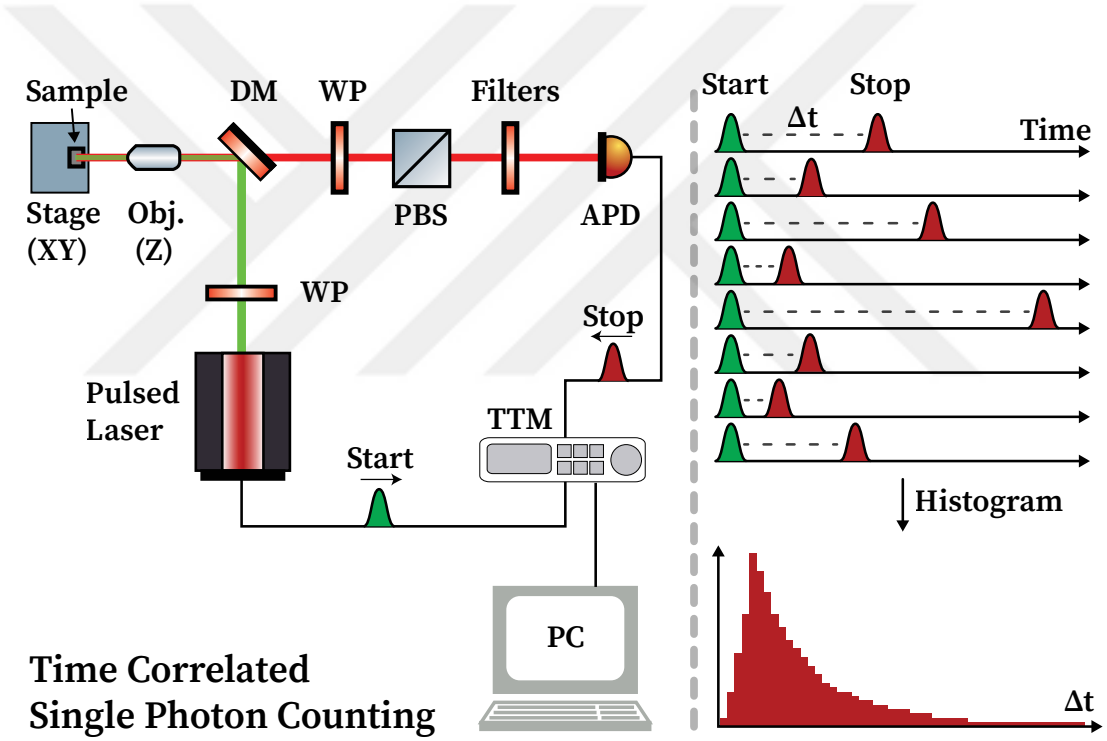

Figure 3.2: Schematic of the time-correlated single photon counting setup for lifetime measurements. A pulsed laser excites the sample, and the emitted photons are detected by an APD. The time intervals between the laser pulse (start) and the detected photon (stop) are recorded by the time tagger module and analyzed on a computer to create a decay histogram of the single emitter.

The TCSPC method is a widely used technique for measuring the fluorescence lifetime of quantum emitters (see Figure 3.2). The excited-state lifetime is a fundamental property of any quantum emitter, including SPSs in hexagonal boron nitride. It dictates the maximum photon emission rate under pulsed excitation, influences the coherence time of emitted photons, and can be affected by the local nano-environment of the defect (via cavities (*71*)) and non-radiative decay pathways (*72*). In this method, the sample is excited

by a pulsed laser source at a suitable wavelength, depending on the emitter. Optical filters in the detection path suppress scattered laser light, select the desired emission band (often centered around the ZPL of the hBN defect), and eliminate unwanted background signals. At the end of the detection path, an avalanche photodiode (APD - ID100 or ID120, ID Quantique) is used as the single-photon detector. Each detected photon generates a "stop" signal, while an internal trigger from the laser provides the "start" signal. These signals are processed by a time tagger module (TTM8000 or QuTools), which measures the time interval (Δt) between the excitation pulse and the detected photon with a resolution of up to 1 ps. These intervals are accumulated to construct a histogram of photon arrival times, shown in the right panel of Figure 3.2.

Depending on the emitter and its photophysics (e.g., presence of shelving states or multiple decay pathways), this histogram can be fitted with an exponential or multi-exponential decay function to extract the fluorescence lifetime(s) of the hBN emitters (*14*). This direct measurement of the excited-state lifetime is a key parameter in characterizing single-photon emitters in hBN and other solid-state systems. For hBN SPSs, typical lifetimes are in the range of a few nanoseconds (*59*), which is compatible with high-speed QKD applications. Furthermore, as investigated in this thesis, time-resolved PL decay measurements at different polarization angles can reveal dynamic changes in polarization during the emission process, providing deeper insights into the complex polarization dynamics of these emitters.

3.3. Second Order Photon Correlation Measurement

Second-order photon correlation measurements (often denoted as $g^{(2)}(\tau)$ measurements) are essential for assessing the single-photon purity of an emitter (see Figure 3.3). The quintessential proof that an observed light source is a true single-photon emitter relies on demonstrating photon antibunching, i.e., a sub-Poissonian photon statistic where the probability of detecting two or more photons simultaneously is suppressed (*52*). This is fundamentally different from classical light sources, such as attenuated lasers. In this technique, the emitter can be excited by either a CW or pulsed laser. After passing through polarization selection and filters (again, to isolate the emission from the specific hBN defect of interest), the collected emission is split into two separate paths by a 50:50 beam splitter. Each path is directed to an individual APD-1 and APD-2, allowing simultaneous detection of photons in two channels. The arrival times of photons at both APDs are recorded by a time tagger module, which assigns timestamps to each detected event.

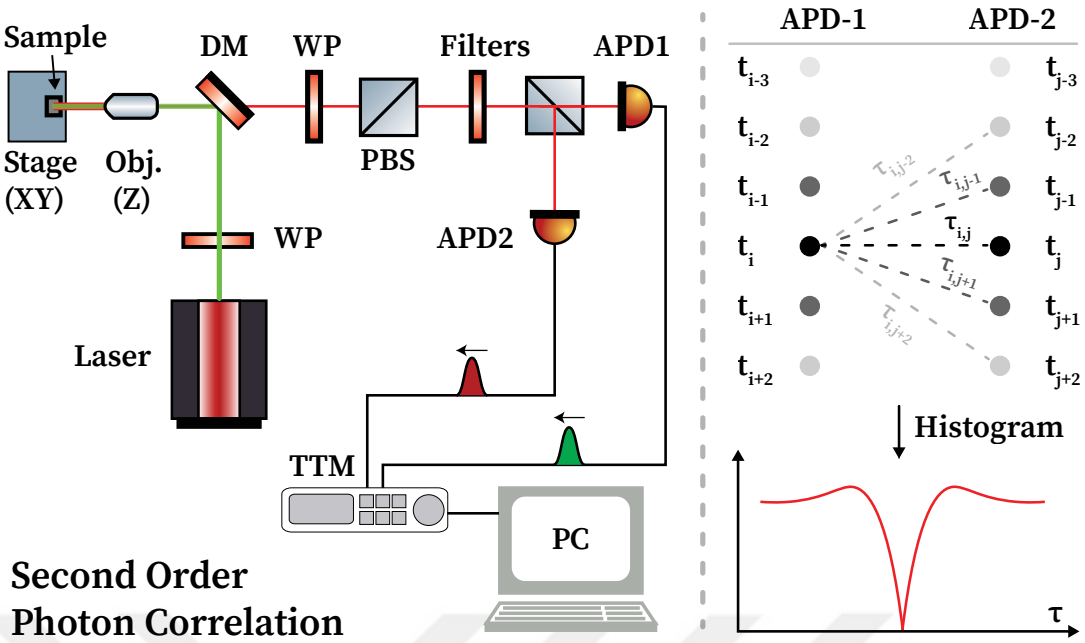

Figure 3.3: Schematic of the second-order photon correlation setup for $g^{(2)}(\tau)$ measurements. Emission is split between two avalanche photodiodes (APD-1 and APD-2), and a time tagger module records photon arrival times. The correlation function $g^{(2)}(\tau)$ is then constructed to evaluate the single-photon purity of the studied emitter.

By comparing the timestamps of APD-1 and APD-2, one constructs a histogram of coincidence counts as a function of the time delay $\tau = t_i - t_j$ (for all i and j values) between detected photons. From this histogram, the second-order correlation function $g^{(2)}(\tau)$ is calculated. For a true single-photon emitter, which can only emit one photon at a time, there should be no coincidence counts at zero time delay ($\tau = 0$), leading to a characteristic dip in the $g^{(2)}(\tau)$ function at $\tau = 0$. A pronounced dip at $\tau = 0$ (i.e., $g^{(2)}(0) < 0.5$) indicates strong antibunching and confirms single-photon emission (*73*, *74*). This measurement is a cornerstone of quantum optics studies involving hBN defects, as it directly reveals the nonclassical nature of the light emitted by these quantum emitters. This validation is particularly critical for many quantum information applications, such as Quantum Key Distribution, as the security of protocols like B92 relies fundamentally on the use of single photons. Any multi-photon component in the emitted stream could be exploited by an eavesdropper via a photon-number-splitting attack, compromising the security of the communication channel (*70*). Thus, demonstrating $g^{(2)}(0) < 0.5$ is an indispensable step in qualifying an hBN defect as a viable single-photon source for quantum applications.

Chapter Summary

This chapter details the fundamental experimental framework used to characterize individual quantum emitters in hexagonal boron nitride at room temperature. The corner-

stone of this framework is a custom-built confocal micro-photoluminescence setup, which enables the spatial isolation and spectral analysis of single defects. We described its key components, including the versatile excitation path that accommodates both continuous-wave and pulsed lasers, the high-NA objective for efficient photon collection, and the sophisticated detection path, which is equipped for high-resolution spectroscopy and automated polarization analysis. This integrated system provides the essential capability to measure an emitter's spectral signature, brightness, and complete polarization state.

Building upon this core setup, we outlined the critical quantum optical techniques employed to validate the non-classical nature of the emission. Time-correlated single photon counting was presented as a method for determining the excited-state lifetimes of emitters, a key parameter governing their temporal dynamics and suitability for high-speed applications. Finally, the principles of second-order photon correlation measurements using a Hanbury Brown and Twiss configuration were described. This technique is indispensable as it allows for the direct observation of photon antibunching ($g^{(2)}(0) < 0.5$), which serves as the definitive proof of single-photon emission and is a fundamental prerequisite for the quantum information applications, such as Quantum Key Distribution, explored in this thesis.

CHAPTER 4

POLARIZATION DYNAMICS OF SINGLE EMITTERS IN HBN

Single-photon emitters are foundational components for a range of emerging quantum technologies, serving as on-demand sources of quantum states of light that are essential for their operation. These emitters are pivotal for applications ranging from quantum computing to quantum communication, where individual photons act as flying qubits, the mobile carriers of quantum information (*75*). The search for an ideal SPE has led to intense investigation across various material platforms, with the most promising candidates including semiconductor quantum dots (QDs), nitrogen-vacancy (NV) centers in diamond, and optically active defects in 2D materials such as hexagonal boron nitride. Each platform offers a unique set of advantages and challenges in the ongoing effort to generate single photons with the requisite purity, brightness, and on-demand characteristics for practical quantum systems (*76*).

The polarization of a single photon is a critical degree of freedom, providing a robust and convenient basis for encoding a qubit. Consequently, the stability and fidelity of this polarization are paramount, as any fluctuation or degradation of the polarization state directly compromises the performance and security of quantum protocols. An unsteady polarization, for example, can limit the key rate and/or increase the errors in quantum communication systems. Critically, polarization stability is inextricably linked to photon indistinguishability, a key requirement for any technology based on quantum interference, such as linear optical quantum computing. If two photons intended to interfere are not identical in their polarization, they become distinguishable, which fundamentally destroys the interference effects upon which these advanced computational schemes are built (*77*).

In this chapter, we investigate the polarization dynamics of single photons emitted from defects in hexagonal boron nitride. By performing a detailed, time-resolved analysis of the polarization state, we aim to characterize and understand the underlying mechanisms that govern its stability, which is crucial for optimizing the performance of these emitters for quantum applications.

4.1. Sample preparation

The quantum emitters central to this study originate from hBN nanoflakes. The samples were prepared by drop-casting a solution containing these nanoflakes onto a silicon substrate, a straightforward method that requires no complex post-processing. The specific hBN nanoflake solution was obtained from Graphene Supermarket and had a concentration of 5.5 mg/L. The flakes within this solution varied in thickness, with the number of atomic layers ranging from one to five atomic layers. The typical flake diameter was between 50 and 200 nm. To prepare the measurement sample, approximately 10 μL of the solution was drop-cast onto a Si/SiO_2 substrate with a 300 nm oxide layer and was subsequently left to dry under ambient conditions. No further post-processing, such as high-temperature annealing, was carried out on these samples. The characterization and polarization dynamics of single emitters found in these nanoflakes are detailed in the subsequent sections.

4.2. Optical Characterization of Emitters

The polarization dynamics of single photons emitted from hBN defects are studied using the custom-built confocal microscopy setup shown in Figure 4.1. For excitation, a 637 nm pulsed laser operating at a repetition rate of up to 80 MHz is used. The laser is delivered through a polarization-maintaining fiber and focused onto the sample by a 50x objective lens, which also collects the resulting photoluminescence. A dichroic mirror (DM) and a long-pass (LP) or notch filter efficiently separate the emission signal from the excitation laser. Two half-wave plates (HWPs) are used in the excitation and emission paths to control the laser polarization for maximum excitation and to analyze the polarization of the collected photons, respectively. After the polarization-analyzing optics, the signal is coupled into either a single-mode fiber (SMF) for enhanced spatial filtering against background light or a multi-mode fiber (MMF) to maximize throughput to the detectors. For initial characterization, the light is directed to a spectrometer with a charge-coupled device (CCD) to measure the photoluminescence (PL) spectrum. To verify the quantum nature of the emitters, the signal is routed to a HBT setup. This configuration measures the second-order correlation function, $g^{(2)}(\tau)$, where an anti-bunching value of $g^{(2)}(0) < 0.5$ provides definitive proof of a single-photon source. Finally, the detailed polarization dynamics are compiled by rotating the emission HWP and recording a full

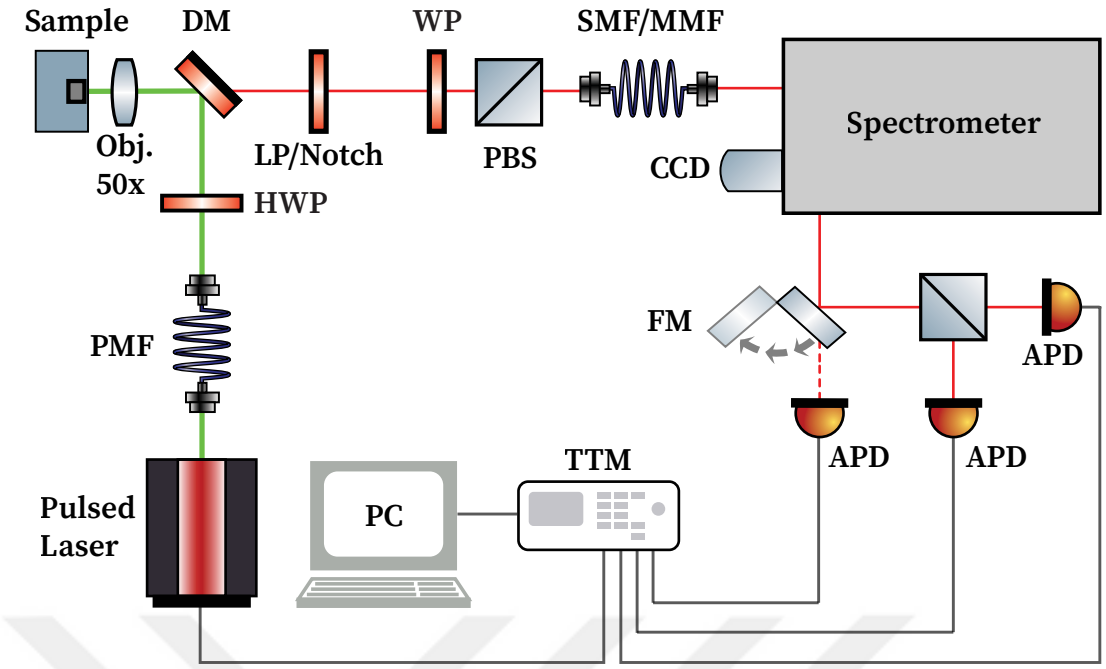

Figure 4.1: Schematic of the confocal micro-PL setup used for optical characterization and polarization-resolved studies of single emitters. Key components are labeled as: PMF: Polarization-Maintaining Fiber, WP: Wave Plate, DM: Dichroic Mirror, LP/Notch: Long-Pass or Notch Filter, PBS: Polarizing Beam Splitter, SMF/MMF: Single-Mode or Multi-Mode Fiber, CCD: Charge-Coupled Device, FM: Flip Mirror, and APD: Avalanche Photodiode. The setup is configured to perform spectral analysis using the spectrometer, time-correlated single-photon counting (TCSPC) for lifetime measurements, and second-order correlation measurements ($g^{(2)}(\tau)$) using the Hanbury Brown and Twiss (HBT) configuration of the APDs.

decay trace for each polarization angle using a single avalanche photodiode. The arrival time of every detected photon is registered by a high-resolution time-tagging module, allowing a PC to reconstruct the time-correlated decay histograms computationally.

Figure 4.2 shows the fundamental optical characterization of a selected candidate emitter for further polarization studies. The room-temperature PL spectrum is shown in panel (a), featuring a dominant ZPL at 647 nm and a corresponding lower-energy PSB around 700 nm. The quantum nature of the defect is highlighted by the power-dependent measurement in panel (b), where the ZPL intensity exhibits clear saturation behavior. This trend is fitted using the standard relation for a three-level system, as previously detailed in Chapter 2:

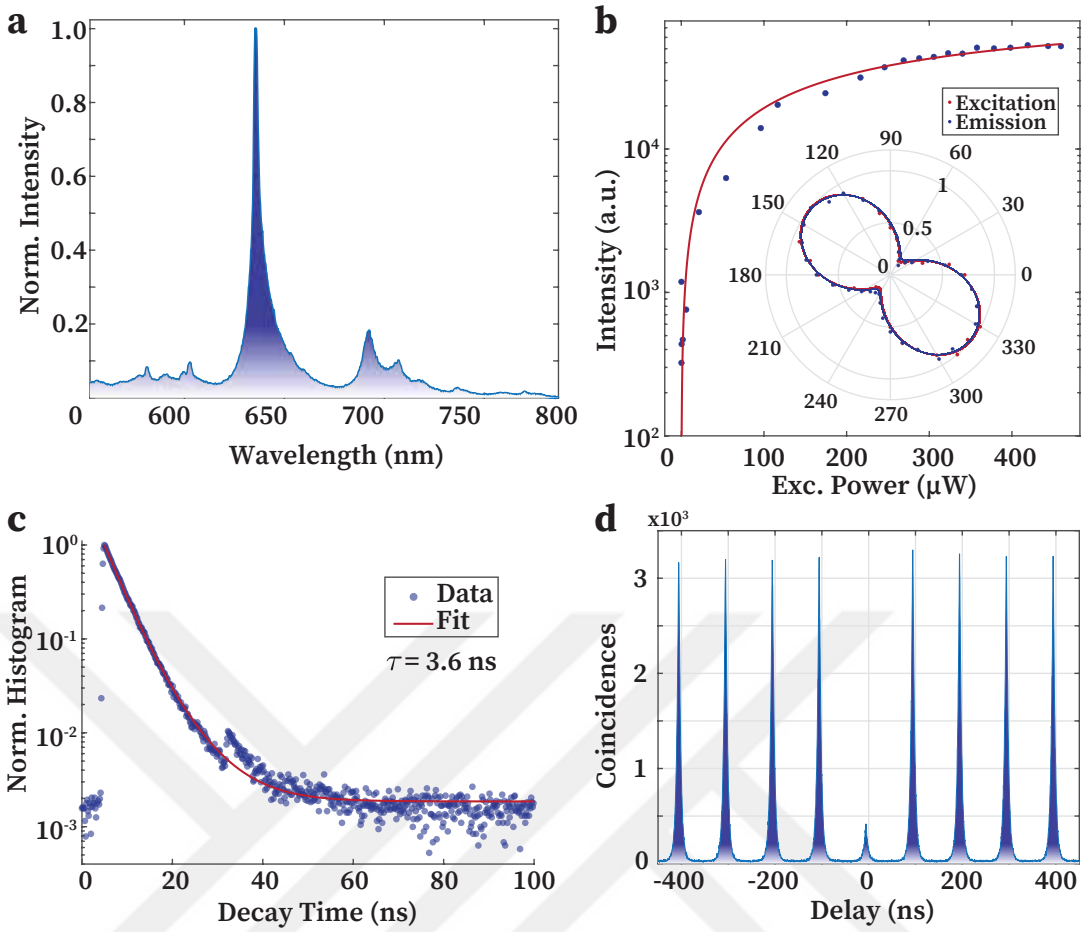

Figure 4.2: Fundamental optical characterization of an hBN quantum emitter used for polarization studies, performed at room temperature. **(a)** Normalized PL spectrum displaying a bright and narrow ZPL at 647 nm and its associated PSB around 700 nm. **(b)** Excitation power-dependent intensity of the ZPL. The inset shows the emitter's dipole nature via its polarization response. **(c)** Time-correlated single-photon counting measurement revealing a lifetime of $\tau = 3.6$ ns from a single exponential fit (red line). **(d)** Second-order photon correlation measurement showing a distinct anti-bunching dip with $g^{(2)}(0) = 0.082$, confirming the single-photon nature of the emission.

$$R(P) = R_\infty \frac{P/P_S}{1 + P/P_S} \tag{4.1}$$

where $R(P)$ is the count rate at a given excitation power P, while R_∞ and P_S are the saturation rate and power, respectively. The fit to the data yields a saturation power of $P_S = 460\,\mu$W, which is well within the capability of our setup, indicating we are operating at maximum brightness for this emitter. The inset polar plot reveals that the excitation and emission polarizations are co-linear, indicating a well-defined optical dipole. The degree of linear polarization (visibility) is calculated from this data using the expression:

$$V = \frac{I_{\max} - I_{\min}}{I_{\max} + I_{\min}} \tag{4.2}$$

This calculation yields a value of approximately 65% for both cases.

The excited state lifetime, measured via TCSPC and shown in panel (c), was analyzed by fitting a biexponential decay function of the form:

$$I(t) = A_1 e^{-t/\tau_1} + A_2 e^{-t/\tau_2} + B_{\text{off}} \tag{4.3}$$

This fit revealed a dominant fast component with a lifetime of $\tau_1 = 3.6$ ns, which is taken as the primary lifetime of the emitter and is consistent with values reported in the literature. The minor peak at 35 ns is an insignificant experimental artifact caused by optical back reflection in the setup. Finally, to confirm the defect as a single quantum source, the second-order autocorrelation function $g^{(2)}(\tau)$ was measured. The pronounced anti-bunching dip at zero delay is fitted using a model for a three-level system to determine its depth precisely:

$$g^{(2)}(\tau) = N\left(1 - c \cdot \left[(1+\alpha)e^{-|\tau|/\tau_1} - \alpha e^{-|\tau|/\tau_2}\right]\right) \tag{4.4}$$

where N is a normalization constant and $c, \alpha, \tau_1, \tau_2$ are fitting parameters that describe the dynamics between the states. The fit of this function to the experimental data yields a value of $g^{(2)}(0) = 0.082$. This value is significantly below the single-photon threshold of 0.5, which confirms the single-photon nature of the emission.

Having confirmed the single-photon nature of the hBN defect, the investigation now shifts to the central theme of this work: the dynamics of its emission polarization. While the initial characterization suggests a stable time-averaged dipole, this does not preclude fast polarization fluctuations that can occur during the nanosecond-scale emission lifetime. Understanding these dynamics is critical, as such fluctuations can compromise the indistinguishability of photons, a key requirement for many quantum protocols. The following section, therefore, presents a detailed, time-resolved analysis designed to reveal how the linear polarization properties of the emitted photons evolve throughout the decay process.

4.3. Polarization Dynamics in Linear Basis

To analyze the polarization dynamics, we performed a series of TCSPC measurements with different emission polarizations by varying the angle of the HWP at the emission port. Polarization is selected by a polarization beam splitter (PBS) after the half-wave plate. The signal is coupled either to a single-mode fiber for additional spatial filtering or to a multi-mode fiber for improved coupling efficiency. All polarization measurements are performed with an experiment time of 1 minute, under the same excitation conditions. The data is then combined into a single polarization-resolved decay map.

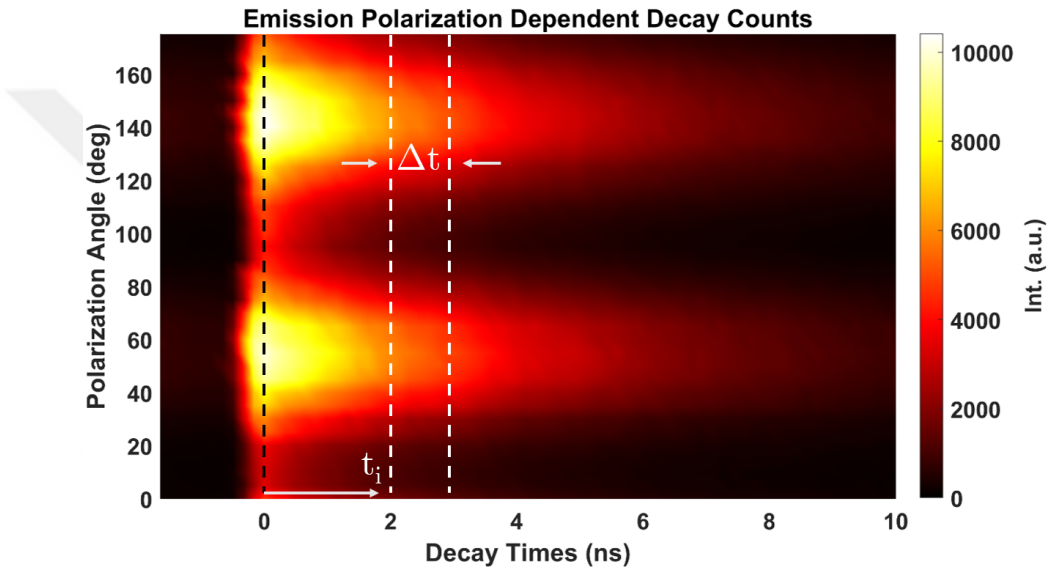

Figure 4.3: Polarization-decay map of an hBN defect created by combining lifetime measurements at different HWP angles from 0 to 360 degrees. The Black dashed line represents the laser pulse. Two white dashed lines represent the boundaries for photons that were emitted between 2 ns and 3 ns.

Figure 4.3 shows the result of such a polarization-decay map. Here, the x-axis represents the decay times of the emitted photons, the y-axis represents the polarization angle of the HWP at the emission port, and the z-axis represents the photon counts in the APDs. This data set can be further analyzed to understand how stable the polarization of single photons is in various decay regions. A Black dashed line at the zero indicates the moment of the excitation pulse, and two white dashed lines represent a region of photons between t_i and $t_i + \Delta t$. Further polarization analysis of this region can be performed to extract the linear polarization visibility of the photons emitted between t_i and $t_i + \Delta t$. In an ideal single emitter, one might expect stable polarization visibility through all segmented regions in this map. Still, the following analysis shows that linear visibility does change with respect to the decay times of the emitter.

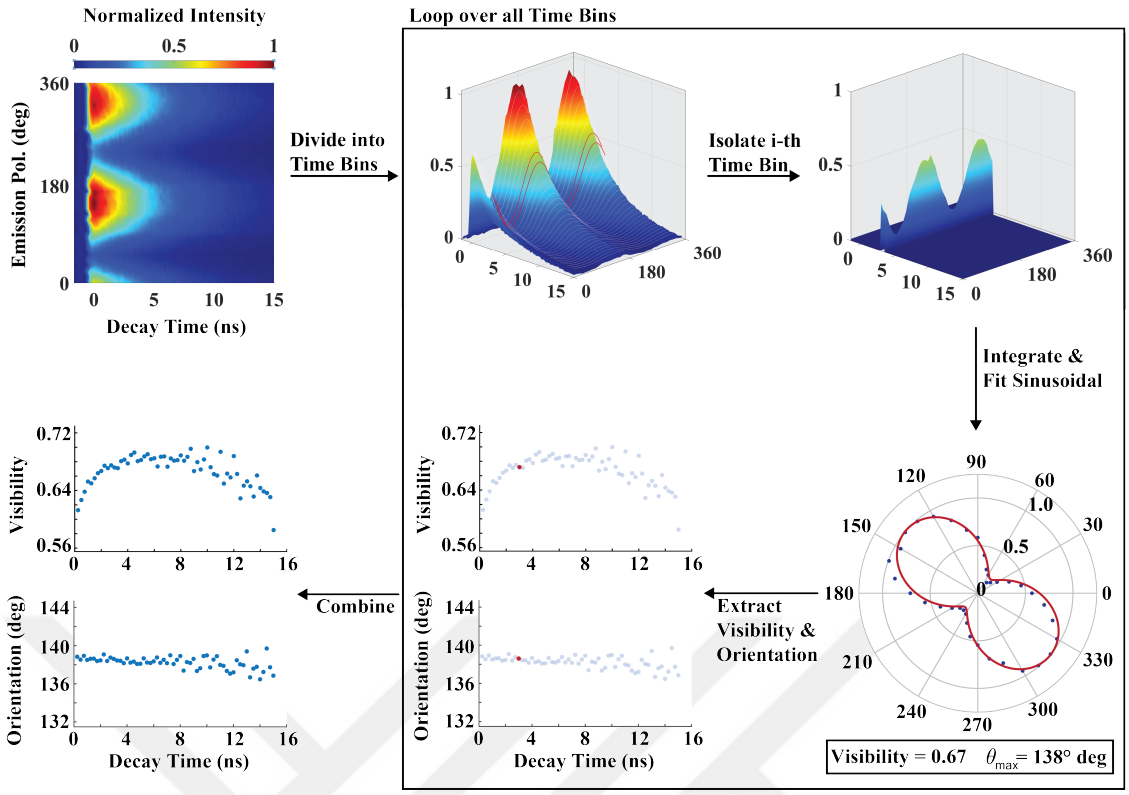

Figure 4.4: Post-process polarization analysis algorithm that we have used to extract visibility and dipole orientation changes of hBN quantum emitters.

Figure 4.4 illustrates the general algorithm used to extract the polarization dynamics of emitters in a linear basis.

- Polarization-decay map is divided into N time bins
- A loop is iterated over all time bins. Loop iteration count i, starts from 1 and goes to N, where N is the last time bin
- for every i-th time bin, segment is excluded, and integrated in time axis to get a total number of counts for every angle value
- This new data of counts versus polarization angle is fit by a cosine function
- linear polarization visibility and emission angle (dipole orientation) is extracted from this data and recorded for every i-th time bin.
- Finally, visibility and dipole orientation for every time bin are combined.

The results of the time-resolved linear polarization analysis, performed using the algorithm described previously, are presented in Figure 4.5. The data reveal significant dynamics in the emitter's polarization properties over its fluorescence lifetime. Panel (a)

shows the evolution of the degree of linear polarization (visibility) with decay time. The visibility exhibits a rapid increase within the first few nanoseconds, rising from an initial value of approximately 62% to a peak of nearly 70%. After this initial rise, visibility remains high and relatively stable for up to 10 ns. At very late decay times (> 10 ns), a slight decline and increased statistical noise are observed, which can be attributed to the decreasing signal-to-noise ratio as photon counts become comparable to detector dark counts.

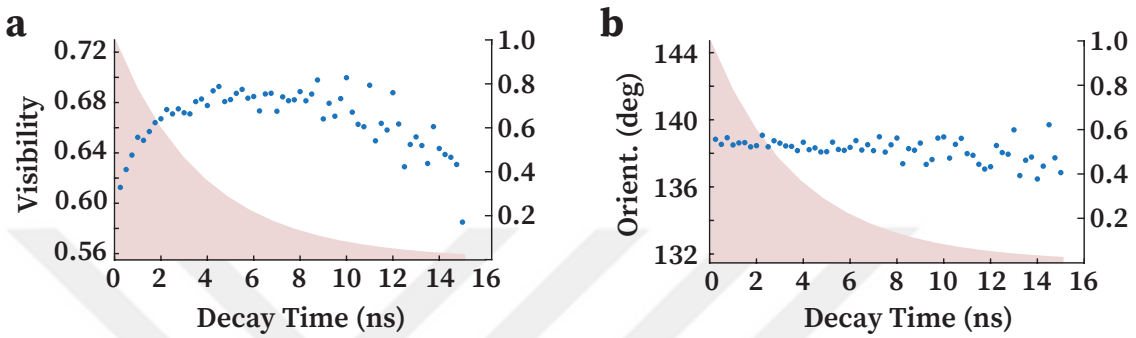

Figure 4.5: Time-resolved linear polarization analysis of the selected hBN single emitter. **(a)** The degree of linear polarization (Visibility) plotted as a function of the photon decay time. **(b)** The orientation of the emission dipole over the same decay period. The shaded red area in both panels represents the photoluminescence intensity decay, indicating the relative population of photons at each time bin.

In stark contrast to the dynamic behavior of the visibility, panel (b) of Figure 4.5 demonstrates that the orientation of the emission dipole is remarkably stable. The orientation remains constant at approximately 138° across the entire measured decay window, with only minor statistical fluctuations around this central value. This indicates that, while the degree of polarization changes after excitation, the physical orientation of the emitter's dipole within the host lattice remains unchanged. In the next section, these findings will be discussed and compared with results from other hBN emitters and diamond NV centers to explore the generality of this phenomenon.

Here we present the combined results of polarization measurements from our hBN samples and Jena's hBN + Diamond samples (*44*). Figure 4.6 displays the polarization-decay maps a_i, visibility changes b_i, and dipole orientation changes c_i with the decay times. Subscript 1 represents the hBN quantum emitters created by electron irradiation using a scanning electron microscope by the JENA group. Subscript 2 represents the hBN quantum emitters in our drop-casted hBN nanoflakes, and finally, subscript 3 represents the NV centers in the diamond prepared by the JENA group. All emitters exhibit similar visibility improvement behavior during the early decay times, indicating a generic mechanism for 2D-based single emitters. Although all emitters exhibit visibility improvement,

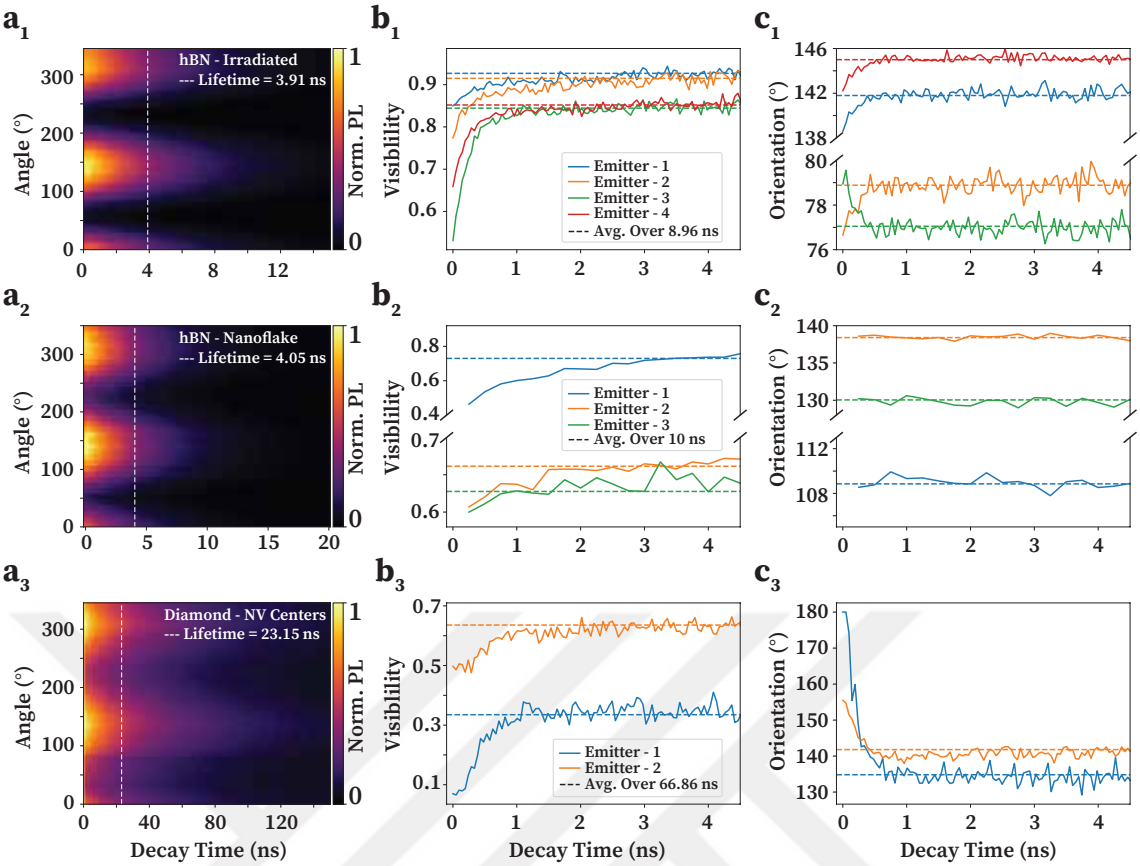

Figure 4.6: Combined polarization analysis of hBN nanoflake quantum emitters (IZTECH), hBN irradiated quantum emitters (JENA), and NV centers of diamond (JENA). All linear degrees of visibility measurements show drastic changes in the early decaying emitters. Irradiated emitters and NV centers also show dipole orientation change in the early times. Reprinted with permission from (*44*). Copyright 2024 American Chemical Society

the rise time of visibility differs among emitters, even in hBN. This distinct rise time of the visibility might depend on the preparation of the samples or how the defects are created in the first place. Dipole orientations, on the other hand, clearly differ between emitters and host material. All irradiated hBN emitters show an apparent change in dipole orientation with respect to decay times, whereas our emitters do not show any change. Orientation change is even more substantial in the NV centers of the diamond, showing 15 degrees to 45 degrees of orientation change in the first nanosecond.

Combined results on polarization analysis show a significant change in the linear degree of polarization and dipole orientation for emitters of hBN and diamond NV centers. Although the effects occur very quickly (under 1 nanosecond for irradiated emitters), they are most pronounced where the emission is strongest, due to the exponential decay curve of the emitters. When averaged, visibility is less than the maximum visibility achieved by the emitter. Similar to the linear degree of visibility, dipole orientation also changes where the emission is strong, resulting in a slightly different averaged dipole

orientation. Finally, not all emitters show similar behaviors regarding visibility rise time and dipole orientation. In our hBN nanoflake quantum emitters, visibility rise is slow compared to irradiated hBN quantum emitters and NV centers of diamond. This discrepancy may be due to sample preparation and the method by which defects are created, and understanding this discrepancy might shed light on the different visibility rise times and dipole orientation changes.

The preceding analysis has conclusively shown that the DoLP of single emitters in both hBN and diamond is not static. Still, it exhibits significant dynamics in the first few nanoseconds following excitation. However, these measurements, performed by projecting the emission onto a linear basis using a half-wave plate and a polarizer, have a fundamental limitation. Specifically, a reduction in the measured DoLP is ambiguous; it can arise either from a genuine, random depolarization process, or from the emission having a static but non-zero *circular* or *elliptical* polarization component, to which the linear analysis is insensitive. To distinguish between these scenarios and identify the actual underlying physical mechanism, a more complete characterization of the polarization state is required. Therefore, this study expands upon the initial work by employing a complete Stokes polarimetry technique to measure the true Degree of Polarization and track its evolution over the emitter's lifetime, thereby resolving the ambiguity in linear basis measurements.

4.4. Polarization Dynamics with Stokes Parameters

To resolve the ambiguity in linear polarization measurements, a complete Stokes analysis is necessary. This section details the theory and application of the RQWP method, a practical and robust technique for measuring the complete polarization state of light. This approach is applied to two representative hBN single-photon emitters, labeled Emitter-1 and Emitter-2, to perform both time-averaged and, for the first time, time-resolved Stokes polarimetry.

We also present our experimental results on Stokes polarization analysis for two hBN emitters labeled emitter-1 and emitter-2. The results are organized as follows. First, we present the basic optical characterization of emitter-1 and emitter-2, along with the experimental setup used in both time-averaged and time-resolved studies. Next, we present the time-averaged Stokes polarization analysis of emitter-1 and discuss the advantages of using Stokes analysis over widely adopted polarization analysis techniques. Finally, we present the time-resolved Stokes polarization analysis of emitter-2, showing an interest-

ing behavior of emitter-2 at early decay times. Finally, we speculate and discuss the two possible mechanisms responsible for the changes in the DoP and DoLP of the emitters.

4.4.1. Rotating Quarter Wave-Plate Method

The classical method of measuring Stokes parameters of a light beam involves four wave-plate measurements at fixed orientations combined with a rotatable linear polarizer. Three measurements require an HWP and a linear polarizer, whereas the last requires a QWP combined with a linear polarizer. There are two main problems with the classical method. Firstly, the classical method only requires four data points to calculate the Stokes parameters, thereby increasing the likelihood of measurement errors. Secondly, introducing another wave plate into the optical path is prone to deflect light, and in some cases, it can affect the optical alignment of the system.

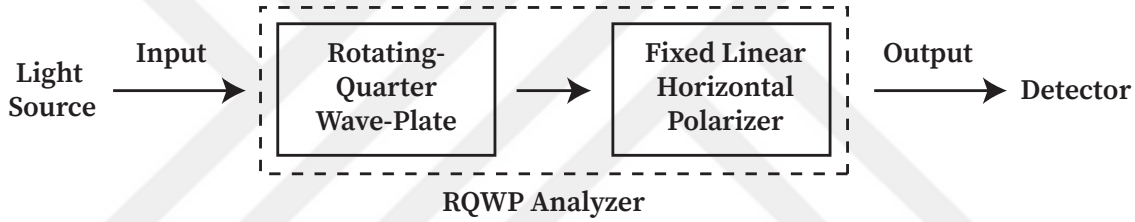

Figure 4.7: Schematic diagram of the RQWP polarimetry method used for measuring Stokes parameters. The setup consists of a rotatable QWP followed by a linear polarizer, which is fixed with its transmission axis oriented horizontally. To perform a measurement, the QWP is rotated through a series of angles (θ), and an optical detector records the intensity of the light that passes through the fixed polarizer. This angle-dependent intensity data is then used to mathematically reconstruct the full Stokes parameters of the input light beam.

An alternative method for measuring Stokes parameters is the Rotatable Quarter-Wave Plate (RQWP) technique, which uses a rotating QWP followed by a fixed linear polarizer with a horizontal transmission axis (*78*). The measurement configuration is depicted in Figure 4.7. For this setup, the optical intensity $I(\theta)$ at the detector is a function of the QWP rotation angle θ and can be written in terms of the incident Stokes parameters as

$$I(\theta) = \frac{1}{2}\left(S_0 + S_1 \cos^2 2\theta + S_2 \cos 2\theta \sin 2\theta + S_3 \sin 2\theta\right). \tag{4.5}$$

The Stokes parameters in Equation 4.5 describe the optical beam entering the measurement system. By applying trigonometric half-angle identities, this expression can be re-

formulated into the following truncated Fourier series:

$$I(\theta) = \frac{1}{2}\left(A + B\sin 2\theta + C\cos 4\theta + D\sin 4\theta\right), \tag{4.6}$$

where the coefficients are related to the Stokes parameters by

$$A = S_0 + \frac{S_1}{2}, \quad B = S_3, \quad C = \frac{S_1}{2}, \quad D = \frac{S_2}{2}. \tag{4.7}$$

Equation 4.6 shows the intensity signal is composed of second and fourth harmonic terms in θ. To determine the coefficients A, B, C, and D, one must sample $I(\theta)$ at a sufficient number of angles. The highest frequency components present are the fourth harmonics, corresponding to the $\cos(4\theta)$ and $\sin(4\theta)$ terms. The Nyquist-Shannon sampling theorem states that the sampling rate must be more than twice the highest signal frequency to avoid aliasing (*79*). Therefore, to resolve the fourth harmonic, more than $2 \times 4 = 8$ measurements are needed over a full 360° period. This establishes that a minimum of eight data points must be acquired within the system's unique 180° operational range.

Because discrete intensities are measured, Equation 4.6 is recast as

$$I_n = \frac{1}{2}\left(A + B\sin 2\theta_n + C\cos 4\theta_n + D\sin 4\theta_n\right), \quad (n = 1, 2..., N) \tag{4.8}$$

where N is an even number equal to or greater than 8. The coefficients A, B, C, and D are determined using familiar methods from Fourier analysis and are given by

$$A = \frac{2}{N}\sum_{n=1}^{N} I_n, \qquad B = \frac{4}{N}\sum_{n=1}^{N} I_n \sin 2\theta_n, \tag{4.9}$$

$$C = \frac{4}{N}\sum_{n=1}^{N} I_n \cos 4\theta_n, \qquad D = \frac{4}{N}\sum_{n=1}^{N} I_n \sin 4\theta_n. \tag{4.10}$$

In Equation 4.10 the angular intervals are equal and are given by $\theta_{n+1} - \theta_n = 180°/N$.

From Equation 4.7 the Stokes parameters are found to be

$$S_0 = A - C, \quad S_1 = 2C, \quad S_2 = 2D, \quad S_3 = B. \tag{4.11}$$

Once the Stokes parameters are found, other features of the Stokes formalism can be calculated using the methods introduced in the previous chapter. One of the main advantages of the RQWP method over the classical measurement of Stokes parameters is its practicality. Since there is only one rotating component in the setup, automating the system with external software is much easier. Additionally, using a large number of data points (N) significantly greater than the minimum of 8 reduces statistical errors in the measurement through averaging.

4.4.2. Characterization of hBN emitters

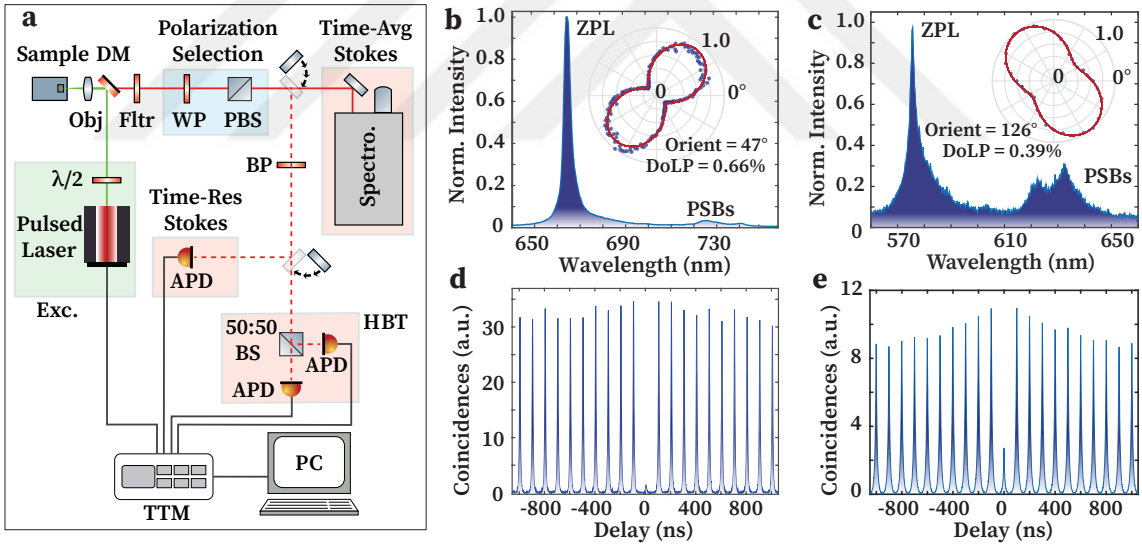

Figure 4.8: Optical characterization of Stokes polarization analysis candidates; Emitter-1 and Emitter-2. **(a)** Schematic of the micro-photoluminescence setup used for optical spectroscopy and polarization analysis of the emitters. **(b)** Normalized PL spectrum of Emitter-1 at room temperature, with its ZPL at 664 nm and characteristic PSB emission around 730 nm. The inset shows the linear polarization analysis, indicating a DoLP of 0.66 and a dipole orientation of $\Psi = 47°$. **(c)** Normalized PL spectrum of Emitter-2, with a ZPL at 575 nm and PSB emission around 630 nm. The inset shows its corresponding linear polarization measurement, with a DoLP of 0.39 and an orientation of $\Psi = 126°$. **(d, e)** Second-order photon correlation measurements for the ZPL emission of Emitter-1 and Emitter-2, respectively. The strong antibunching values of $g^{(2)}(0) = 0.035 \pm 0.002$ for Emitter-1 and $g^{(2)}(0) = 0.36 \pm 0.005$ for Emitter-2 unambiguously confirm their single-photon nature.

The fundamental optical properties of the two hBN defects selected for this study, Emitter-1 and Emitter-2, are summarized in Figure 4.8. The experimental setup used for all measurements is shown in panel (a). The room-temperature PL spectrum of Emitter-1, acquired under 483 nm pulsed excitation with an 80 MHz repetition rate, is displayed in panel (b). It is characterized by a sharp ZPL at 664 nm, corresponding to an energy of 1.87 eV. The associated emission features two distinct PSBs at 727 nm and 743 nm, which correspond to coupling with signature optical phonon modes of hBN at 160 meV and 200 meV, respectively (*80*). The inset presents the results of a linear polarization analysis, which yields a dipole orientation of $\Psi = 47°$ and a DoLP of 0.66. Similarly, the PL spectrum for Emitter-2, shown in panel (c), exhibits a prominent ZPL at 575 nm with corresponding PSBs around 630 nm. Its linear polarization analysis reveals a distinct dipole orientation of $\Psi = 126°$ and a DoLP of 0.39. To verify the quantum nature of the emission, second-order photon correlation measurements were performed for both defects. The results, shown for Emitter-1 in panel (d) and Emitter-2 in panel (e), confirm strong photon antibunching. The correlation values at zero time delay were measured to be $g^{(2)}(0) = 0.035 \pm 0.002$ for Emitter-1 and $g^{(2)}(0) = 0.36 \pm 0.005$ for Emitter-2, unambiguously validating their operation as true single-photon sources.

Having confirmed the single-photon nature and fundamental spectral properties of both emitters, the investigation now proceeds to a detailed analysis of their polarization states. Of particular interest is the observation from Figure 4.8 (b) that Emitter-1 has a DoLP of around 70%. To determine whether this value is due to a genuine random depolarization effect or a static, elliptical polarization state, a time-averaged Stokes analysis was first performed on this emitter, as detailed in the following section.

4.4.3. Time-Averaged Stokes Polarization Analysis of Emitter 1

A time-averaged Stokes analysis was performed on Emitter-1 to determine its complete, time-integrated polarization state. The results of this measurement, conducted using the RQWP technique, are summarized in Figure 4.9. The top panel (a) shows the polarization-resolved spectral map, recorded as a function of the QWP angle, while the bottom plot shows the spectrally resolved DoP extracted from this data. The emission is almost perfectly polarized at the center of the ZPL (664 nm), reaching a DoP of 99%. However, the DoP decreases for wavelengths detuned from the ZPL, which is consistent with phonon-induced depolarization mechanisms previously observed in hBN emitters (*13*, *32*).

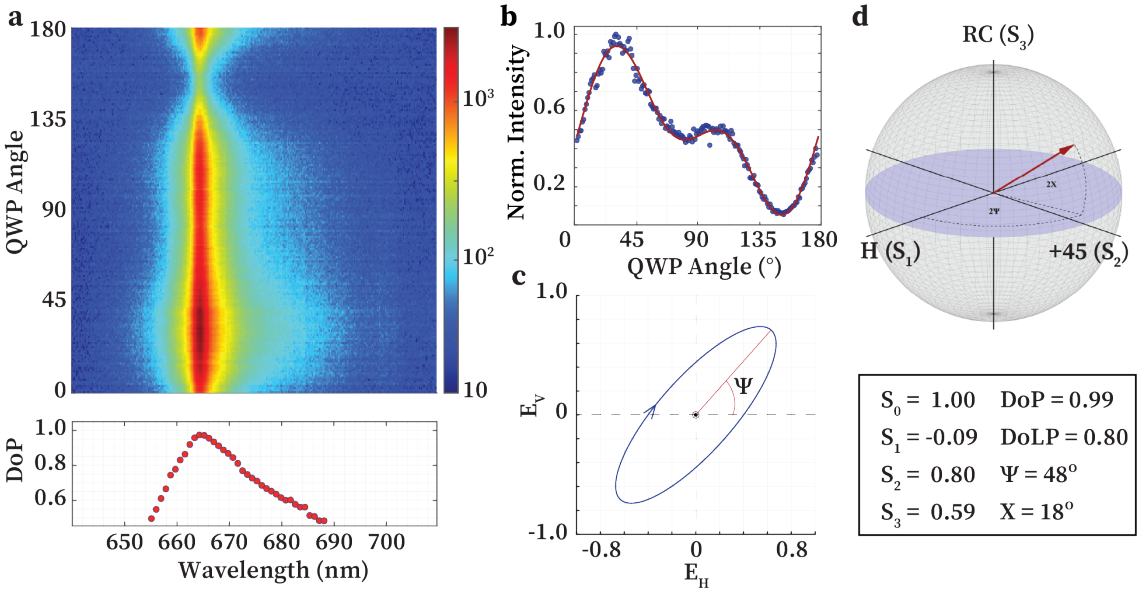

Figure 4.9: Full polarization state characterization of ZPL emission from Emitter-1 using the RQWP method. **(a)** Polarization map of the emitter's photoluminescence, obtained using the RQWP method. The plot at the bottom shows the spectrally resolved DoP of the emission, which reaches a maximum of 99% at the center of the ZPL. **(b)** The integrated ZPL intensity plotted as a function of the QWP rotation angle. The red solid curve is the theoretical fit to the data used to extract the Stokes parameters. **(c)** The polarization ellipse of the ZPL, with Ψ representing the orientation of the major axis relative to the horizontal. The arrow indicates the direction of rotation, corresponding to the detected circular polarization component. **(d)** The complete polarization state visualized as a vector on the Poincare sphere. The box at the bottom lists the extracted Stokes parameters and the corresponding calculated values for the DoP, DoLP, and the ellipse parameters (Ψ and χ).

The integrated ZPL intensity as a function of QWP angle is shown in panel (b). A fit of the RQWP intensity model (Equation 4.6) to this data allows for the extraction of the full Stokes parameters. The complete polarization state is visualized as a polarization ellipse in panel (c) and as a vector on the Poincare sphere in panel (d). The analysis yields the Stokes parameters $S_1 = -0.09$, $S_2 = 0.80$, and $S_3 = 0.59$. The corresponding Degree of Polarization is DoP = 0.99, while the Degree of Linear Polarization is only DoLP = 0.80. This significant difference between DoP and DoLP reveals that the reduced linear polarization of Emitter-1 is not due to random depolarization but is a direct consequence of its emission having a large, static circular polarization component. The extracted orientation of $\Psi = 48°$ is also in excellent agreement with the value obtained from the independent linear analysis shown in Figure 4.8(b). These results demonstrate the power of Stokes analysis to distinguish between true depolarization and coherent elliptical polarization states, a task that is impossible with simpler linear projection measurements.

4.4.4. Time-Resolved Stokes Polarization Analysis of Emitter 2

In addition to the time-averaged results, a time-resolved Stokes analysis was conducted on a single hBN defect (Emitter-2) to probe the dynamics of its polarization. This technique involves recording PL decay curves at various QWP angles and extracting the Stokes parameters as a function of time post-excitation. Figure 4.10(a) displays the DoP and the corresponding Stokes parameters of the fully polarized emission component over a 5 ns time window. The DoP rises sharply from approximately 0.3 to 0.5 within the first nanosecond before stabilizing. This dynamic aligns with previous observations of defects in both hBN and diamond (*44*). During this initial transient period, the Stokes parameters S_2 and S_3 exhibit significant evolution, while S_1 remains relatively constant near zero.

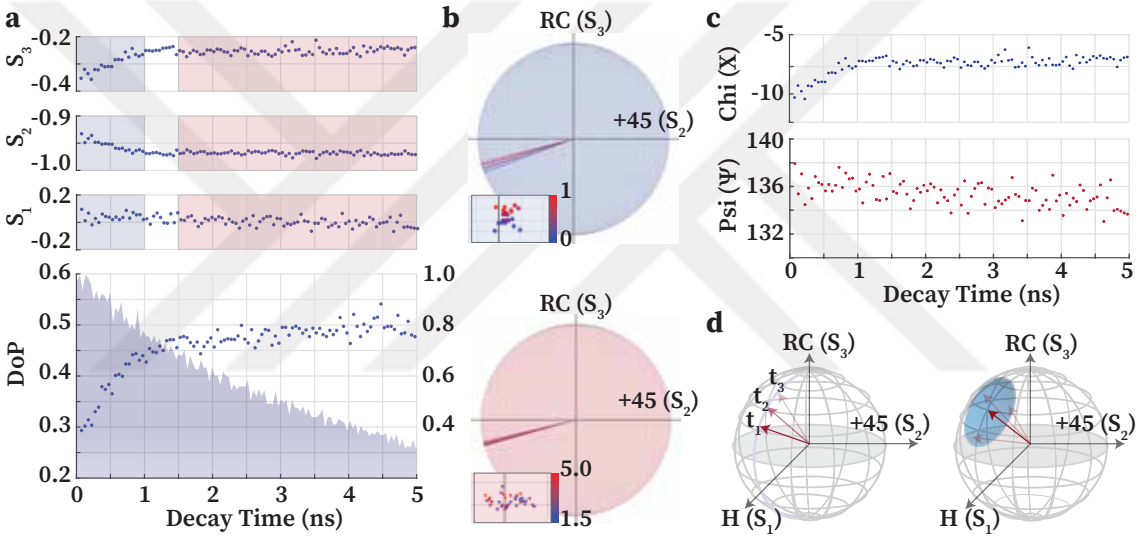

Figure 4.10: Time-resolved polarization dynamics of Emitter-2 and possible relaxation mechanisms of a single-photon emitter. **(a)** The time-resolved DoP and the individual Stokes parameters (S_1, S_2, S_3) of the completely polarized part of the emission, plotted against the decay time for the first 5 ns after excitation. The photoluminescence decay histogram from the TCSPC measurement is overlaid on the DoP plot. **(b)** The evolution of the polarization state visualized on the Poincare sphere for two distinct time windows: a dynamic region from 0-1 ns (blue) and a more stable region from 1.5-5.0 ns (red). The insets show the distribution of polarization states on the sphere's surface for each respective window. **(c)** The corresponding dynamical behavior of the polarization ellipse parameters, orientation (Ψ) and ellipticity (χ), as a function of decay time. **(d)** A schematic illustrating two potential mechanisms responsible for the observed DoP behavior: a directional relaxation process (left) and a persistent, random fluctuation of the polarization state (right).

Figure 4.10(b) visualizes the evolution of the polarization state on the Poincare sphere for an early, dynamic time window (0-1 ns, blue) and a later, more stable window (1.5-5.0 ns, red). During the first nanosecond, the polarization state evolves toward the linear polarization plane, evidenced by the decrease in the circular component (S_3) and the evolution of the linear component (S_2). The corresponding changes in the polarization

ellipse parameters-orientation (Ψ) and ellipticity (χ)-are shown in Figure 4.10(c).

Based on these observations, two underlying mechanisms can be identified, as illustrated in Figure 4.10(d). The directional evolution during the early decay times suggests a deterministic relaxation process. In contrast, the persistent fluctuations observed throughout the emission period point to a stochastic process, which may arise from environmental factors such as surface charge fluctuations or spectral diffusion (*32*).

The initial increase in DoP likely reflects an evolution from a partially mixed polarization state toward more coherent emission. This can be attributed to the relaxation of the emitter from a superposition of excited states into a lower-energy excited state that possesses a better-defined dipole moment. However, the saturation of the DoP at a value of 0.5, rather than approaching unity, indicates the presence of a persistent depolarization mechanism. Possible causes include fast spectral diffusion, phonon-assisted transitions, or emission from unresolved fine-structure levels. These findings underscore the power of time-resolved Stokes polarimetry, as it provides a comprehensive view of the emission polarization that allows for the direct observation of intrinsic dynamics that are averaged out in conventional measurements.

Chapter Summary

In this chapter, we conducted a comprehensive investigation into the polarization dynamics of single-photon emitters in hexagonal boron nitride. The initial study, using time-resolved linear polarimetry, revealed that the DoLP of these emitters is not static but changes dynamically in the first few nanoseconds following pulsed excitation. This observation highlighted a fundamental ambiguity: a reduced DoLP could stem from either a genuine random depolarization process or a coherent, non-linear (i.e., elliptical) polarization state. To resolve this, we employed the RQWP method to perform a complete Stokes analysis. The time-averaged Stokes measurements on a representative emitter (Emitter-1) conclusively demonstrated that its DoLP of 0.80 was significantly lower than its true DoP of 0.99. This proved that the apparent depolarization in a linear basis was, in fact, due to a significant, static circular polarization component in the emission.

Building on this finding, we performed the first time-resolved Stokes analysis on an hBN emitter (Emitter-2) to explore its polarization evolution with even greater detail. This advanced measurement revealed a deeper layer of dynamics, showing that the true DoP is not constant but increases rapidly from approximately 0.3 to 0.5 within the first nanosecond of decay before stabilizing. This behavior was attributed to the interplay of two distinct mechanisms: an initial, rapid relaxation process in which the emitter set-

tles into a more coherent state, and a persistent, underlying depolarization process likely linked to environmental noise or unresolved fine structure. These results underscore the necessity of complete Stokes polarimetry to accurately characterize the complex physics of solid-state quantum emitters and engineer their properties for future quantum applications.

CHAPTER 5

QUANTUM KEY DISTRIBUTION WITH DEFECTS IN HBN

In this chapter, we present a landmark demonstration: the first integration of a 2D material-based single-photon emitter into a QKD system. Specifically, we detail the first use of a hBN defect as the quantum light source for a proof-of-concept QKD application (*4*). We begin by establishing the theoretical foundations of QKD, detailing the principles that ensure quantum-secure communication and providing an overview of foundational protocols. This includes a detailed explanation of the BB84 (*81*) and B92 (*82*) protocols, which are most relevant to this work. Subsequently, we describe the preparation of the hBN sample and present a rigorous optical characterization of a single, isolated defect, confirming its properties as a high-purity, room-temperature single-photon source through spectral, temporal, and photon correlation measurements. Following this, we detail the implementation of a proof-of-concept, free-space QKD system using the B92 protocol with the validated hBN emitter and analyze its performance, including the achieved sifted key rate and quantum bit error rate. The chapter concludes with a simulation of the secret key rate as a function of channel loss, providing a clear outlook on the potential of this platform and a roadmap for future system enhancements.

5.1. Introduction: The Principles of Quantum Secure Communication

The advent of quantum computing promises to revolutionize fields ranging from medicine to materials science. However, this computational power also poses a significant threat to the security of our current digital infrastructure. Much of modern cryptography, particularly public key systems like RSA and Elliptic Curve Cryptography, relies on the computational difficulty of specific mathematical problems, such as factoring large numbers or solving the discrete logarithm problem (*83*). A sufficiently powerful, fault-tolerant quantum computer, running algorithms like Shor's algorithm, would be able to solve these problems efficiently, rendering our current public key encryption methods obsolete (*70*).

5.1.1. The Post Quantum Cryptographic Imperative

This vulnerability creates an urgent need for new cryptographic methods that are secure against attacks from both classical and quantum computers. The threat is not a distant one; it is immediate due to the "store now, decrypt later" scenario (*84*). In this scenario, an adversary can intercept and store encrypted data today, waiting for the day when a quantum computer is available to decrypt it. This means that sensitive information with long-term value, such as government secrets, financial records, and intellectual property, is already at risk.

In response, the global cryptographic community is pursuing two primary avenues for quantum-safe security. The first is Post-Quantum Cryptography, which involves developing new public key algorithms based on mathematical problems believed to be intractable for both classical and quantum computers (*85*). The second, and the focus of this chapter, is Quantum Key Distribution. This radically different approach does not rely on computational assumptions; instead, it grounds its security in the fundamental laws of physics.

5.1.2. Fundamentals of Quantum Key Distribution

Quantum Key Distribution is a secure communication method that enables two parties, conventionally referred to as Alice (the sender) and Bob (the receiver), to produce and share a random, secret key known only to them. This key can then be used with a symmetric encryption algorithm, ideally the one-time pad, which is provably secure when used with a truly random key to encrypt and decrypt a message transmitted over a standard communication channel.

The security of QKD is not derived from mathematical complexity but from the principles of quantum mechanics (*86*). It relies on encoding key information onto individual quantum states, or qubits, which are typically realized using the polarization states of single photons (*87*). The following quantum principles guarantee the security:

- **The Observer Effect**: A fundamental consequence of quantum indeterminacy is that the act of measuring an unknown quantum system inevitably disturbs it (*88*). If a third party, an eavesdropper named Eve, attempts to intercept and measure the photons Alice sends to Bob, her measurement will alter the quantum states of those photons. This introduces detectable anomalies in the communication, allowing Al-

ice and Bob to quantify the extent of the eavesdropping and abort the protocol if the security is compromised.

- **The No Cloning Theorem**: This theorem states that it is impossible to create an identical, independent copy of an arbitrary, unknown quantum state (*89*). This prevents Eve from simply intercepting a photon, copying its state perfectly, and sending the original on to Bob without leaving a trace. Any attempt to learn about the state requires a measurement, which brings the observer effect into play.

While the theoretical framework of QKD promises unconditional security based on these physical laws, the practical implementation of any QKD system presents significant challenges. Government security agencies, such as the U.S. National Security Agency and Germany's Federal Office for Information Security (BSI), have correctly pointed out that the actual security of a QKD system is highly dependent on its specific implementation (*90*, *91*). Real-world components are imperfect: single-photon sources may occasionally emit multiple photons, detectors have dark counts and finite efficiency, and optical components can have polarization-dependent losses. These imperfections can create side channels that a sophisticated eavesdropper might be able to exploit (*92*). Therefore, a critical distinction exists between the protocol's security, which is a theoretical abstraction, and the system's security, which is a property of its physical realization. The work presented in this chapter is a direct investigation of this relationship. The non-zero Quantum Bit Error Rate (QBER), the necessity of temporal filtering to combat detector noise, and the finite sifted key rate are not mere experimental limitations; they are the cryptographic consequences of the physical properties of the single photon source and the detection apparatus. This chapter, therefore, explores not just a QKD protocol, but the tangible performance of a QKD system where the material science of the hBN defect is inextricably linked to the cryptographic security and efficiency of the entire communication link.

5.2. Overview of Foundational QKD Protocols

The foundational protocols of quantum cryptography are often categorized as prepare-and-measure protocols, a family of schemes where one party (Alice) prepares single quantum states and sends them to a second party (Bob) for measurement. The security of these protocols relies on the fundamental principle that any attempt by an

eavesdropper to measure the quantum states will inevitably cause a disturbance that Alice and Bob can detect. The seminal examples of this approach are the BB84 protocol, where Alice prepares and sends single photons in states randomly chosen from two mutually unbiased bases, and the B92 protocol, which uses just two non-orthogonal states. Given their direct relevance to the experimental work presented in this thesis, we will now examine the BB84 and B92 protocols in greater detail.

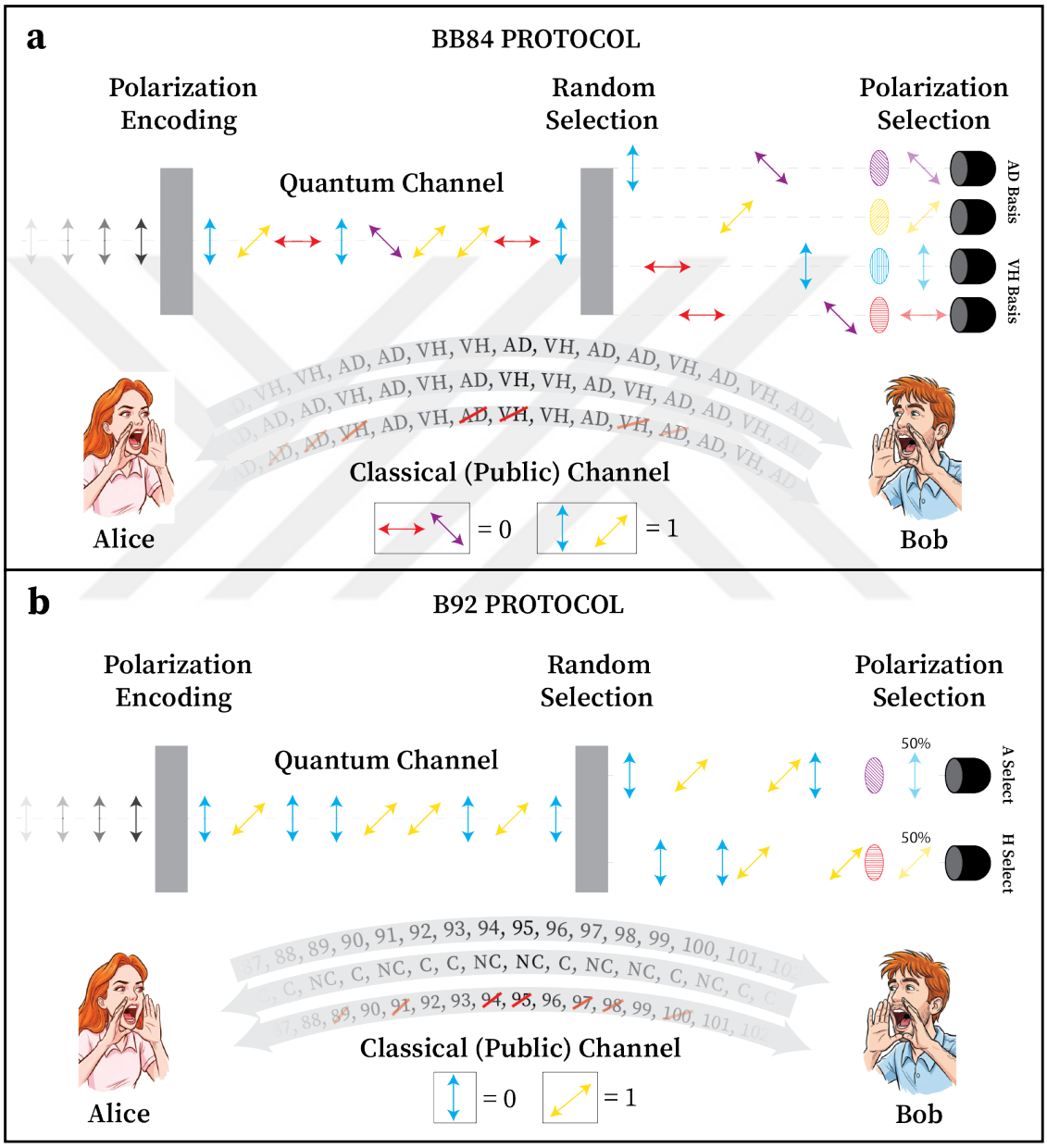

Figure 5.1: Comparison of **(a)** BB84 and **(b)** B92 Quantum Key Distribution protocols. The detailed explanation of the protocols can be found in the main text.

5.2.1. The BB84 Protocol

The first and most well-known QKD protocol is the BB84 protocol, proposed by Charles Bennett and Gilles Brassard in 1984 (*81*). It serves as the foundation for much of the field, and its security has been rigorously studied. The protocol (See Figure 5.1 **a**) proceeds as follows:

1. **Preparation (Alice)**: Alice generates two independent strings of random bits. The first string will become the raw key material. The second string determines the polarization basis she will use to encode each bit of the first string. She uses two mutually unbiased bases: the rectilinear basis, consisting of horizontal ($|H\rangle$, 0°) and vertical ($|V\rangle$, 90°) polarizations, and the diagonal basis, consisting of diagonal ($|D\rangle$, +45°) and anti-diagonal ($|A\rangle$, 135°) polarizations. For example, she might assign $|H\rangle$ and $|D\rangle$ to represent a '0' bit, and $|V\rangle$ and $|A\rangle$ to represent a '1' bit. For each bit in her key string, she prepares a single photon in the corresponding polarization state, chosen from the basis dictated by her random basis string.

2. **Transmission**: Alice sends the sequence of prepared single photons to Bob over a quantum channel, which could be an optical fiber or a free space link.

3. **Measurement (Bob)**: For each photon he receives, Bob also randomly and independently chooses a measurement basis (rectilinear or diagonal). He measures the photon's polarization in his chosen basis and records the outcome. If Bob decides on the same basis as Alice, he should measure the same bit value as Alice, and thus he can correctly infer the bit that Alice intended to send. If he chose the wrong basis, his result, and thus the bit he reads, will be random.

4. **Sifting (Public Discussion)**: After the quantum transmission is complete, Alice and Bob communicate over a public but authenticated classical channel. They publicly announce the sequence of bases they used for each photon, but not their key bits. They compare their basis choices and discard all measurement results where they used different bases. On average, this step, known as sifting, removes half of the raw data. The remaining correlated bits form the "sifted key".

5. **Error Estimation**: Alice and Bob then sacrifice a random subset of their sifted key bits by publicly comparing them. The discrepancy between their values is referred to as the Quantum Bit Error Rate. If the QBER is below a predefined security threshold (25% for generic Intercept-Resend Attack (*93*), between 11% - 28% for

more complex attacks and/or with additional security measures (*94*, *95*)), they can proceed. A high QBER indicates the likely presence of an eavesdropper, and the protocol must be aborted.

6. **Post Processing**: If the QBER is acceptably low, Alice and Bob apply two classical algorithms to the remaining sifted key. First, error correction is used to identify and remove any discrepancies in their key strings. Second, privacy amplification is performed, a process where they distill a shorter, but provably secret, final key by applying a hash function. This step effectively removes any partial information that Eve might have gained.

5.2.2. The B92 Protocol

In 1992, Charles Bennett proposed a simplified version of BB84, now known as the B92 protocol (*82*). Its main innovation is the use of only two non-orthogonal quantum states instead of the four states used in BB84. This simplification streamlines the protocol, particularly the classical communication phase, although at the cost of a lower key rate (*96*). The protocol (See Figure 5.1 **b**) proceeds as follows:

1. **Preparation (Alice)**: Alice's bit value directly determines which of two non-orthogonal states she prepares. For instance, in an implementation like the one described in this chapter, a '0' bit is encoded with a vertical polarization ($|V\rangle$, 90°) and a '1' bit is encoded with a diagonal polarization ($|D\rangle$, +45°).

2. **Transmission**: Alice sends the sequence of prepared photons to Bob over the quantum channel.

3. **Measurement (Bob)**: For each incoming photon, Bob randomly chooses between two polarizations, each orthogonal to one of Alice's prepared states. For example, he can choose to select anti-diagonal ($|A\rangle$) and horizontal ($|H\rangle$) polarization states.

4. **Sifting (Public Discussion)**: The sifting process is fundamentally different from BB84. A conclusive result is kept for the key only when Bob's measurement unambiguously reveals the bit Alice sent. This occurs in the following cases:

    - If Bob detects a horizontal ($|H\rangle$) photon, he knows with certainty that Alice must have sent $|D\rangle$, so he records a '1'.

- If Bob detects an anti-diagonal ($|A\rangle$) photon, he knows with certainty that Alice must have sent $|V\rangle$, so he records a '0'.

All other polarization states are ambiguous and must be discarded. Bob then publicly announces only the time slots in which he made a conclusive detection (C, meaning clicked). Alice compares this list to her original sequence and discards the time slots where Bob had no detection (NC, meaning not clicked). The remaining time slots (corresponding to bits) form the sifted key. This process has a theoretical success probability of 25% per photon sent due to random selections on Bob's side.

Table 5.1: Comparison of the BB84 and B92 Quantum Key Distribution protocols.

Feature	BB84 Protocol	B92 Protocol
States Used by Alice	Four states from two mutually unbiased bases (e.g., $\|H\rangle, \|V\rangle, \|+45°\rangle, \|-45°\rangle$)	Two non-orthogonal states (e.g., $\|V\rangle, \|+45°\rangle$)
Basis Choices by Alice	Randomly chooses between two bases (e.g., rectilinear or diagonal) for each bit.	The bit value itself determines the state; no separate basis choice is needed.
Basis Choices by Bob	Randomly chooses between the same two bases as Alice for each measurement.	Randomly chooses between two specific measurement bases designed to identify one of Alice's states.
Sifting Process	Alice and Bob publicly announce their basis choices and discard all events where the bases do not match.	Bob only announces the time slots of conclusive detections. No basis announcement is required.
Theoretical Efficiency (Ideal)	50% of transmitted photons contribute to the sifted key.	25% of transmitted photons contribute to the sifted key.
Core Security Principle	No-cloning theorem and disturbance upon measurement of non-orthogonal states (*87*).	Disturbance upon measurement of non-orthogonal states (*97*).

The table 5.1 summarizes the key operational differences between the BB84 and B92 protocols, highlighting the distinctions in state preparation, sifting procedure, and theoretical key rate.

5.2.3. Entanglement-Based Protocols

While the prepare-and-measure schemes are more straightforward to implement, it is essential to acknowledge the other prominent family of QKD protocols: entanglement-based protocols. The E91 protocol, pioneered by Artur Ekert in 1991, operates on a different principle (*98*). Instead of Alice preparing states, a central source distributes pairs of entangled particles (e.g., photons) to Alice and Bob. They each measure their particle, randomly choosing from a set of bases. Security is guaranteed by testing a Bell-like inequality on a subset of their measurement results. A violation of this inequality confirms the presence of genuine quantum correlations, which cannot be mimicked by a classical eavesdropper, thus elegantly tying the security of QKD to the fundamental non-locality of quantum mechanics.

The conceptual link between these two approaches was solidified by the BBM92 protocol (*99*), which showed that an entanglement-based source could be used to implement the BB84 scheme. In this view, Alice can measure her particle from an entangled pair, and her random measurement choice and its outcome effectively "prepare" the state of Bob's particle in one of the BB84 states. This equivalence not only unified the understanding of different QKD schemes but also provided new insights into their security proofs.

5.3. B92 Protocol QKD with an hBN-based Single Photon Source

This section describes the full experimental realization of a QKD system utilizing a single-photon emitter based on a defect in hexagonal boron nitride. The following subsections detail the complete process, beginning with the material preparation, followed by a rigorous optical characterization to validate the emitter as a suitable quantum source, and culminating in the integration of the source into a QKD setup and the analysis of its performance.

5.3.1. Sample Preparation

The experimental work in this chapter transitions from the theoretical principles of QKD to a practical demonstration using a novel quantum light source. The source platform is hBN, a two-dimensional van der Waals material known for its wide bandgap and

ability to host optically active defects that can function as single-photon emitters at room temperature. The sample was prepared by obtaining multilayer hBN flakes from a commercial solution (Graphene Supermarket) and drop casting them onto a silicon substrate with a 285 nm layer of silicon dioxide (SiO_2/Si). This scalable and straightforward preparation method can yield numerous isolated defects suitable for study. All experimental data presented in this chapter were obtained from a single, isolated defect found within one of these flakes, operating entirely at room temperature.

5.3.2. Optical characterization of QKD candidate

Before a quantum emitter can be used in a QKD experiment, it must be rigorously characterized to ensure it meets the stringent requirements for such an application. The key criteria are that it must be a bright, stable, and pure single photon source with well-defined polarization properties.

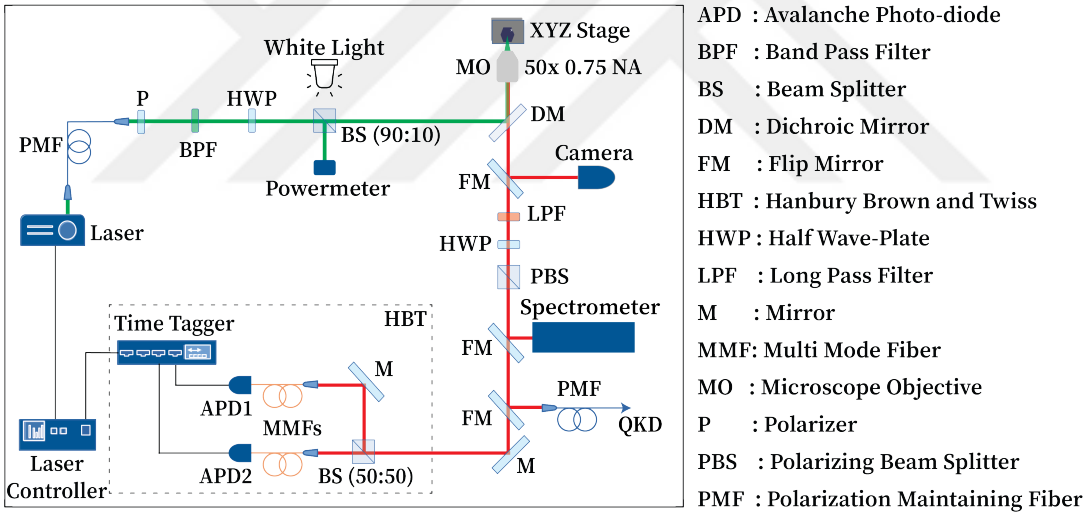

Figure 5.2: Schematic representation of the confocal micro-PL setup used to characterize the optical properties of single defects in hBN. A spectrometer spectrally analyzes collected emission, and its single-photon nature is measured with an HBT interferometer. Spectrally filtered and polarized single photon emission is guided to the QKD system via a polarization-maintaining single-mode fiber. Reprinted with permission from Samaner, C. et al. Adv. Quantum Technol. 2022, 5 (9), 2200059. Copyright 2022 Wiley-VCH GmbH.

The initial identification and subsequent optical characterization of the defect were performed using the custom-built confocal micro photoluminescence (μPL) setup depicted in Figure 5.2. A pulsed laser was used for excitation, focused onto the sample by a high-numerical-aperture microscope objective (NA = 0.75), which also collected the resulting photoluminescence. A dichroic mirror separated the excitation and emission

paths. The collected emission could be directed to a spectrometer for spectral analysis or to a Hanbury Brown and Twiss (HBT) interferometer for photon correlation measurements to verify its quantum nature. Once an emitter was fully characterized and deemed suitable, its emission was spectrally filtered and coupled into a polarization-maintaining single-mode fiber for delivery to the QKD system.

Spatial and Spectral Identification

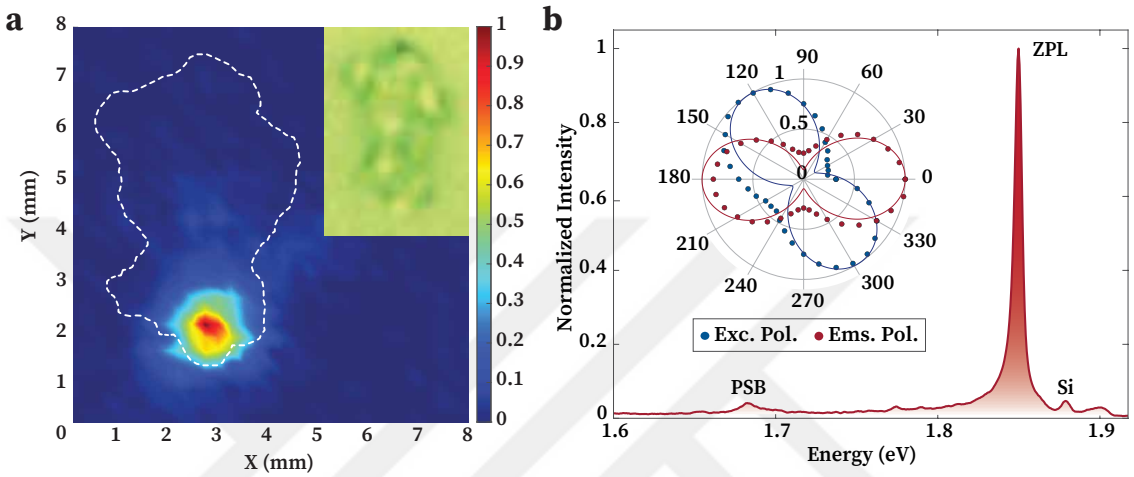

Figure 5.3: PL mapping, spectrum, and polarization response of a localized emitter in bulk hBN. **(a)** PL map of a bulk hBN with a bright localized emission. The inset shows the optical image of the studied hBN structure. **(b)** The PL spectrum of the isolated defect, taken at a 1 MHz repetition rate, shows the ZPL and PSB emission of the defect, as well as the Raman scattering from the silicon substrate. The inset shows the excitation (blue) and emission (red) polarization-dependent intensity of ZPL emission. Reprinted with permission from Samaner, C. et al. Adv. Quantum Technol. 2022, 5 (9), 2200059. Copyright 2022 Wiley-VCH GmbH.

The first step was to locate a suitable emitter. This was achieved by creating a photoluminescence map of the sample, as shown in Figure 5.3a. The map reveals a bright, spatially localized emission spot, indicating the presence of an isolated defect. The corresponding emission spectrum, recorded under a 1 MHz laser repetition rate, is shown in Figure 5.3b. The spectrum exhibits the characteristic features of a defect emitter in hexagonal boron nitride. A sharp and intense ZPL is observed at an energy of 1.848 eV (wavelength of 671 nm). This ZPL is accompanied by a broad PSB centered at approximately 1.683 eV. The energy difference between the ZPL and the PSB peak is ~165 meV, which corresponds well with the energy of the high-energy optical phonon mode in the hBN lattice (*80*). The fact that the ZPL emission strongly dominates the spectrum signifies a large Debye-Waller factor. This is highly desirable for practical applications, as it allows for efficient spectral filtering to isolate the ZPL photons, thereby maximizing the usable photon flux and rejecting background noise. The inset of Figure 5.3b shows the

polarization-dependent intensity of the ZPL emission. The emitter exhibits strong linear polarization for both excitation and emission, with a measured visibility of approximately 78% for emission. This pronounced polarized nature of the emission is a fundamental prerequisite for using the photon's polarization to encode quantum information.

Brightness and Emission Dynamics

A practical QKD source must be bright enough to support a reasonable key exchange rate. To quantify the brightness of the selected emitter, an excitation power-dependent saturation measurement was performed on the spectrally filtered ZPL emission. The result, obtained under a 40 MHz laser repetition rate, is shown in Figure 5.4a. The emission rate increases with excitation power before beginning to saturate, a hallmark of a single quantum emitter. The data was fit using a three-level model, which yielded a projected maximum emission rate (R_∞) of 495 kHz into the first collection optic. This confirms that the defect is a bright source capable of generating a high flux of single photons.

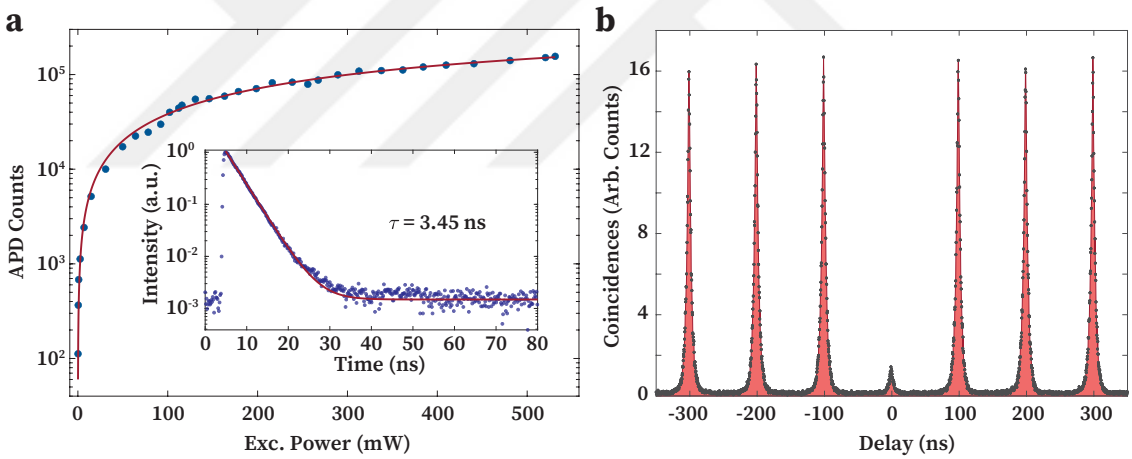

Figure 5.4: Excitation power dependence, lifetime, and photon correlation of a single emitter in bulk hBN. **(a)** Excitation power dependence of ZPL emission (spectrally filtered) measured with an APD under 40 MHz repetition rate. Inset: Time resolved PL of the defect with a decay time of 3.45 ns. **(b)** Second order photon correlation measurement of the same emitter taken under 1 MHz repetition rate. The anti-bunching value is estimated as $g^{(2)}(0) = 0.12 \pm 0.03$. Reprinted with permission from Samaner, C. et al. Adv. Quantum Technol. 2022, 5 (9), 2200059. Copyright 2022 Wiley-VCH GmbH.

The emission dynamics were studied using time-correlated single-photon counting (TCSPC). The inset of Figure 5.4a shows the photoluminescence decay trace, which is well described by a single exponential function. The fit reveals an excited state lifetime of $\tau = 3.45 \pm 0.05$ ns, a value typical for hBN emitters and sufficiently short to support high repetition rate operation.

Verification of Single Photon Emission

The most critical characteristic of a light source for QKD is its single-photon purity. The security of QKD protocols against sophisticated attacks, most notably the photon number splitting (PNS) attack, fundamentally relies on the promise that Alice sends one and only one photon at a time. In a PNS attack, if Alice emits a pulse containing multiple photons, Eve can intercept the pulse, "peel off" one photon to measure and gain information about the key, and forward the remaining photon(s) to Bob, all without introducing detectable errors. A trustworthy single-photon source renders this attack ineffective.

To verify the single-photon nature of the emitter, we measured its second-order autocorrelation function, $g^{(2)}(\tau)$, using an HBT setup. The result is shown in Figure 5.4b. The function exhibits a pronounced dip at zero time delay ($\tau = 0$), which is the definitive signature of photon antibunching. The value at the dip was calculated to be $g^{(2)}(0) = 0.12 \pm 0.03$. This value is significantly below the threshold of 0.5, which is the widely accepted criterion for classifying a source as a single photon emitter.

This measurement provides more than just a qualitative confirmation; it establishes a quantitative link between the material's purity and the system's cryptographic security. The $g^{(2)}(0)$ value is a direct measure of the probability of multi-photon emission. In a complete security analysis of a QKD system, the measured $g^{(2)}(0)$ is a critical input parameter. A lower value directly translates to less potential information leakage to Eve, which in turn allows for a higher secure key rate to be distilled during the privacy amplification stage. Therefore, the quality of the hBN crystal and the specific nature of the defect, which together determine the $g^{(2)}(0)$ value, are not merely material properties but are fundamental cryptographic parameters of the entire system.

5.3.3. Integration of Single Photon Source to QKD system

For this demonstration, the B92 protocol was chosen. While less efficient in terms of key rate than the BB84 protocol, its implementation is more straightforward, particularly regarding the receiver's design and classical post-processing, making it an ideal choice for a proof-of-concept experiment with the available equipment. The complete experimental setup is illustrated in Figure 5.5. The system is divided into the transmitter (Alice) and the receiver (Bob).

- **Alice (Transmitter)**: The heart of Alice's system is the characterized hBN single photon source. A pulse generator triggers the excitation laser at a clock rate

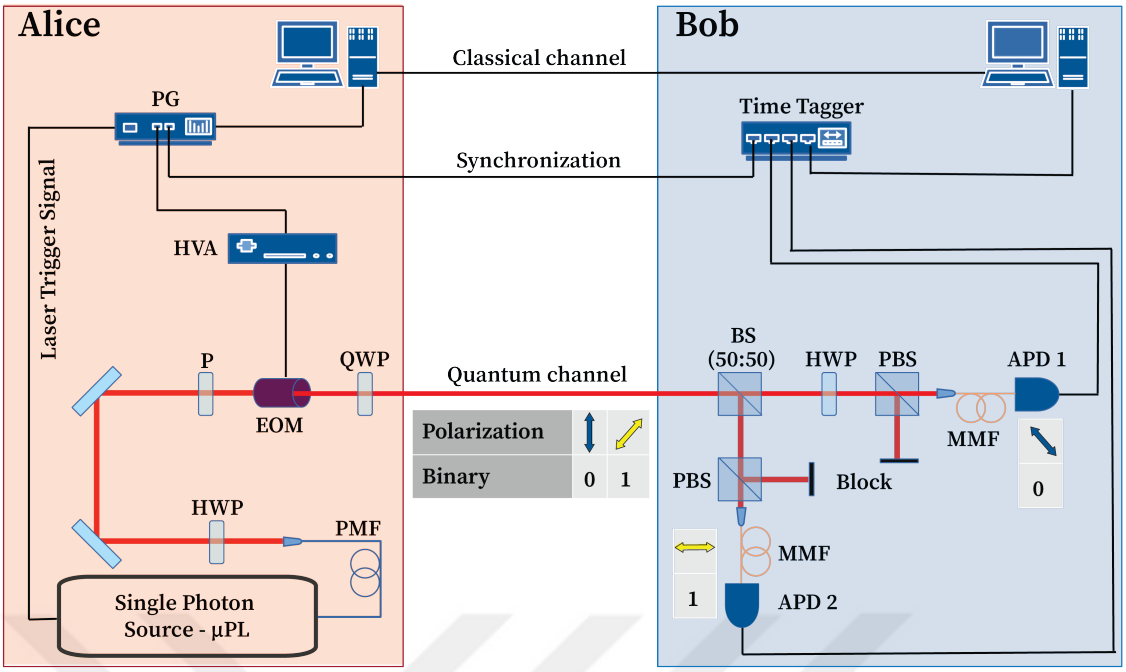

Figure 5.5: Experimental setup of the B92-based free space Quantum Key Distribution system. The Alice side features a single photon source, a pulse generator (PG), and an electro-optic modulator (EOM) for polarization encoding. A pulse generator is connected to the EOM via a high-voltage amplifier (HVA) to generate the high-voltage values necessary for altering the polarization of single photons by the EOM. The Bob side comprises a beam splitter (BS), two polarizing beam splitters (PBS), a half-wave plate (HWP) in one path, and two single photon detectors (APD1, APD2) for polarization analysis and photon detection. APDs and the Pulse Generator (PG) are connected to a time tagger unit for synchronization of Alice and Bob. Reprinted with permission from Samaner, C. et al. Adv. Quantum Technol. 2022, 5 (9), 2200059. Copyright 2022 Wiley-VCH GmbH.

of 1 MHz. The same PG sends a periodic binary signal to a high-voltage amplifier, which drives an electro-optic modulator (EOM). The single photons from the hBN defect are first passed through a polarizer to ensure a high extinction vertically polarized state before entering the EOM. The EOM, along with a subsequent quarter-wave plate (QWP), encodes the bit value onto the photon's polarization. A voltage of 0 V from the HVA results in a vertically polarized photon (bit '0'), while a voltage of 95 V results in a +45Â° polarized photon (bit '1'), thus preparing the two non-orthogonal states required for the B92 protocol. The encoded single photons are then sent to Bob through a free-space quantum channel.

- **Bob (Receiver)**: Bob's task is to measure the incoming photons in one of two randomly chosen bases. This random choice is implemented passively using a non-polarizing 50:50 beam splitter (BS), which directs each photon to one of two measurement arms. Each arm contains a polarizing beam splitter (PBS) set to analyze a specific basis. One arm measures in the diagonal basis to identify the 45Â° state

(conclusively identifying Alice's bit '0'), while the other arm, equipped with a half wave plate (HWP) to rotate the basis, measures in the rectilinear basis to identify the horizontal state (conclusively identifying Alice's bit '1'). Each measurement path terminates in a single photon avalanche diode. A time tagger unit records the detection events from both APDs and uses the synchronization signal from Alice's PG to correlate the events and build the key.

5.3.4. Error and Performance Analysis

The QKD demonstration was performed for a duration of 2.5 seconds with the system operating at a 1 MHz repetition rate. The excitation power was set to the maximum available, which corresponded to approximately half the saturation power of the emitter. The count rate after the microscope objective was 30 kHz, which was reduced to 7.8 kHz at the input of Alice's EOM due to coupling losses. After traversing the entire QKD system, including all optical components and accounting for detector efficiencies and the 25% intrinsic efficiency of the protocol, the final average count rate at each of Bob's detectors was approximately 400 Hz, in addition to detector dark counts of 1.5 kHz.

Figures 5.6a and 5.6b show histograms of the time difference between Alice's laser trigger and Bob's photon detection events. The peak in the distribution occurs at a delay of approximately 148 ns, a latency primarily due to the system's electronics. The temporal spread of this peak is a combination of the emitter's 3.45 ns lifetime and the timing jitter of the detectors.

A crucial technique in practical QKD is temporal filtering. By only accepting detection events that fall within a narrow time window (Δt) around the expected arrival time, one can significantly improve the signal-to-noise ratio by rejecting a significant fraction of uncorrelated detector dark counts. However, this creates a trade-off: a narrower window improves the QBER but reduces the number of accepted bits, thus lowering the sifted key rate (SKR). This relationship is explicitly shown in Figure 5.6c. As the temporal filter window is tightened from 9 ns to 3 ns, the QBER improves from 11.34% to 8.95%, but the SKR decreases from 414 bps to 238 bps. For this demonstration, a 3 ns window provides a good balance, yielding a secure key with a QBER well below the insecure limit. The key experimental parameters and results are summarized in Table 5.2.

These results, particularly a sifted key rate of 238 bps with a QBER of 8.95% under a 3 ns temporal filter, represent the first successful QKD demonstration using a

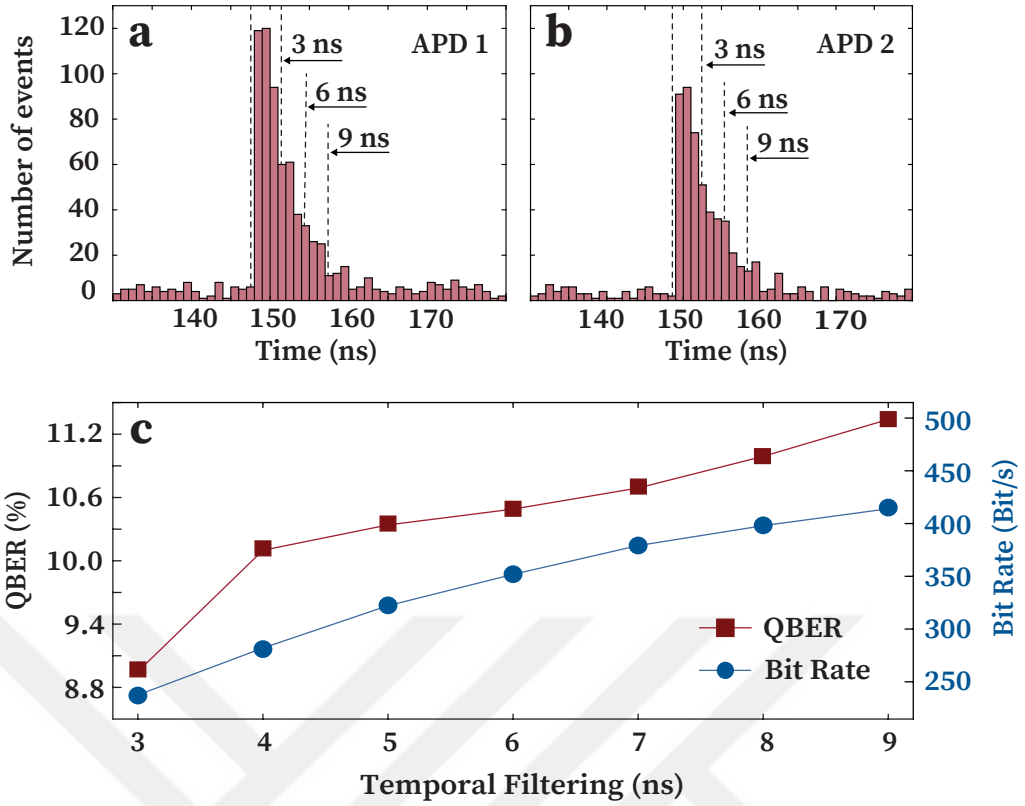

Figure 5.6: APD signal arrival histograms and QBER/bit rate performance in a QKD demonstration. **(a,b)** Histograms of relative time differences between laser trigger and detection on APDs, showing total counts in 1 ns time intervals over 2.5 seconds of QKD demonstration. **(c)** Change of Quantum Bit Error Rate and bit rate as a function of temporal filtering. Reprinted with permission from Samaner, C. et al. Adv. Quantum Technol. 2022, 5 (9), 2200059. Copyright 2022 Wiley-VCH GmbH.

defect in hexagonal boron nitride. To place this achievement in the broader context of the field, it is instructive to compare its performance with that of other prominent single-photon source platforms, as detailed in Table 5.3. A close examination reveals several key insights. Our demonstrated QBER of 8.9-11.3% is within the range of other solid-state systems, such as the quantum dot demonstration in Ref. [105], which reported a QBER of 6.0-9.0%. The corresponding normalized secure key rate (SKR/Freq.) of our system, (238-414) $\times 10^{-6}$, is notably higher than the 33.6 $\times 10^{-6}$ achieved in that work, highlighting the high photon flux of our hBN emitter. While more mature platforms, such as NV centers [108] or specific QD systems [104, 106], exhibit lower QBERs and, in some cases, higher key rates, it is crucial to recognize that these represent technologies that have been developed over a significantly more extended period. Our results, achieved in a proof-of-concept setup, are therefore highly encouraging. The performance metrics are not limited by the hBN emitter's intrinsic properties alone but are also influenced by factors discussed previously, such as significant detector dark counts and suboptimal

Table 5.2: Summary of QKD experimental parameters and results under 1 MHz operation.

Temporal Filtering (Δt)	Mean Photon Number (μ)	Purity ($g^{(2)}(0)$)	Sifted Key Rate (bps)	QBER (%)
3 ns	0.0117	0.046	238	8.95
9 ns	0.0234	0.080	414	11.34

optical coupling efficiency.

Table 5.3: Comparison of QKD demonstrations using color centers in hBN and other single photon sources. (SKR: Secure Key Rate). Used with permission of Wiley-VCH GmbH, from (*100*); permission conveyed through Copyright Clearance Center, Inc.

Source	Refs.	Protocol	Encoding	λ (nm)	Photon per pulse	QBER (%)	SKR/Freq. (Bits $\times 10^{-6}$)	Bound (dB)
hBN	(*101*)	BB84	Passive	728	—	—	—	26
	(*4*)	B92	Pol.	671	0.011-0.023	8.9-11.3	(238-414) $\times 10^{-6}$	22
	(*102*)	BB84	Pol.	645	0.012	3.0-8.0	(504-900) $\times 10^{-6}$	—
QDs	(*103*)	BB84	Pol.	877	0.007	2.5	329 $\times 10^{-6}$	28
	(*104*)	BB84	Pol.	910	0.0034	6.0-9.0	33.6 $\times 10^{-6}$	—
	(*23*)	BB84	Pha.	1580	0.05	2.3	70 $\times 10^{-6}$	23
NV Center	(*105*)	BB84	Pol.	637-750	0.014	4.6	1792 $\times 10^{-6}$	20
	(*106*)	BB84	Pol.	600-800	0.029	3.0	2600 $\times 10^{-6}$	16
TMDCs	(*107*)	BB84	Passive	807	0.013	0.8	—	23
Molecule	(*108*)	BB84	Passive	780-830	0.04-0.08	2.0-3.9	—	23-27

Comparison of hBN defects with other SPSs validates that hBN defects are a viable and immediately competitive platform for QKD, establishing a solid performance baseline. It also illuminates the path forward. The superior performance of more established systems demonstrates the potential gains that can be realized by addressing the specific engineering and system-level bottlenecks identified in our setup. This naturally leads to the question of how much performance can be improved with practical enhancements. To provide a quantitative answer and to chart a course for future work, we now turn to a simulation of the secret key rate under optimized conditions.

Secret Key Rate Simulation and Outlook

To evaluate the potential of this hBN-based platform and to benchmark it against other QKD systems, we performed a simulation of the secret key rate as a function of channel loss. The simulation employs a standard model for the BB84 protocol (for ease of comparison with the literature) and utilizes the experimentally measured parameters of our source as inputs (*109*). The secret key rate per pulse, R, is given by:

$$R = \frac{1}{2} P_{\text{click}} [1 - H_2(\text{QBER}_p) - f_{\text{EC}} H_2(\text{QBER}_\mu)]$$

where P_{click} is the overall detection probability at Bob, H_2 is the binary Shannon entropy function, QBER_p and QBER_μ are the phase and bit error rates respectively, and f_{EC} is the efficiency of the error correction protocol. The QBER and detection probabilities are functions of the mean photon number per pulse (μ), the source purity ($g^{(2)}(0)$), detector dark counts, and total channel loss.

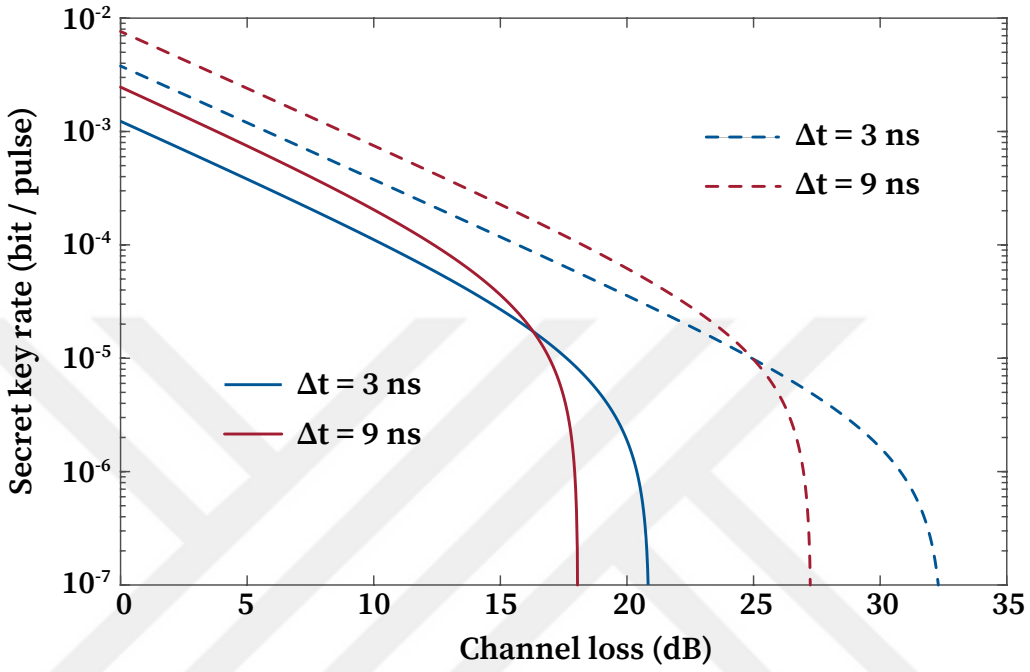

Figure 5.7: Simulated secret key rate versus channel loss for Δt = 3 ns and Δt = 9 ns temporal filtering settings. Solid lines represent simulations using experimentally measured values, while dashed lines represent an optimized experimental setup with improved optical transmission and reduced dark counts in APDs. Reprinted with permission from Samaner, C. et al. Adv. Quantum Technol. 2022, 5 (9), 2200059. Copyright 2022 Wiley-VCH GmbH.

The results of this simulation are shown in Figure 5.7. The solid lines represent the performance of the current experimental setup for the two temporal filtering conditions (Δt=3 ns and Δt=9 ns). The simulation confirms that a tighter temporal filter (3 ns) provides a more robust key over longer distances (higher channel loss) due to its lower QBER, despite having a lower initial key rate (*110*). More importantly, this analysis provides a clear roadmap for future improvements. The dashed lines in Figure 5.7 show the projected performance for an optimized system. This projection assumes concrete, achievable engineering improvements, including replacing the coupling fibers to enhance optical transmission and utilizing commercially available detectors with significantly lower dark counts (e.g., 25 Hz vs. 1.5 kHz). The simulation shows that these practical enhancements could boost the secret key rate by nearly an order of magnitude and significantly extend the achievable communication distance.

This analysis bridges the gap between a proof-of-concept experiment and a practical application. While the current key rate of 238 bps is modest, the simulation provides a data-driven argument for the platform's viability. It quantitatively demonstrates how much performance can be gained by tackling specific, identified engineering bottlenecks. Ultimately, the performance ceiling is set by the intrinsic properties of the quantum emitter itself; its quantum efficiency and saturation rate determine the maximum possible photon flux. Therefore, the path toward high-speed, long-distance QKD with hBN defects involves a two-pronged approach: fundamental materials science to discover and engineer even brighter and purer emitters, and parallel advances in quantum engineering to optimize the collection, transmission, and detection of the single photons they produce.

Chapter Summary

This chapter presents a comprehensive investigation into the use of single-photon emitters in hexagonal boron nitride for quantum key distribution. It began by establishing the theoretical foundations of QKD, detailing the principles of the BB84 and B92 protocols, and highlighting the physical laws that guarantee their security. The core of the chapter was the presentation of a successful proof-of-concept demonstration of a free-space QKD system operating at room temperature, utilizing a single, isolated defect in hBN as the quantum light source. This work represents a significant milestone, marking the first time a 2D material-based quantum emitter, specifically an hBN defect, has been successfully integrated into a functional QKD system. The work detailed the essential steps of selecting and characterizing a suitable emitter, verifying its high single-photon purity with a measured $g^{(2)}(0) = 0.12 \pm 0.03$, a critical requirement for security against photon-number-splitting attacks. The implementation of a B92 protocol was described, achieving a sifted key rate of 238 bps with a quantum bit error rate of 8.95%. The critical role of practical techniques, such as temporal filtering, in optimizing the trade-off between key rate and error rate was analyzed. Finally, through security rate simulations, a clear and quantitative pathway for future performance enhancements was established. By improving optical efficiencies and detector technologies, the secret key rate and communication distance of such a system can be substantially increased. This work firmly establishes that defects in hBN are a viable and promising platform for developing scalable, robust, and practical QKD systems, paving the way for future advancements in secure quantum communications.

CHAPTER 6

CONCLUSION AND OUTLOOK

This thesis has presented a comprehensive investigation into the optical and quantum properties of single-photon emitters in hBN, culminating in a landmark demonstration of their integration into a QKD system. Our work systematically advanced the understanding of these emitters, from their fundamental polarization behavior to their application in secure quantum communications. This final chapter summarizes the key findings from the three main studies of this research, draws overall conclusions, and provides an outlook on potential future investigations that build upon the results presented herein.

6.1. Summary of Key Findings

Our research was structured around three interconnected studies, each building upon the previous one to provide a comprehensive picture of the potential of hBN defects as robust quantum light sources for future quantum technologies.

6.1.1. Polarization Dynamics in a Linear Basis

The initial phase of our research focused on characterizing the fundamental emission properties of individual defects in hBN and NV centers in diamond by analyzing their time-resolved linear polarization dynamics. By creating detailed polarization-decay maps, we discovered that the DoLP is not static but evolves significantly over the nanosecond lifetime of the emitters. A key finding was the drastic improvement in linear visibility for photons emitted in the first few nanoseconds of the decay process, increasing from approximately 50% to nearly 70% in some emitters. While our drop-cast hBN emitters showed stable dipole orientations, some irradiated samples and NV centers exhibited a concurrent change in their emission axis in this early time window. This discovery highlights that time-averaged polarization measurements, which are commonly used in the literature, can obscure the true polarization quality of an emitter, and that the most highly polarized photons are emitted at the beginning of the decay process. This has profound

implications for optimizing polarization-based quantum protocols.

6.1.2. Complete Polarization Dynamics with Stokes Parameters

Recognizing that a simple linear basis analysis cannot distinguish between true depolarization and static circular polarization components, our second study employed a more sophisticated approach. We implemented the RQWP method to perform a complete time-averaged and time-resolved Stokes polarization analysis. The time-averaged measurements revealed a crucial insight: for a representative emitter, the DoP was exceptionally high at 99%. In contrast, the DoLP was only 80%. This unambiguously demonstrates that the reduced linear visibility was not primarily due to random depolarization but rather to a significant and stable circular polarization component in the emission.

The time-resolved analysis further illuminated these dynamics. We observed that the DoP itself exhibits a distinct rise within the first nanosecond, confirming our earlier findings. Furthermore, the evolution of the individual Stokes parameters (S_1, S_2, S_3) revealed that the polarization state follows a distinct trajectory on the Poincare sphere during the emission process, starting with a larger circular component that diminishes over time. These results provide a comprehensive and nuanced picture of the emission process, suggesting that the polarization state is not fixed but evolves dynamically, a critical consideration for the precise manipulation of polarization-encoded qubits.

6.1.3. Quantum Key Distribution with an hBN Emitter

The culmination of this research was the successful integration of a fully characterized, room-temperature hBN single-photon emitter into a functional QKD system. This work constitutes the first demonstration of a QKD protocol using a 2D material-based single-photon source. We designed and built a free-space communication link and implemented the B92 prepare-and-measure protocol, using the strong linear polarization of the hBN defect to encode cryptographic bits.

The experiment was a definitive success, resulting in the generation of a secure key with a sifted key rate of 238 bps and a QBER of 8.95%. This QBER is well below the security threshold for the protocol, confirming the system's viability for secure communication. We further analyzed the critical trade-off between the SKR and QBER by applying temporal filtering to the photon arrival times, demonstrating a key optimiza-

tion technique for practical QKD systems. The successful operation of this system, using a scalable and robust room-temperature emitter, represents a significant step toward the practical realization of quantum communication networks.

6.2. Overall Conclusion

In conclusion, this thesis presents a comprehensive and systematic investigation into the polarization properties of hBN quantum emitters, successfully translating these fundamental insights into a pioneering technological application. Our work has moved beyond static, time-averaged characterizations to reveal the rich, time-resolved polarization dynamics that define these sources. We have shown that while linear polarization can be imperfect, the true degree of polarization is often near unity, with the discrepancy arising from a dynamic interplay between linear and circular components.

By harnessing the most stable component of this emission, we achieved a landmark demonstration: the first quantum key distribution link secured by single photons from a 2D material. This result demonstrates that hBN emitters are not merely a subject of academic curiosity but a viable, robust, and scalable platform for building practical quantum technologies that can operate at room temperature. This research effectively bridges the gap between fundamental materials science and applied quantum information, establishing a solid foundation for utilizing 2D materials in the next generation of secure communication systems.

Future Outlook

The findings presented in this thesis lay the groundwork for several exciting future directions, spanning both fundamental emitter physics and applied quantum communication. A crucial next step in polarization dynamics research is to investigate the underlying physical mechanisms responsible for the time-dependent evolution of the polarization state, exploring the potential roles of spin dynamics, local charge fluctuations, and phonon interactions. A deeper understanding could enable the active engineering of defects (using techniques such as localized strain, electric fields, or coupling to photonic cavities) to produce single photons with tailored, stable polarization states on demand. Such high-quality flying qubits would, in turn, directly benefit the advancement of hBN-based QKD. Building upon the proof-of-concept system demonstrated here, future work should focus on dramatically increasing the secure key rate by integrating these optimized emitters into high-efficiency photonic structures such as solid immersion lenses or on-chip

waveguides. This would pave the way for implementing more robust decoy-state protocols, extending communication distances by developing telecom-wavelength emitters for integration with existing fiber networks, and ultimately, realizing entanglement-based QKD as a foundational step toward the development of quantum repeaters and the broader quantum internet.

REFERENCES

1. O'Brien, J. L. Optical Quantum Computing. *Science* **2007**, *318*, 1567–1570.

2. Vajner, D. A.; Rickert, L.; Gao, T.; Kaymazlar, K.; Heindel, T. Quantum Communication Using Semiconductor Quantum Dots. *Advanced Quantum Technologies* **2022**, *5*.

3. Degen, C. L.; Reinhard, F.; Cappellaro, P. Quantum Sensing. *Rev. Mod. Phys.* **2017**, *89*, 035002.

4. Samaner, C.; Pacal, S.; Mutlu, G.; Uyanik, K.; Ates, S. Free-Space Quantum Key Distribution with Single Photons from Defects in Hexagonal Boron Nitride. *Advanced Quantum Technologies* **2022**, *5*, 2200059.

5. Chen, X.; Greiner, J. N.; Wrachtrup, J.; Gerhardt, I. Single Photon Randomness Based on a Defect Center in Diamond. *Scientific Reports* **2019**, *9*.

6. Hoese, M.; Koch, M. K.; Breuning, F.; Lettner, N.; Fehler, K. G.; Kubanek, A. Single Photon Randomness Originating from the Symmetric Dipole Emission Pattern of Quantum Emitters. *Applied Physics Letters* **2022**, *120*.

7. Senellart, P.; Solomon, G.; White, A. High-Performance Semiconductor Quantum-Dot Single-Photon Sources. *Nature Nanotechnology* **2017**, *12*, 1026–1039.

8. Atatüre, M.; Englund, D.; Vamivakas, N.; Lee, S.-Y.; Wrachtrup, J. Material Platforms for Spin-Based Photonic Quantum Technologies. *Nat. Rev. Mater.* **2018**, *3*, 38–51.

9. Bradac, C.; Gao, W.; Forneris, J.; Trusheim, M. E.; Aharonovich, I. Quantum Nanophotonics with Group IV Defects in Diamond. *Nat. Commun.* **2019**, *10*, 5625.

10. Kianinia, M.; Xu, Z. Q.; Toth, M.; Aharonovich, I. Quantum Emitters in 2D Materials: Emitter Engineering, Photophysics, and Integration in Photonic Nanostructures. *Applied Physics Reviews* **2022**, *9*.

11. He, Y. M.; Clark, G.; Schaibley, J. R.; He, Y.; Chen, M. C.; Wei, Y. J.; Ding, X.;

Zhang, Q.; Yao, W.; Xu, X.; Lu, C. Y.; Pan, J. W. Single Quantum Emitters in Monolayer Semiconductors. *Nature Nanotechnology* **2015**, *10*, 497–502.

12. Tran, T. T.; Bray, K.; Ford, M. J.; Toth, M.; Aharonovich, I. Quantum Emission from Hexagonal Boron Nitride Monolayers. *Nature Nanotechnology* **2016**, *11*, 37–41.

13. Jungwirth, N. R.; Calderon, B.; Ji, Y.; Spencer, M. G.; Flatté, M. E.; Fuchs, G. D. Temperature Dependence of Wavelength Selectable Zero-Phonon Emission from Single Defects in Hexagonal Boron Nitride. *Nano Letters* **2016**, *16*, 6052–6057.

14. Tran, T. T.; Elbadawi, C.; Totonjian, D.; Lobo, C. J.; Grosso, G.; Moon, H.; Englund, D. R.; Ford, M. J.; Aharonovich, I.; Toth, M.; et al., Robust Multicolor Single Photon Emission from Point Defects in Hexagonal Boron Nitride. *ACS Nano* **2016**, *10*, 7331–7338.

15. Naclerio, A. E.; Kidambi, P. R. A Review of Scalable Hexagonal Boron Nitride (h-BN) Synthesis for Present and Future Applications. *Advanced Materials* **2023**, *35*.

16. Kianinia, M.; Regan, B.; Tawfik, S. A.; Tran, T. T.; Ford, M. J.; Aharonovich, I.; Toth, M. Robust Solid-State Quantum System Operating at 800 K. *ACS Photonics* **2017**, *4*, 768–773.

17. Aharonovich, I.; Englund, D.; Toth, M. Solid-State Single-Photon Emitters. *Nature Photonics* **2016**, *10*, 631–641.

18. Xu, X.; Martin, Z. O.; Sychev, D.; Lagutchev, A. S.; Chen, Y. P.; Taniguchi, T.; Watanabe, K.; Shalaev, V. M.; Boltasseva, A. Creating Quantum Emitters in Hexagonal Boron Nitride Deterministically on Chip-Compatible Substrates. *Nano Lett.* **2021**, *21*, 8182–8189.

19. Li, C.; Mendelson, N.; Ritika, R.; Chen, Y.; Xu, Z.-Q.; Toth, M.; Aharonovich, I. Scalable and Deterministic Fabrication of Quantum Emitter Arrays from Hexagonal Boron Nitride. *Nano Lett.* **2021**, *21*, 3626–3632, PMID: 33870699.

20. Mendelson, N. et al. Identifying Carbon as the Source of Visible Single-Photon Emission from Hexagonal Boron Nitride. *Nature Materials* **2021**, *20*, 321–328.

21. Gottscholl, A.; Diez, M.; Soltamov, V.; Kasper, C.; Sperlich, A.; Kianinia, M.; Bradac, C.; Aharonovich, I.; Dyakonov, V. Room Temperature Coherent Control of Spin Defects in hexagonal Boron Nitride. **2020**,

22. Chejanovsky, N.; Rezai, M.; Paolucci, F.; Kim, Y.; Rendler, T.; Rouabeh, W.; Fávaro de Oliveira, F.; Herlinger, P.; Denisenko, A.; Yang, S.; Gerhardt, I.; Finkler, A.; Smet, J. H.; Wrachtrup, J. Structural Attributes and Photodynamics of Visible Spectrum Quantum Emitters in Hexagonal Boron Nitride. *Nano Lett.* **2016**, *16*, 7037–7045.

23. Takemoto, K.; Nambu, Y.; Miyazawa, T.; Sakuma, Y.; Yamamoto, T.; Yorozu, S.; Arakawa, Y. Quantum Key Distribution over 120km Using Ultrahigh Purity Single-Photon Source and Superconducting Single-Photon Detectors. *Scientific Reports* **2015**, *5*, 4–6.

24. Ding, X.; He, Y.; Duan, Z. C.; Gregersen, N.; Chen, M. C.; Unsleber, S.; Maier, S.; Schneider, C.; Kamp, M.; Hofling, S.; Lu, C. Y.; Pan, J. W. On-Demand Single Photons with High Extraction Efficiency and Near-Unity Indistinguishability from a Resonantly Driven Quantum Dot in a Micropillar. *Physical Review Letters* **2016**, *116*, 1–6.

25. Kretzschmar, T.; Ritter, S.; Kumar, A.; Vogl, T.; Eilenberger, F.; Schmidt, F. Quantitative Investigation of Quantum Emitter Yield in Drop-Casted Hexagonal Boron Nitride Nanoflakes. *ACS Applied Optical Materials* **2024**, *2*, 1427–1435.

26. Patel, R. N.; Hopper, D. A.; Gusdorff, J. A.; Turiansky, M. E.; Huang, T. Y.; Fishman, R. E.; Porat, B.; Walle, C. G. V. D.; Bassett, L. C. Probing the Optical Dynamics of Quantum Emitters in Hexagonal Boron Nitride. *PRX Quantum* **2022**, *3*.

27. Couteau, C.; Barz, S.; Durt, T.; Gerrits, T.; Huwer, J.; Prevedel, R.; Rarity, J.; Shields, A.; Weihs, G. Applications of Single Photons to Quantum Communication and Computing. *Nature Reviews Physics* **2023**, *5*, 326–338.

28. Hübel, H.; Vanner, M. R.; Lederer, T.; Blauensteiner, B.; Lorünser, T.; Poppe, A.; Zeilinger, A. High-fidelity Transmission of Polarization Encoded Qubits from an

Entangled Source over 100 km of Fiber. *Opt. Express* **2007**, *15*, 7853–7862.

29. Sychev, D. V.; Ulanov, A. E.; Tiunov, E. S.; Pushkina, A. A.; Kuzhamuratov, A.; Novikov, V.; Lvovsky, A. I. Entanglement and Teleportation Between Polarization and Wave-Like Encodings of an Optical Qubit. *Nature Communications* **2018**, *9*, 3672.

30. Lo, H.-K.; Curty, M.; Tamaki, K. Secure Quantum Key Distribution. *Nat. Photon.* **2014**, *8*, 595–604.

31. Jungwirth, N. R.; Fuchs, G. D. Optical Absorption and Emission Mechanisms of Single Defects in Hexagonal Boron Nitride. *Physical Review Letters* **2017**, *119*, 057401.

32. Exarhos, A. L.; Hopper, D. A.; Grote, R. R.; Alkauskas, A.; Bassett, L. C. Optical Signatures of Quantum Emitters in Suspended Hexagonal Boron Nitride. *ACS Nano* **2017**, *11*, 3328–3336.

33. Kupko, T.; von Helversen, M.; Rickert, L.; Schulze, J. H.; Strittmatter, A.; Gschrey, M.; Rodt, S.; Reitzenstein, S.; Heindel, T. Tools for the Performance Optimization of Single-Photon Quantum Key Distribution. *npj Quantum Information* **2020**, *6*.

34. Wang, T.; Puchtler, T. J.; Zhu, T.; Jarman, J. C.; Nuttall, L. P.; Oliver, R. A.; Taylor, R. A. Polarisation-Controlled Single Photon Emission at High Temperatures from InGaN Quantum Dots. *Nanoscale* **2017**, *9*, 9421–9427.

35. Rugar, A. E.; Dory, C.; Sun, S.; Vučković, J. Characterization of Optical and Spin Properties of Single Tin-Vacancy Centers in Diamond Nanopillars. *Phys. Rev. B* **2019**, *99*, 205417.

36. Ates, S.; Ulrich, S. M.; Reitzenstein, S.; Löffler, A.; Forchel, A.; Michler, P. Post-Selected Indistinguishable Photons from the Resonance Fluorescence of a Single Quantum Dot in a Microcavity. *Phys. Rev. Lett.* **2009**, *103*, 167402.

37. White, S. J.; Duong, N. M. H.; Solntsev, A. S.; Kim, J. H.; Kianinia, M.; Aharonovich, I. Optical Repumping of Resonantly Excited Quantum Emitters in Hexagonal Boron Nitride. *Physical Review Applied* **2020**, *14*.

38. Grange, T.; Somaschi, N.; Antón, C.; De Santis, L.; Coppola, G.; Giesz, V.; Lemaître, A.; Sagnes, I.; Auffèves, A.; Senellart, P. Reducing Phonon-Induced Decoherence in Solid-State Single-Photon Sources with Cavity Quantum Electrodynamics. *Phys. Rev. Lett.* **2017**, *118*, 253602.

39. Sakib, M. A.; Triplett, B.; Harris, W.; Hussain, N.; Senichev, A.; Momenzadeh, M.; Bocanegra, J.; Vabishchevich, P.; Wu, R.; Boltasseva, A.; Shalaev, V. M.; Shcherbakov, M. R. Purcell-Induced Bright Single Photon Emitters in Hexagonal Boron Nitride. *Nano Letters* **2024**, *24*, 12390–12397, PMID: 39311406.

40. Arcari, M.; Sollner, I.; Javadi, A.; Hansen, S. L.; Mahmoodian, S.; Liu, J.; Thyrrestrup, H.; Lee, E. H.; Song, J. D.; Stobbe, S.; Lodahl, P. Near-Unity Coupling Efficiency of a Quantum Emitter to a Photonic Crystal Waveguide. *Physical Review Letters* **2014**, *113*, 1–5.

41. Sontheimer, B.; Braun, M.; Nikolay, N.; Sadzak, N.; Aharonovich, I.; Benson, O. Photodynamics of Quantum Emitters in Hexagonal Boron Nitride Revealed by Low-Temperature Spectroscopy. *Phys. Rev. B* **2017**, *96*, 121202.

42. Paralikis, A.; Piccinini, C.; Madigawa, A. A.; Metuh, P.; Vannucci, L.; Gregersen, N.; Munkhbat, B. Tailoring Polarization in WSe_2 Quantum Emitters through Deterministic Strain Engineering. *npj 2D Materials and Applications* **2024**, *8*, 59.

43. Jungwirth, N. R.; Chang, H.-S.; Jiang, M.; Fuchs, G. D. Polarization Spectroscopy of Defect-Based Single Photon Sources in ZnO. *ACS Nano* **2016**, *10*, 1210–1215.

44. Kumar, A.; Samaner, C.; Cholsuk, C.; Matthes, T.; Pacal, S.; Oyun, Y.; Zand, A.; Chapman, R. J.; Saerens, G.; Grange, R.; Suwanna, S.; Ates, S.; Vogl, T. Polarization Dynamics of Solid-State Quantum Emitters. *ACS Nano* **2024**, *18*, 5270–5281, PMID: 38335970.

45. Samaner, C.; Ates, S. Time-Resolved Stokes Analysis of Single Photon Emitters in Hexagonal Boron Nitride. 2025; `https://arxiv.org/abs/2504.11193`.

46. Zhong, D.; Gao, S.; Saccone, M.; Greer, J. R.; Bernardi, M.; Nadj-Perge, S.; Faraon, A. Carbon-Related Quantum Emitter in Hexagonal Boron Nitride with Homoge-

neous Energy and 3-Fold Polarization. *Nano Letters* **2024**, *24*, 1106–1113, PMID: 38240528.

47. Jara, C.; Rauch, T.; Botti, S.; Marques, M. A. L.; Norambuena, A.; Coto, R.; Castellanos-Aguila, J. E.; Maze, J. R.; Munoz, F. First-Principles Identification of Single Photon Emitters Based on Carbon Clusters in Hexagonal Boron Nitride. *The Journal of Physical Chemistry A* **2021**, *125*, 1325–1335, PMID: 33554602.

48. Linderalv, C.; Wieczorek, W.; Erhart, P. Vibrational Signatures for the Identification of Single-Photon Emitters in Hexagonal Boron Nitride. *Phys. Rev. B* **2021**, *103*, 115421.

49. Fox, M. *Quantum Optics: An Introduction*; Oxford University Press, 2006.

50. Loudon, R. *The Quantum Theory of Light*, 3rd ed.; Oxford University Press: Oxford, UK, 2000.

51. Saleh, B. E. A.; Teich, M. C. *Fundamentals of Photonics; 2nd ed.*; Wiley series in pure and applied optics; Wiley: New York, NY, 2007.

52. Kimble, H. J.; Dagenais, M.; Mandel, L. Photon Antibunching in Resonance Fluorescence. *Phys. Rev. Lett.* **1977**, *39*, 691–695.

53. Lounis, B.; Orrit, M. Single-Photon Sources. *Reports on Progress in Physics* **2005**, *68*, 1129.

54. Brown, R. H.; Twiss, R. Q. Correlation Between Photons in Two Coherent Beams of Light. *Nature* **1956**, *177*, 27–29.

55. Berhane, A. M.; Bradac, C.; Aharonovich, I. Photoinduced Blinking in a Solid-State Quantum System. *Phys. Rev. B* **2017**, *96*, 041203.

56. Novotny, L.; Hecht, B. *Principles of Nano-Optics*, 2nd ed.; Cambridge University Press, 2012.

57. Stoneham, A. M. *Theory of Defects in Solids: Electronic Structure of Defects in Insulators and Semiconductors*; Oxford University Press, 2007.

58. Chen, Y.-C.; Lin, S.-C.; Chou, J.-P.; Tsai, Y.-C.; Huang, C.-T.; Lee, C.-J.; Chang, W.-H. Stable Single Photon Emitters with Large Debye-Waller Factor in Silica. *ACS Photonics* **2025**, *12*, 1461–1469.

59. Aharonovich, I.; Tetienne, J. P.; Toth, M. Quantum Emitters in Hexagonal Boron Nitride. *Nano Letters* **2022**, *22*, 9227–9235.

60. Kubanek, A. Coherent Quantum Emitters in Hexagonal Boron Nitride. *Advanced Quantum Technologies* **2022**, *5*, 2200009.

61. Mai, T. N. A.; Hossain, M. S.; Nguyen, N. M.; Chen, Y.; Chen, C.; Xu, X.; Trinh, Q. T.; Dinh, T.; Tran, T. T. Quantum Emitters in Hexagonal Boron Nitride: Principles, Engineering and Applications. *Advanced Functional Materials* **2025**,

62. Sharman, K.; Golami, O.; Wein, S. C.; Zadeh-Haghighi, H.; Rocha, C. G.; Kubanek, A.; Simon, C. A DFT Study of Electron-Phonon Interactions for the C2CN and VNNB Defects in Hexagonal Boron Nitride: Investigating the Role of the Transition Dipole Direction. *Journal of Physics Condensed Matter* **2023**, *35*.

63. Kumar, A.; Cholsuk, C.; Mishuk, M. N.; Hazra, M.; Pillot, C.; Matthes, T.; Shaik, T. A.; Çakan, A.; Deckert, V.; Suwanna, S.; Vogl, T. Comparative Study of Quantum Emitter Fabrication in Wide Bandgap Materials Using Localized Electron Irradiation. *ACS Applied Optical Materials* **2024**, *2*, 323–332.

64. Kumar, A.; Cholsuk, C.; Zand, A.; Mishuk, M. N.; Matthes, T.; Eilenberger, F.; Suwanna, S.; Vogl, T. Localized Creation of Yellow Single Photon Emitting Carbon Complexes in Hexagonal Boron Nitride. *APL Materials* **2023**, *11*, 071108.

65. Esmann, M.; Wein, S. C.; Anton-Solanas, C. Solid-State Single-Photon Sources: Recent Advances for Novel Quantum Materials. 2024.

66. Grosso, G.; Moon, H.; Lienhard, B.; Ali, S.; Efetov, D. K.; Furchi, M. M.; Jarillo-Herrero, P.; Ford, M. J.; Aharonovich, I.; Englund, D. Tunable and High-Purity Room Temperature Single-Photon Emission from Atomic Defects in Hexagonal Boron Nitride. *Nature Communications* **2017**, *8*.

67. Shotan, Z.; Jayakumar, H.; Considine, C. R.; Mackoit, M.; Fedder, H.; Wrachtrup, J.;

Alkauskas, A.; Doherty, M. W.; Menon, V. M.; Meriles, C. A. Photoinduced Modification of Single-Photon Emitters in Hexagonal Boron Nitride. *ACS Photonics* **2016**, *3*, 2490–2496.

68. Sharma, K. K. *Optics: Principles and Applications*; Elsevier/Academic Press, 2015.

69. Chipman, R. A.; Lam, W. S. T.; Young, G. *Polarized light and Optical Systems*; CRC Press, Taylor, Francis Group, 2019.

70. Gisin, N.; Ribordy, G.; Tittel, W.; Zbinden, H. Quantum Cryptography. *Rev. Mod. Phys.* **2002**, *74*, 145–195.

71. Santori, C.; Fattal, D.; Yamamoto, Y. *Single-Photon Devices and Applications*; Wiley-VCH: Weinheim, 2010.

72. Lakowicz, J. R. *Principles of Fluorescence Spectroscopy*, 3rd ed.; Springer: Boston, MA, 2006.

73. Kurtsiefer, C.; Mayer, S.; Zarda, P.; Weinfurter, H. Stable Solid-State Source of Single Photons. *Phys. Rev. Lett.* **2000**, *85*, 290–293.

74. Brouri, R.; Beveratos, A.; Poizat, J.-P.; Grangier, P. Photon Antibunching in the Fluorescence of Individual Color Centers in Diamond. *Opt. Lett.* **2000**, *25*, 1294–1296.

75. Slussarenko, S.; Pryde, G. J. Photonic Quantum Information Processing: A Concise Review. *Applied Physics Reviews* **2019**, *6*, 041303.

76. Yu, S.; Zhang, X.; Lei, X.; Zhai, L. A Concise Primer on Solid-State Quantum Emitters. *IEEE Journal of Selected Topics in Quantum Electronics* **2025**, *31*, 1–16.

77. Schofield, R. C.; Clear, C.; Hoggarth, R. A.; Major, K. D.; McCutcheon, D. P. S.; Clark, A. S. Photon Indistinguishability Measurements Under Pulsed and Continuous Excitation. *Phys. Rev. Res.* **2022**, *4*, 013037.

78. Schaefer, B.; Collett, E.; Smyth, R.; Barrett, D.; Fraher, B. Measuring the Stokes polarization parameters. *American Journal of Physics* **2007**, *75*, 163–168.

79. Shannon, C. E. Communication in the Presence of Noise. *Proceedings of the IRE* **1949**, *37*, 10–21.

80. Cusco, R.; Gil, B.; Cassabois, G.; Artus, L. Temperature Dependence of Raman-Active Phonons and Anharmonic Interactions in Layered Hexagonal BN. *Physical Review B* **2016**, *94*, 1–11.

81. Bennett, C. H.; Brassard, G. Quantum Cryptography: Public Key Distribution and Coin Tossing. *Theoretical Computer Science* **2014**, *560*, 7–11.

82. Bennett, C. H.; Bessette, F.; Brassard, G.; Salvail, L.; Smolin, J. Experimental Quantum Cryptography. *Journal of Cryptology* **1992**, *5*, 3–28.

83. Shor, P. W. Polynomial-Time Algorithms for Prime Factorization and Discrete Logarithms on a Quantum Computer. *SIAM Journal on Computing* **1997**, *26*, 1484–1509.

84. Chen, L.; Jordan, S.; Liu, Y.-K.; Moody, D.; Peralta, R.; Perlner, R.; Smith-Tone, D. *Report on Post-Quantum Cryptography*; 2016; https://csrc.nist.gov/pubs/ir/8105/final (accessed Aug 12, 2025).

85. Moody, D. *Status Report on the Third Round of the NIST Post-Quantum Cryptography Standardization Process*; 2022; https://www.nist.gov/publications/status-report-third-round-nist-post-quantum-cryptography-standardization-process (accessed Aug 12, 2025).

86. Gottesman, D.; Lo, H.-K.; Lütkenhaus, N.; Preskill, J. Security of Quantum Key Distribution with Imperfect Devices. *Quantum Info. Comput.* **2004**, *4*, 325–360.

87. Shor, P. W.; Preskill, J. Simple Proof of Security of the BB84 Quantum Key Distribution Protocol. *Phys. Rev. Lett.* **2000**, *85*, 441–444.

88. Bassi, A.; Ghirardi, G. The Quantum Measurement Problem: State of Play. *Physics Reports* **2003**, *379*, 257–426.

89. Wootters, W. K.; Zurek, W. H. A Single Quantum Cannot be Cloned. *Nature* **1982**, *299*, 802–803.

90. National Security Agency, *The Commercial National Security Algorithm Suite 2.0 and Quantum Computing FAQ*; 2024; https://www.nsa.gov/Cybersecurity/Post-Quantum-Cybersecurity-Resources/ (accessed August 12, 2025).

91. Bundesamt für Sicherheit in der Informationstechnik (BSI), *Quantum-Safe Cryptography - Fundamentals, Current Developments and Recommendations*; 2022; https://www.bsi.bund.de/SharedDocs/Downloads/EN/BSI/Publications/Brochure/ (accessed August 12, 2025).

92. Lydersen, L.; Wiechers, C.; Wittmann, C.; Elser, D.; Skaar, J.; Makarov, V. Hacking Commercial Quantum Cryptography Systems by Tailored Bright Illumination. *Nature Photonics* **2010**, *4*, 686–689.

93. Bechmann-Pasquinucci, H. Eavesdropping Without Quantum Memory. *Phys. Rev. A* **2006**, *73*, 044305.

94. Pirandola, S. et al. Advances in Quantum Cryptography. *Adv. Opt. Photon.* **2020**, *12*, 1012–1236.

95. Shu, H. Asymptotically Optimal Prepare-Measure Quantum Key Distribution Protocol. *International Journal of Theoretical Physics* **2023**, *62*, 191.

96. Tamaki, K.; Koashi, M.; Imoto, N. Unconditionally Secure Key Distribution Based on Two Nonorthogonal States. *Phys. Rev. Lett.* **2003**, *90*, 167904.

97. Tamaki, K.; Lütkenhaus, N. Unconditional Security of the Bennett 1992 Quantum Key-Distribution Protocol over a Lossy and Noisy Channel. *Phys. Rev. A* **2004**, *69*, 032316.

98. Ekert, A. K. Quantum Cryptography Based on Bell's Theorem. *Phys. Rev. Lett.* **1991**, *67*, 661–663.

99. Bennett, C. H.; Brassard, G.; Mermin, N. D. Quantum Cryptography without Bell's Theorem. *Phys. Rev. Lett.* **1992**, *68*, 557–559.

100. Cakan, A.; Cholsuk, C.; Gale, A.; Kianinia, M.; Pacal, S.; Ates, S.; Aharonovich, I.; Toth, M.; Vogl, T. Quantum Optics Applications of Hexagonal Boron Nitride De-

fects. *Advanced Optical Materials* **2025**, *13*, 2402508.

101. Zeng, H. Z. J.; Ngyuen, M. A. P.; Ai, X.; Bennet, A.; Solntsev, A. S.; Laucht, A.; Al-Juboori, A.; Toth, M.; Mildren, R. P.; Malaney, R., et al. Integrated Room Temperature Single-Photon Source for Quantum Key Distribution. *Optics Letters* **2022**, *47*, 1673–1676.

102. Al-Juboori, A.; Zeng, H. Z. J.; Nguyen, M. A. P.; Ai, X.; Laucht, A.; Solntsev, A.; Toth, M.; Malaney, R.; Aharonovich, I. Quantum Key Distribution using a Quantum Emitter in Hexagonal Boron Nitride. *Advanced Quantum Technologies* **2023**, *6*, 2300038.

103. Waks, E.; Inoue, K.; Santori, C.; Fattal, D.; Vuckovic, J.; Solomon, G. S.; Yamamoto, Y. Quantum Cryptography with a Photon Turnstile. *Nature* **2002**, *420*, 762–762.

104. Rau, M.; Heindel, T.; Unsleber, S.; Braun, T.; Fischer, J.; Frick, S.; Nauerth, S.; Schneider, C.; Vest, G.; Reitzenstein, S., et al. Free Space Quantum Key Distribution over 500 meters using Electrically Driven Quantum Dot Single-Photon Sources-a Proof of Principle Experiment. *New Journal of Physics* **2014**, *16*, 043003.

105. Beveratos, A.; Brouri, R.; Gacoin, T.; Villing, A.; Poizat, J.-P.; Grangier, P. Single Photon Quantum Cryptography. *Physical review letters* **2002**, *89*, 187901.

106. Leifgen, M.; Schröder, T.; Gädeke, F.; Riemann, R.; Métillon, V.; Neu, E.; Hepp, C.; Arend, C.; Becher, C.; Lauritsen, K., et al. Evaluation of Nitrogen-and Silicon-Vacancy Defect Centres as Single Photon Sources in Quantum Key Distribution. *New journal of physics* **2014**, *16*, 023021.

107. Gao, T.; von Helversen, M.; Antón-Solanas, C.; Schneider, C.; Heindel, T. Atomically-Thin Single-Photon Sources for Quantum Communication. *npj 2D Materials and Applications* **2023**, *7*, 4.

108. Murtaza, G.; Colautti, M.; Hilke, M.; Lombardi, P.; Cataliotti, F. S.; Zavatta, A.; Bacco, D.; Toninelli, C. Efficient Room-Temperature Molecular Single-Photon

Sources for Quantum Key Distribution. *Optics Express* **2023**, *31*, 9437–9447.

109. Waks, E.; Santori, C.; Yamamoto, Y. Security Aspects of Quantum Key Distribution with Sub-Poisson Light. *Phys. Rev. A* **2002**, *66*, 042315.

110. Bunandar, D.; Govia, L. C. G.; Krovi, H.; Englund, D. Numerical Finite-Key Analysis of Quantum Key Distribution. *npj Quantum Information* **2020**, *6*, 104.

VITA

Çağlar Samaner received his Bachelor of Science degree in Physics from Ege University in 2016 with a GPA of 3.63 out of 4.00. He earned his Master of Science degree in Physics from the Izmir Institute of Technology in 2019. In 2025, he completed his Ph.D. in Physics at the same institution. His doctoral research focused on the polarization dynamics of single-photon emitters in hexagonal boron nitride and their application in quantum key distribution.

During his graduate studies, he worked as a research assistant in the Department of Physics at the Izmir Institute of Technology. He designed and built advanced confocal microscopy setups, performed polarization-resolved photoluminescence and time-correlated single-photon counting experiments, and developed automated control and data analysis tools using LabVIEW, MATLAB, and Python. He played a leading role in achieving Turkey's first complete demonstration of a free-space quantum key distribution protocol using solid-state single-photon emitters.

His scholarly contributions include the following works: "Free-Space Quantum Key Distribution with Single Photons from Defects in Hexagonal Boron Nitride," published in *Advanced Quantum Technologies* (2022, featured on the journal's front cover); "Polarization Dynamics of Solid-State Quantum Emitters," published in *ACS Nano* (2024); and "Time-Resolved Stokes Polarization Analysis of Single Photon Emitters in Hexagonal Boron Nitride," currently under peer review for publication in *ACS Photonics* (2025).

He has presented his research at various national and international conferences, including EQEP in Stuttgart (2024), STMSE in Ankara (2023), and Quantum Days (2025), and was honored with Best Poster Awards at the 764. WE-Heraeus Seminar (Germany, 2022) and Photonics 2022 (Ankara). He was also invited to speak at a local workshop in 2025 on quantum technologies.